ASSESSING SOIL EROSION OF AGRICULTURE FIELD DURING WINTER AND SUMMER SEASONS USING 3D SCANNING AND CLOSE-RANGE PHOTOGRAMMETRY TECHNOLOGY

by

Fangzhou Zheng

B.Sc. (Hons), Dalhousie University Faculty of Agriculture, 2012

A Thesis Submitted in Partial Fulfillment
of the Requirements for the Degree of

Master of Science in Forestry

in the Graduate Academic Unit of **Forestry and Environmental Management**

Supervisors: Fan-Rui Meng, Ph.D., Forestry & Env. Management
Sheng Li, Ph.D., Forestry & Env. Management

Examining Board: Paul A Arp, Ph.D. Forestry & Env. Management, Chair
Yefang Jiang, Ph.D. Civil Engineering

This thesis is accepted by the
Dean of Graduate Studies

THE UNIVERSITY OF NEW BRUNSWICK

August 2016

© Fangzhou Zheng, 2016

ABSTRACT

Soil surface morphology is strongly affected by land management practices and soil biophysical processes such as soil erosion. Traditional methods on measuring soil surface morphology changes have been costly, time-consuming and causing extra soil disturbance. Alternatively, remote sensing technologies involving 3D scanning and photogrammetry are becoming available and capable of measuring surface morphology correctly and quickly. With these techniques, studies have focused on small-scale rill erosion during short snow-free periods.

In this study, the performances and accuracies of 3D scanner and photogrammetry methods on detecting morphological features, i.e., total station scanner (TSS) and close-range photogrammetry (CRP), were evaluated and optimized. Three parameters (width, depth and area) of each morphological feature of two surfaces, a ridged and channeled plywood board (2.4 m by 3.6 m) and a ridged and channeled bare-earth plot (6 m by 20 m), were derived using both remote sensing methods and actual measurement. For the plywood board assessment, the optimal TSS and CRP root mean square errors achieved were: width = 1.3 cm vs. 0.8 cm; depth = 1.0 cm vs. 0.4 cm; areas = 7.8 cm^2 vs. 4.2 cm^2. Whereas for the bare-earth plot, the optimal TSS and CRP root mean square errors were: width = 3.4 cm vs. 1.1 cm; depth = 2.2 cm vs. 1.6 cm. Hence, the performances of CRP on detecting morphological changes are better than the TSS results. However, the TSS method

is more practical than CRP by allowing larger scanning distance and fewer operators.

A field experiment was conducted at the Agriculture and Agri-Food Canada Fredericton Research and Development Centre, New Brunswick, on 6 m by 80 m large plots to determine surface morphological changes under three tillage treatments during two winter and summer seasons. The treatments involved (i) potato cropping with up-down-slope tillage, (ii) potato cropping with contour tillage, and (iii) fallowing with up-down-slope tillage (control). The periods lasted (i) from snowfall to after snowmelt, and (ii) from seeding to about one-third potato canopy coverage. Surface morphologies (elevation, slope, curvature) were scanned and evaluated at the beginning and end of each period. Also, soil moisture at 15 and 30 cm depth, and soil temperature at 15 cm depth were monitored within the winter period before and after freezing.

For the winter period, there was an about 2.1 cm to 2.9 cm drop in elevation for the plots as a whole. Translating these changes in soil losses, assuming that these changes were due to soil erosion, and that the soil bulk density equals to 1.1 g cm^{-3}, they can procure a net soil loss of 231 Mg ha^{-1} to 319 Mg ha^{-1}. However, this elevation changes is unlikely being caused by soil erosion alone, but attribute to soil-structure and compactions caused by freeze-thaw action, snowpack compaction that could change soil aggregation and pore volumes.

For the summer period, the plots revealed an elevation drop in the distance ranges of approximately 0 m – 20 m and 40 m – 50 m from the top of the plots. On the other hand, elevation rise was observed at approximately 20 – 40 m and 50 – 70 m. This drop and rise would translate into overall soil loss of 55 to 110 Mg ha^{-1} for the cropped plots, and a net soil gain of 22 to 88 Mg ha^{-1} for the fallow plots.

In some of the winter and summer plots, water-induced erosion rill was detected using both TSS and CRP methods. For the same rill derived from the summer period, CRP yields higher and more accurate value than TSS by about 0.9 Mg ha^{-1}.

Overall, these results indicate that both technologies are able to capture surface elevation changes and detect erosion rills. However, neither method could be used to determine sheet erosion correctly. Hence, further methodology refinements are needed to ensure that the TSS and CRP results are not affected by the freeze-thaw action or the presence of ground-covering vegetation due to, e.g. cropping or fallowing.

ACKNOWLEDGEMENT

Firstly, I would like to acknowledge Agriculture and Agri-food Canada (AAFC) and Natural Sciences and Engineering Research Council of Canada (NSERC) for funding.

More importantly, I would like to thank my Advisory Committee members, Dr. Rene Wackrow from the Loughborough University, Dr. David Lobb from the University of Manitoba, Dr. Yun Zhang and, my supervisors, Dr. Fan-rui Meng and Dr. Sheng Li for their endless support and thoughtful advice for my studies at the University of New Brunswick.

Also, I would like to thank Monica Boudreault, Meagan Betts, Tegan Smith, Jimmy Qi, Eric Liu, John Monteith, Lionel Stevens, and in particular, Dr. Zisheng Xing for their help with the field work and/or lab analyses.

At last, I would like to thank my wife, Anran Chen and my parents in China for their encouragement and support during my studies in Canada.

Table of Contents

ABSTRACT ii
ACKNOWLEDGEMENT v
Table of Contents vi
List of Tables ix
List of Figures xi
List of Acronyms xiv
Chapter 1 Introduction 1
1.1 Background 2
1.2 Outline of thesis 7
Reference 10
Chapter 2 Assessing the accuracy of toal station scanning and close-range photogrammetry for quantifying soil surface morphology 14
Abstract 15
2.1 Introduction 16
2.2 Materials and Methods 20
2.2.1 Equipment 20
2.2.1.1 Total station scanning (TSS) 20
2.2.1.2 Close-range photogrammetry (CRP) 21
2.2.2 Indoor board test 24
2.2.3 Outdoor field test 26
2.2.4 Data extraction and analysis 29
2.3 Results and Discussion 33
2.3.1 Indoor board test 33
2.3.1.1 Visual observations 33
2.3.1.2 Width of the AMFs 36
2.3.1.3 Depth of the AMFs 40
2.3.1.4 Area of the AMFs 43
2.3.1.5 Zonal analysis 45
2.3.1.6 Applicability analysis 48
2.3.2 Outdoor field test 49

2.3.2.1 Visual observations 49
2.3.2.2 Width of AMFs 51
2.3.2.3 Depth of AMFs 55
2.3.2.4 Zonal analysis 57
2.3.2.5 Applicability analysis 60
2.4 Conclusion 61
Reference 63
Chapter 3 Quantifying soil surface evolution during winter and snow melting using total station scanning and close-range photogrammetry 68
Abstract 69
3.1 Introduction 71
3.2 Methodology 74
3.2.1 Site setup 74
3.2.2 Equipment 77
3.2.2.1 Total station scanning (TSS) 77
3.2.2.2 Close-range photogrammetry (CRP) 78
3.2.3 Field experiment 78
3.2.4 Data extraction and analysis 80
3.2.4.1 DEM generation 80
3.2.4.2 Channel detection 80
3.2.4.3 Elevation change 81
3.2.4.4 Field verification and validation 83
3.3 Results and discussion 86
3.3.1 Channel detection 86
3.3.2 Elevation change 90
3.3.3 Field verification and validation 102
3.4 Conclusion 108
Reference 109
Chapter 4 Quantifying soil surface evolution during summer using total station scanning and close-range photogrammetry 112
Abstract 113
4.1 Introduction 114

4.2 Methodology 117
4.2.1 Site setup 117
4.2.2 Equipment 118
4.2.3 Field experiment 119
4.2.4 Data extraction and analyses 120
4.2.4.1 DEM generation 120
4.2.4.2 Channel detection 121
4.2.4.3 Elevation change 122
4.2.4.4 Method verification 123
4.3 Results and discussion 124
4.3.1 Channel detection 124
4.3.2 Elevation change 127
4.3.2.1 The TSS method 127
4.3.2.2 The CRP method 130
4.3.3 Method verification 142
4.4 Conclusion 145
Reference 147
Chapter 5 Conclusion 150
5.1 General conclusions 151
5.2 Suggested future work 153
APPENDIX I 154
APPENDIX II 156
CURRICULUM VITAE

List of Tables

Table 2.1. Measured value (width, depth and area) of each artificial morphological feature (AMF) for the indoor test. 25
Table 2.2. Measured value (width and depth) of each artificial morphological feature (AMF) for the outdoor test. 28
Table 2.3. Camera distance (m) and photos taking interval (m) for different overlap rates (%). 29
Table 2.4. Average width (cm), SD (cm) and RMSE (cm) of each morphological feature derived from manual measurement & different remote sensing methods for the indoor test. 37
Table 2.5. Average depth (cm), SD (cm) and RMSE (cm) of each morphological feature derived from manual measurement & different remote sensing methods for the indoor test. 40
Table 2.6. Average area (cm^2), SD (cm^2) and RMSE (cm^2) of each morphological feature derived from manual measurement & different remote sensing methods for the indoor test. 43
Table 2.7. Measured elevation differences (cm) and elevation differences (cm) derived from DEM using different methods by zone for the indoor test. 45
Table 2.8. Consumptions (operator, time) and detecting range (m) of different methods for the indoor test. 48
Table 2.9. Average width (cm), SD (cm) and RMSE (cm) of each morphological feature derived from manual measurement & different remote sensing methods for the outdoor test. 52
Table 2.10. Average depth (cm), SD (cm) and RMSE (cm) of each morphological feature derived from manual measurement and different remote sensing methods for the outdoor test. 55
Table 2.11. Consumptions (operator, time) and detecting range (m) of different methods for the outdoor test. 60
Table 3.1. Tillage treatments and symbols for six plots. 76
Table 3.2. Dimensions and channelized erosion rate (Mg ha^{-1}) of a channel derived from the DEMs using both methods during 2013 winter period. 88
Table 3.3. Dimensions and channelized erosion rate (Mg ha^{-1}) of a channel derived from the DEMs using both methods during 2014 winter period. 90

Table 3.4. Mass-based (Mg ha^{-1}) and depth-based (cm) elevation drop with different tillage treatments using remote sensing methods during the winter period. 101
Table 3.5. Correlation Coefficient (r) between elevation change and slope gradient and between elevation change and slope curvature for 6 plots during the winter period. 101
Table 3.6. Measured seasonal erosion rate (Mg ha^{-1}) over the entire plot and elevation drop (Mg ha^{-1}) derived from the remote sensing methods under different tillage treatments during the winter period. 104
Table 3.7. Soil moisture content (m^3 m^{-3}) during freezing period and elevation drop (cm) during winter at three locations (20 m, 40 m and 60 m) in Plot 4. 108
Table 4.1. Dimensions and channelized erosion rate (Mg ha^{-1}) of a channel derived from the DEMs using both methods during the summer period.127
Table 4.2. Mass-based (Mg ha^{-1}) and depth-based (cm) elevation drop with different tillage treatments using remote sensing methods during the summer period..... 141
Table 4.3. Correlation Coefficient (r) between elevation change and slope gradient and between elevation change and slope curvature for 6 plots during the summer period. 142

List of Figures

Figure 1.1. Schematic of research conducted as part of this thesis, with individual chapters and their subject. 9
Figure 2.1. Test field for calibration of the photogrammetry methodology. 22
Figure 2.2. Aluminum platform (6 m wide and maximum 6 m high) for CRP method. 23
Figure 2.3. Manmade plywood surface for assessing remote sensing methods. 24
Figure 2.4. Bare-earth plot for assessing remote sensing methods. 27
Figure 2.5. Nine zone labels of manmade plywood surface. 31
Figure 2.6. Illustration of detection range for the handheld CRP methods. 33
Figure 2.7. A transect extracted from each DEM generated using different remote sensing methods for the indoor test. 34
Figure 2.8. A transect extracted from each DEM generated using different remote sensing methods for the outdoor test. 50
Figure 2.9. Spatial distribution of elevation differences (m) using TSS methods for the outdoor test. 58
Figure 2.10. Spatial distribution of elevation differences using CRP methods for the outdoor test. 59
Figure 3.1. The experiment field and the layout of plots and geo-reference points used in this study. 75
Figure 3.2. Geo-reference point (left) and target (right) 76
Figure 3.3. Setup of total station (three positions) for TSS method. 79
Figure 3.4. Manual water sample collection from a flume during snowmelt season. 84
Figure 3.5. A large channel in the Plot 5 (T0) in May 2013. 86
Figure 3.6. DEMs with a channel of Plot 5 (T0) generated using TSS (left) and CRP (right) methods in May 2013. 87
Figure 3.7. A channel in the Plot 5 (T0) in May 2014. 89
Figure 3.8. DEMs with two channels of Plot 5 (T0) generated using TSS (left) and CRP (right) methods in May 2014. 89
Figure 3.9. Elevation changes (m) of Plot 1 (T1) generated using CRP method for the period from Nov 2013 to May 2014. 91
Figure 3.10. Lengthwise slope curvature (% m^{-1}) and slope gradient (%) of Plot 1 (T1) in May 2014. 91
Figure 3.11. Elevation changes (m) of Plot 2 (T1) generated using CRP method for the period from Nov 2013 to May 2014. 92

Figure 3.12. Lengthwise slope curvature (% m^{-1}) and slope gradient (%) of Plot 2 (T1) in May 2014. 93
Figure 3.13. Elevation changes (m) of Plot 3 (T2) generated using CRP method for the period from Nov 2013 to May 2014. 94
Figure 3.14. Lengthwise slope curvature (% m^{-1}) and slope gradient (%) of Plot 3 (T2) in May 2014. 94
Figure 3.15. Elevation changes (m) of Plot 4 (T2) generated using CRP method for the period from Nov 2013 to May 2014. 96
Figure 3.16. Lengthwise slope curvature (% m^{-1}) and slope gradient (%) of Plot 4 (T2) in May 2014. 96
Figure 3.17. Elevation changes (m) of Plot 5 (T0) generated using CRP method for the period from Nov 2013 to May 2014. 97
Figure 3.18. Lengthwise slope curvature (% m^{-1}) and slope gradient (%) of Plot 5 (T0) in May 2014. 98
Figure 3.19. Elevation changes (m) of Plot 6 (T0) generated using CRP method for the period from Nov 2013 to May 2014. 99
Figure 3.20. Lengthwise slope curvature (% m^{-1}) and slope gradient (%) of Plot 6 (T0) in May 2014. 99
Figure 3.21. Soil moisture (m^3 m^{-3}) during the spring period (from 2014.03.22 to 2014.05.30) in AAFC Fredericton Research and Development Centre. 102
Figure 3.22. Soil temperature (°c) during the winter period (from 2013.11.06 to 2013.12.31) at three locations (20 m, 40 m and 60 m) in Plot 4..... 105
Figure 3.23. Soil moisture (m^3 m^{-3}) during the winter period (from 2013.11.15 to 2013.12.31) at three locations (20 m, 40 m and 60 m) in Plot 4..... 106
Figure 3.24. Soil moisture (m^3 m^{-3}) during the snowmelt season (from 2014.04.09 to 2014.05.06) at three locations (20 m, 40 m and 60 m) in Plot 4..... 107
Figure 4.1. An original photo (left) and a processed photo (right) of soil surface. 120
Figure 4.2. A channel of Plot 5 (T0) generated after the hurricane event. 125
Figure 4.3. DEMs with a channel of Plot 5 (T0) generated using TSS (left) and CRP (right) methods on July 8th, 2014. 126
Figure 4.4. Elevation changes (m) of Plot 2 (T1) generated using TSS method for the period from June 20th, 2014 to July 8th, 2014. 128
Figure 4.5. Elevation changes (m) of Plot 4 (T2) generated using TSS method for the period from June 20th, 2014 to July 8th, 2014. 129
Figure 4.6. Elevation changes (m) of Plot 5 (T0) generated using TSS method for the period from June 20th, 2014 to July 8th, 2014. 130

Figure 4.7. Elevation changes (m) of Plot 1 (T1) generated using CRP method for the period from June 20th, 2014 to July 8th, 2014. 131
Figure 4.8. Lengthwise slope curvature (% m^{-1}) and slope gradient (%) of Plot 1 (T1) in July 2014. 131
Figure 4.9. Elevation changes (m) of Plot 2 (T1) generated using CRP method for the period from June 20th, 2014 to July 8th, 2014. 132
Figure 4.10. Lengthwise slope curvature (% m^{-1}) and slope gradient (%) of Plot 2 (T1) in July 2014. 133
Figure 4.11. Elevation changes (m) of Plot 3 (T2) generated using CRP method for the period from June 20th, 2014 to July 8th, 2014. 134
Figure 4.12. Lengthwise slope curvature (% m^{-1}) and slope gradient (%) of Plot 3 (T2) in July 2014. 134
Figure 4.13. Elevation changes (m) of Plot 4 (T2) generated using CRP method for the period from June 20th, 2014 to July 8th, 2014. 135
Figure 4.14. Lengthwise slope curvature (% m^{-1}) and slope gradient (%) of Plot 4 (T2) in July 2014. 136
Figure 4.15. Elevation changes (m) of Plot 5 (T0) generated using CRP method for the period from June 20th, 2014 to July 8th, 2014. 137
Figure 4.16. Lengthwise slope curvature (% m^{-1}) and slope gradient (%) of Plot 5 (T0) in July 2014. 137
Figure 4.17. Elevation changes (m) of Plot 6 (T0) generated using CRP method for the period from June 20th, 2014 to July 8th, 2014. 139
Figure 4.18. Lengthwise slope curvature (% m^{-1}) and slope gradient (%) of Plot 6 (T0) in July 2014. 139
Figure 4.19. Part of Plot 2 (T1) before the hurricane (left) and part of Plot 2 after the hurricane (right). 143
Figure 4.20. Elevation changes (m) of Plot 2 (T1) generated using CRP method before and after the hurricane event. 143
Figure 4.21. Part of Plot 3 (T2) before the hurricane (left) and part of Plot 3 after the hurricane (right). 144
Figure 4.22. Elevation changes (m) of Plot 3 (T2) generated using CRP method before and after the hurricane event. 144

List of Acronyms

TSS	Total station scanner
CRP	Close-range photogrammetry
TSS-M	Total station scanner at middle location
TSS-L	Total station scanner at left location
TSS-R	Total station scanner at right location
CRP-F	Frame-based close-range photogrammetry
CRP-H	Handheld close-range photogrammetry
CRP-H1	Handheld close-range photogrammetry on the ground
CRP-H2	Handheld close-range photogrammetry on the stand
CRP-H1-90	Handheld close-range photogrammetry on the ground with 90° shooting angle
CRP-H2-90	Handheld close-range photogrammetry on the stand with 90° shooting angle
CRP-H1-70	Handheld close-range photogrammetry on the ground with 70° shooting angle
CRP-H2-70	Handheld close-range photogrammetry on the stand with 70° shooting angle
CRP-H1-45	Handheld close-range photogrammetry on the ground with 45° shooting angle
CRP-H2-45	Handheld close-range photogrammetry on the stand with 45° shooting angle
CRP-H1-20	Handheld close-range photogrammetry on the ground with 20° shooting angle
CRP-H2-20	Handheld close-range photogrammetry on the stand with 20° shooting angle
CRP-53%LO&57%HO	Frame-based close-range photogrammetry with 53% longitudinal overlap and 57% horizontal overlap
CRP-53%LO&49%HO	Frame-based close-range photogrammetry with 53% longitudinal overlap and 49% horizontal overlap
CRP-53%LO&39%HO	Frame-based close-range photogrammetry with 53% longitudinal overlap and 39% horizontal overlap
CRP-53%LO&29%HO	Frame-based close-range photogrammetry with 53% longitudinal overlap and 29% horizontal overlap
CRP-53%LO&18%HO	Frame-based close-range photogrammetry with 53% longitudinal overlap and 18% horizontal overlap

CRP-88%LO&57%HO	Frame-based close-range photogrammetry with 88% longitudinal overlap and 57% horizontal overlap
CRP-77%LO&57%HO	Frame-based close-range photogrammetry with 77% longitudinal overlap and 57% horizontal overlap
CRP-30%LO&57%HO	Frame-based close-range photogrammetry with 30% longitudinal overlap and 57% horizontal overlap
CRP-7%LO&57%HO	Frame-based close-range photogrammetry with 7% longitudinal overlap and 57% horizontal overlap
AMF	Artificial morphological feature
VSC	V-shape channel
WSR	Wide square ridge
WSC	Wide square channel
MSR	Medium square ridge
HSR	High square ridge
NSC	Narrow square channel
NC	Narrow channel
WC	Wide channel
CBH1	Channel 1 between potato hills
CBH2	Channel 2 between potato hills
SIFT	Scale-invariant feature transform
DEM	Digital elevation model
SD	Standard deviation
RMSE	Root mean square error
T0	Fallow up-down-slope tillage
T1	Potato contour tillage
T2	Potato up-down-slope tillage

Chapter 1

Introduction

1.1 Background

Surface soil morphology plays an essential role in agriculture, such as in runoff generation and nutrient redistribution. Soil surface morphology can also be easily changed by tillage operations. On cultivated land such as potato fields, tillage operation can easily erase lower order channels and creates new small channels (furrows) and ridges. Soil surface morphology is also affected by processes such as freeze-thaw action, dry-wet action, biological activities, gravitational subsidence and soil erosion. For example, water in soil starts to freeze when soil temperature drops below freezing point (Ferrick and Gatto, 2004). During the freezing process, the increase in volume of ice leads to frost heaving. Expanding ice also pushes soil particles apart from each other, changing the structure of soil. Similar to the freeze-thaw action, the dry-wet action also impacts soil surface morphology. For instance, expansion and contraction of clay soil caused by dry-wet action can generate cracks in soil, resulting in changes of soil surface morphology. Animal movements disturb the soil and may also cause soil morphological changes.

Among all biophysical processes, soil erosion probably has the strongest impact on soil surface morphology. Soil erosion is the wearing away of the surface soil by wind, water, or other erosive forces. Its process generally can be divided into three steps: (i) detachment of soil particles, (ii) transportation of soil particles, and (iii) deposition of transported soil particles at another location. For water erosion in a rainfall event, soil particles are initially detached by to rain splashing. Runoff is initiated when the

infiltration rate of the soil is exceeded by the rainfall intensity. Water flows firstly as a thin layer, which does not have much power to separate soil particles. This is a process called sheet (inter-rill) erosion, and is characterized by soil movement at micro-scale. Further downslope, the quantity of runoff water accumulates, and its velocity accelerates. As a result, small rills are formed, causing rill erosion (Li, 2012). As topography converges, runoff is concentrated and often causes channelized erosion in ephemeral gullies. When the gully is are too wide or too deep to be eliminated by ordinary tillage operation, it is termed classical gully (Poesen et al., 2003). In cold-climate areas, such as Canada, snowmelt erosion contributes greatly to total soil erosion. Snowmelt erosion is different from rainfall erosion in processes mainly in two points. First, there is no rain splash during snowmelt period so that the detachment mechanism in snowmelt erosion is mainly through runoff (Li, 2012). Second, snow is often accumulated during the winter months so that the runoff in snowmelt event is often much greater than runoff in normal rain events. Therefore, the snowmelt erosion may lead to a greater soil loss compared to rainfall erosion, especially in Canada, where there is a large amount of snow in winter months.

Due to the strong impact of soil erosion on surface morphology, many studies measured surface morphological change as a means to assess soil erosion. The rill survey is an established way to assess rill creation and development by measuring dimensions and density of rills in a field manually. Several researchers have conducted detailed manual rill surveys in plots with bare soil surface (Bewket and

Sterk, 2003; Rejman and Brodowski, 2005). However, rill survey only focuses on measuring rill erosion, and requires considerable effort to collect the details of each rill. Another widely used method is erosion pin. It has been used to monitor stream bank erosion (Couper et al., 2002; Lawler, 1993; Stott, 1997) and inter-rill erosion (Ghimire et al., 2013). Directly quantifying soil surface evolution using these traditional methods can be challenging. First, the traditional methods usually are labor-intensive and time-consuming; second, the accuracy and resolution of these methods are often not enough for capturing morphological changes due to soil erosion; third, the natural environment may be disturbed while collecting data using these intrusive methods.

Recently, increasing numbers of soil surface morphology studies have utilized remote sensing technologies. Compared with traditional methods of measuring soil surface morphology, remote sensing methods can collect surface morphology quicker, more accurately, and with fewer disturbances. Remote sensing technologies can be categorized into active and passive remote sensing. In active remote sensing, an active sensor emits a signal and collects the reflected signal from the targets and surrounding areas. A passive sensor collects existing signal, such as sunlight, that is reflected from targets or surrounding areas. An example of the active remote sensing technology is the 3D scanning function of the new generation total stations. These total stations are equipped with a laser gun to shoot out a laser beam and collect the reflections. The round-trip travel time of a pulse is used to calculate the distance

between the scanner and the target. An example of passive remote sensing method is photogrammetry, which acquires information about objects and the surrounding environments by recording, measuring and interpreting photos (Matthews, 2008). Pairs of photos taken in photogrammetry mimic the three-dimensional view of the left and right eyes. Through mathematical interpolation, a detailed three-dimensional model can be generated from the two-dimensional photos of a stereo pair.

Several studies have employed airborne versions of these remote sensing methods to measure soil surface morphology (e.g., Croke et al., 2013; Perroy et al., 2010; Ventura et al., 2011). However, due to the distance of the sensor to the objects, the resolution and accuracy are low. With technical improvements, ground-based or close-range version of 3D scanning, as well as the photogrammetry method may provide solutions to overcome these limitations. Schmid et al. (2004) used the ground-based 3D scanner to monitor erosion rate in German forest site (about 20 m^2). Nasermoaddeli and Pasche (2008) also used the scanner to quantify the erosion rate of riverbanks in Germany as well. Ehiorobo and Izinyon (2013) used a 3D scanner and GPS equipment to survey erosion sites in Nigeria, for modeling soil loss from gullies. In addition, soil loss from the rill was quantified by Vinci et al. (2015) using a 3D scanner in Italy. Welch et al. (1984, 1983) used close-range photogrammetric techniques to predict gully and channel erosion, as well as analytical photogrammetry to monitor stream channel erosion in the USA. In a lab environment, Berger et al. (2010) monitored a rill network using close-range photogrammetry. Li

et al. (2014) simulated a snow melt environment condition on a frame (approximately 0.9 × 1.1 m) and used close-range photogrammetry to measure rill erosion in Alaska. These studies have focused on rill erosion in a small scale plot or on soil loss from river banks or gullies. They showed the potential and advantage of the ground-based remote sensing technology over the traditional methods. However, no study has been carried out to use ground-based remote sensing technology at the field-scale in agricultural lands. The challenge lies in that there are often multiple processes happening simultaneously, all affecting soil surface morphology.

In order to use the ground-based remote sensing technologies to measure surface morphology in agricultural fields, it is essential to assess their errors associated with these methods. Studies on the accuracy of ground-based remote sensing methods have been carried out by a number of researchers. Miri and Varshosaz (2011) found that increasing the distance between a target and sensor or increasing the shooting angle both can lead to a decrease in the accuracy of a ground-based 3D scanner. Ali et al. (2000) conducted an experiment under a specific setting in order to test factors that may influence the accuracy of close-range photogrammetry. He found that increasing the distance between the object and the camera led to lower vertical accuracy. However, further testing showed that increasing the number of camera stations resulted in more accurate products. Butler et al. (1998) assessed the accuracy of surface roughness extracted from close-range photogrammetry, while Samad et al. (2010) assessed the accuracy of stream mapping using similar technology. These

studies were carried out mostly with specific setting or for a specific area. There is a lack of systematic assessment of these technologies on the magnitude of their errors and the affecting factors.

Overall, it is clear that ground-based remote sensing approaches have the potential and advantage over the traditional method of monitoring soil surface evolution. In this thesis, I selected two ground-based remote sensing technologies, the total station scanner and close-range photogrammetry, examined their performance and used them in field plots under tillage treatments for two years.

The objectives are:

(i) To assess the accuracy of the total station scanner and close-range photogrammetry for quantifying soil surface morphological change.

(ii) To quantify the soil surface morphological change during two periods (winter and summer) using the two remote sensing methods.

1.2 Outline of thesis

The general framework of this research is illustrated in Figure 1.1. Chapter 2 presents the accuracy assessment of total station scanner (TSS) and the close-range photogrammetry (CRP). The assessment was conducted indoor using a board surface with artificial ridges and channels, as well as outdoor on an area in the field with man-made ridges and channels. Three geometry parameters: width, depth, and cross-sectional areas are used. These parameters were extracted from the remote

sensing data and also measured manually. By comparing the parameters derived from manual measurement with that of the remote sensing methods, the errors of remote sensing methods can be assessed. In Chapter 3, both TSS and CRP were employed to quantify soil surface evolution during the winter period to quantify the impact of snowmelt runoff and other processes on soil surface changes. The experiment was carried out in six agricultural plots with different tillage practices. The surface morphology of these plots was determined before snowfall and after snowmelt using both remote sensing methods. The difference in soil surface at the different time reflects the soil surface evolution during the winter season. Sediment data collected from the field plots were used to validate the remote sensing results. In Chapter 4, a similar approach was used to quantify soil surface evolution during the summer period in order examine the influence of rainfall erosion and other processes on soil surface evolution during the summer period.

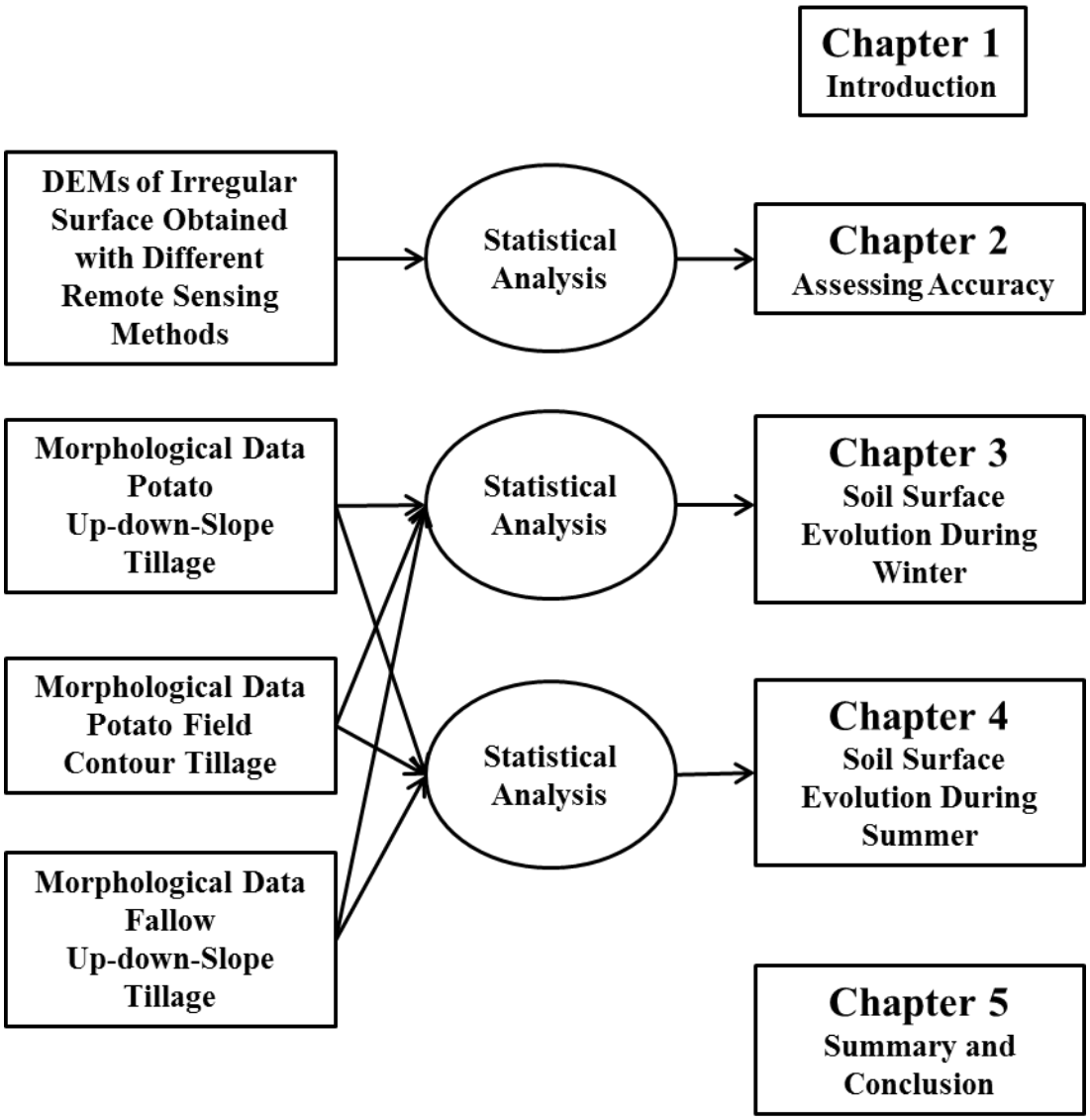

Figure 1.1. Schematic of research conducted as part of this thesis, with individual chapters and their subject.

Reference

Ali, M. E. N. O., Eliwa, M. A., Mohanmed, A. A. E., Abbas, E. A. M., 2000. Accuracy analysis for new close-range photogrammetric systems. International Archives of Photogrammetry and Remote Sensing. 33: Part B5.

Berger, C., Schulze, M., Rieke-Zapp, D., Schlunegger, F., 2010. Rill development and soil erosion: a laboratory study of slope and rainfall intensity. Earth Surface Processes and Landforms. 35(12): 1456-1467.

Bewket, W., Sterk, G., 2003. Assessment of soil erosion in cultivated fields using a survey methodology for rills in the Chemoga watershed, Ethiopia.Agriculture, ecosystems & environment. 97(1): 81-93.

Butler, J.B., Lane, S.N., Chandler, J.H., 1998. Assessment of DEM quality for characterizing surface roughness using close range digital photogrammetry. The Photogrammetric Record. 16(92): 271-291.

Couper, P., Stott, T. A., Maddock, A., 2002. Insights into river bank erosion processes derived from analysis of negative erosion-pin recordings: Observations from three recent UK studies. Earth Surf. Process. Landf. 27: 59–79.

Croke, J., Todd, P., Thompson, C., Watson, F., Denham, R., Khanal, G., 2013. The use of multi temporal LiDAR to assess basin-scale erosion and deposition following the catastrophic January 2011 Lockyer flood, SE Queensland, Australia. Geomorphology. 184: 111-126.

Ehiorobo, J. O., Izinyon, O.C., 2013. Monitoring of soil loss from erosion using geoinformatics and geotechnical engineering methods. Journal of civil engineering and architecture. 7(1): 78-84.

Ferrick, M. G., Gatto, L. W., 2004. Quantifying the effect of a freeze-thaw cycle on soil erosion: laboratory experiments. Earth surface processes and landforms. 30(10): 1305-1326.

Ghimire, S.K., Higaki, D., Bhattarai, T.P., 2013. Estimation of soil erosion rates and eroded sediment in a degraded catchment of the Siwalik Hills, Nepal. Land. 2(3): 370-391.

Lawler, D.M., 1993. The Measurement of River Bank Erosion and Lateral Channel Change - A review Earth Surface Processes and Landforms. 18(9): 777-8 21.

Li, L., Collins, R., Zhang, X., Wei, H., 2014. A Photogrammetric Method to Evaluate the Erosiveness of Fairbanks Silt with Different Treatments. In Climatic Effects on Pavement and Geotechnical Infrastructure. ASCE Publications. 176-182 p.

Li, S., 2012. Soil erosion and conservation. Encyclopedia of environmentrics, 2nd edition. John Wiley & Sons, Ltd.

Matthews, N. A., 2008. Aerial and Close-Range Photogrammetric Technology: Providing resource documentation, interpretation, and preservation. Technical Note 428. U. S. Department of the interior, Bureau of Land Management, National Operations Center, Denver, Colorado. 42 p.

Miri, M., Varshosaz, M., 2011. Evaluating parameters affecting the georeferencing accuracy of terrestrial laser scanners. International Archives of the Photogrammetry, Remote Sensing and Spatial Information Sciences. 38: 5/W16.

Nasermoaddeli, M.H., Pasche, E., 2008. Application of terrestrial 3D laser scanner in quantification of the riverbank erosion and deposition. Proceedings of Riverflow. 3-5 p.

Perroy, R.L., Bookhagen, B., Asner, G.P., Chadwick, O.A., 2010. Comparison of gully erosion estimates using airborne and ground-based LiDAR on Santa Cruz Island, California. Geomorphology. 118(3): 288-300.

Poesen, J., Nachtergaele, J., Verstraeten, G., Valentin, C., 2003. Gully erosion and environmental change: importance and research needs, Cantena. 50: 91–133.

Rejman. J and Brodowki, R., 2005. Rill characteristics and sediment transport as a function of slope length during a storm event on loess soil. Earth Surface Processes and Landforms. 30: 231-239.

Samad, A.M., Ahmad, A., Ishak, N., 2010. Assessment of digital camera for mapping stream using close range photogrammetric technique. Proc. 20106th Int. Colloq. Signal Process. Its Appl. (CSPA). 1 -5 p.

Schmid, T., Schack-Kirchner, H., Hildebrand, E., 2004. A case study of terrestrial laser scanning in erosion research: calculation of roughness and volume balance at a logged forest site. In Proceedings of the ISPRS Working Group VIII/2: Laser-Scanners for Forest and Landscape Assessment. 3-6 p.

Stott, T. A., 1997. Comparison of stream bank erosion processes on forested and moorland streams in the Balquhidder catchments, Central Scotland. Earth Surf. Process. Landf. 22: 383–399.

Ventura, G., Vilardo, G., Terranova, C., Sessa, E.B., 2011. Tracking and evolution of complex active landslides by multi-temporal airborne LiDAR data: The Montaguto landslide (Southern Italy). Remote Sensing of Environment. 115(12): 3237-3248.

Vinci, A., Brigante, R., Todisco, F., Mannocchi, F., Radicioni, F., 2015. Measuring rill erosion by laser scanning. Catena. 124: 97-108.

Welch, R., T. Jordan., 1983. Analytical Non-metric Close-Range Photogrammetry for Monitoring Stream Channel Erosion, PE & RS. 49(3): 367-374.

Welch, R., Jordan, T. R., Thomas, A. W., 1984. A photogrammetric technique for measuring soil erosion, Journal of soil and water conservation. 39(2): 191-194.

Chapter 2

Assessing the accuracy of total station scanning and close-range photogrammetry for quantifying soil surface morphology

Abstract

Ground-based remote sensing technologies such as 3D scanner and photogrammetry have been utilized widely to detect surface morphology. However, studies up to date have focused on assessing the accuracy of the methods on detecting vehicle accident, the geometry of building, coastal change and etc. There is a lack of information about what are the performances of the ground-based remote sensing technologies on detecting soil morphological change under different scenarios.

In this study, the performances and accuracies of total station scanner (TSS) and close-range photogrammetry (CRP) methodologies on detecting morphological features were evaluated and optimized. By comparing the results for (i) a ridged and channeled plywood board (2.4 m by 3.6 m) and (ii) a ridged and channeled bare-earth plot (6 m by 20 m) derived from both methods with the actual measurement. For the plywood board assessment, the optimal TSS and CRP root mean square errors were: width = 1.3 cm vs. 0.8 cm; depth = 1.0 cm vs. 0.4 cm; areas = 7.8 cm^2 vs. 4.2 cm^2. Whereas for the bare-earth plot, the optimal TSS and CRP root mean square errors were: width = 3.4 cm vs. 1.1 cm; depth = 2.2 cm vs. 1.6 cm. Hence, both assessments indicated that the CRP results are better than the TSS results. However, TSS is more practical than CRP by allowing larger scanning distances and fewer operators. By comparing the different setups of TSS and CRP, the best TSS result was observed on the middle position and the best CRP results were observed with the largest shooting angle and the largest overlap rate.

2.1 Introduction

Soil surface morphology plays an essential role in many soil biophysical processes, such as runoff generation and organic matter distribution. However, soil surface morphology is strongly affected by many land management practices, in particular, tillage operations. Tillage operations often completely change the soil surface micromorphology, and may be designed to create or obliterate morphological features, such as channels and ridges. Soil surface morphology is also affected by soil biophysical processes, such as gravitational subsidence after tillage, wet/dry cycle, and freeze/thaw cycle. However, the soil biophysical process that has the strongest impact on soil surface morphology is probably soil erosion. For example, water erosion often creates morphological features such as rills and gullies. In addition, soil loss on the eroding portion and soil accumulation at soil deposition spots can result in elevation changes in these areas. In fact, due to the strong impact of soil erosion on surface morphology, many methods have been developed to assess the soil erosion rate by measuring surface morphological change.

The manual survey method has been widely used to assess the dimensions and density of rills in a field, as a traditional and accurate way for measuring rill erosion (Bewket and Sterk, 2003). A study by Herweg (1996) indicated that a carefully implemented survey usually has errors less than 15%. However, Bewket and Sterk (2003) indicated that survey results cannot be used as accurate estimations for soil loss due to inter-rill erosion. Inter-rill erosion can be measured using another

traditional method, the erosion pin. With the erosion pin method, a set of erosion pins are often inserted into the ground; the distance between ground level and a mark on the erosion pin is measured over time, creating a record for soil loss or accumulation (Ghimire et al., 2013). Several other studies have also employed erosion pins to monitor stream bank erosion (Couper et al., 2002; Lawler et al., 1997; Stott, 1997). A recent study by Ghimire, Higaki and Bhattarai (2013) used erosion pins to measure different types of soil erosion in Nepal, such as sheet erosion, gully erosion, landslide and bank erosion. The accuracy of morphological change derived from erosion pin measurements usually is larger than ~1 mm, which is equivalent to a soil loss of ~11 t ha^{-1}. Traditional methods, such as the manual survey and erosion pins, may disturb the natural conditions of the area, and may possibly cause additional erosion. Erosion pins can also be disturbed by animal or human interference. In addition, considerable time and effort are necessary to acquire high spatial and temporal resolutions using these traditional methods.

Remote sensing is a technological method used to obtain information about an object or phenomenon without physical contact (Schowengerdt, 2007). It can be divided into passive and active remote sensing. With passive remote sensing, sensors collect radiation reflected back by the target or surrounding areas. Visual light photography and infrared thematic mapping are two examples of passive remote sensors. With active remote sensing, sensors actively emit a signal to scan target or surrounding areas and then collect the backscatter signals. Examples of active sensors include

Light Detection and Ranging (Lidar), Radio Detection and Ranging (Radar), and Sound navigation and ranging (Sonar), which measures the time delay between sending and receiving of a signal to identify targets.

With the technical improvement, the ground-based or close-range version of 3D scanner and photogrammetry provide potential solutions to break out of these limitations. Since it is much easier to move and operate those ground-based systems than their airborne versions, a higher temporal resolution of surface morphology can be acquired. Both ground-based technics have been applied in the water erosion studies (Berger et al., 2010; Gessesse et al., 2010, Milan et al., 2007; Nadal-Romero et al., 2015; Nasermoaddeli and Pasche, 2008; Peter Heng et al., 2010; Schmid et al., 2004; Vinci et al., 2015). Besides, some studies used close-range photogrammetry to characterize soil surface roughness (Abd Elbasit et al., 2009; Aguilar et al., 2009; Blaes and Defourny, 2008; Rieke-Zapp et al., 2001; Taconet and Ciarletti, 2007; Zribi et al. 2000), which is an important parameter in water interaction processes.

Both remote sensing methods have several advantages compared to the traditional methods such as relative fine resolution, quick data acquisition, mobility, repeatability and no extra disturbance of soil surface. However, how accurate of both remote sensing technologies on detecting morphological changes? Some accuracy studies of remote sensing methods have been done in last decades. In 2003, Boehler and Marbs conducted an investigation to compare the accuracy of laser scanners of different manufacturers under one setting. Some factors which may affect the

accuracy were tested such as shooting angle, distance range, object edge, object surface reflectivity and environmental conditions. Miri and Varshosaz (2011) also evaluated the parameters which affect the accuracy of the scanner such as the distance to laser scanner and the shooting angle between the surface and scanner beam. The results showed that there was a trend of decreasing accuracy with increasing distance and shooting angle. For the photogrammetry method, Ali et al. (2000) studied the factors that influence the accuracy of photogrammetry under one particular setting, indicating that the drop of the elevation of the camera or the increase of the distance between two cameras increased the vertical accuracy significantly. Besides, the accuracies of both remote sensing methods for different surface morphology applications were quantified in many studies. The accuracy of 3D scanning-derived digital terrain model was investigated by Aguilar and Mills (2008); Montane and Torres (2006) and Salleh et al. (2015) with different approaches. Butler et al. (1998) and Samad et al. (2010) conducted accuracy assessments of close-range photogrammetry for characterizing surface roughness and mapping streams respectively.

However, no accuracy assessment of both technologies has been conducted for detecting the surface morphological change. Moreover, no study has investigated the accuracies of both methods at different settings or the applicability of them under various scenarios. There is a lack of information about what are the performances of

the ground-based remote sensing methods on detecting morphological change under different settings. Therefore, the objectives of this study are:

1. To estimate the accuracies of the Total station scanning (TSS) and Close-range photogrammetry (CRP) method under different settings on detecting morphological features and measuring elevation differences;
2. To assess the applicability of the TSS and CRP method under various scenarios with spatial, temporal and resource constraints.

2.2 Materials and Methods

2.2.1 Equipment

2.2.1.1 Total station scanning (TSS)

For the total station scanning method, a Trimble VX spatial station was used. On the top of the basic survey functions of a traditional total station, the Trimble VX is equipped with a camera and includes a 3D scanning function for collecting a large number of points within a user-defined area at user-specified horizontal and vertical intervals. Setting up the Trimble VX for scanning is relatively simple. The unit only needs to be placed at a stable location (often mounted on a tripod) and be leveled. The detection range for scanning can reach 150 m and the speed for scanning is typically 5 points/sec. The accuracy of a single 3D point can reach 10 mm within 150 m.

2.2.1.2 Close-range photogrammetry (CRP)

For the close-range photogrammetry method, Nikon D7000 cameras were used. The Nikon D7000 is based on a DX-format (23.6 x 15.6mm) CMOS image sensor with 16.2 effective megapixel resolution, from a total resolution of 16.9 megapixels. The D7000's image has a pixel size of 4.78μm, and yields maximum image dimensions of 4,928 x 3,262 pixels (Nikon Corporation, 2010). The camera body weighs approximately 690 g and is convenient to carry in the field. In this study, an AF Nikkor 24 mm f/2.8D lens was used and calibrated at a focal distance of 5 m so that distortion of the lens can be adjusted. The calibration procedure was developed following the requirement of the PhotoModeler Scanner® software. A detailed description of the calibration procedure can be found in Appendix I. In brief, specially designed targets provided by PhotoModeler Scanner® were printed and were taped onto a wall, covering an area of approximately 10 m x 10 m, which was used as the test field (Fig. 2.1). The camera was firstly placed at 5 m distance from the wall. The lens was adjusted to focus on the wall and then was taped to avoid any change in focusing distance. A set of photos were taken at different angles and distances (4 – 6 m). These photos were imported into the PhotoModeler Scanner® software, which can identify each target automatically. A built-in algorithm then uses the multiple photos of the same test field to adjust the distortion of the lens.

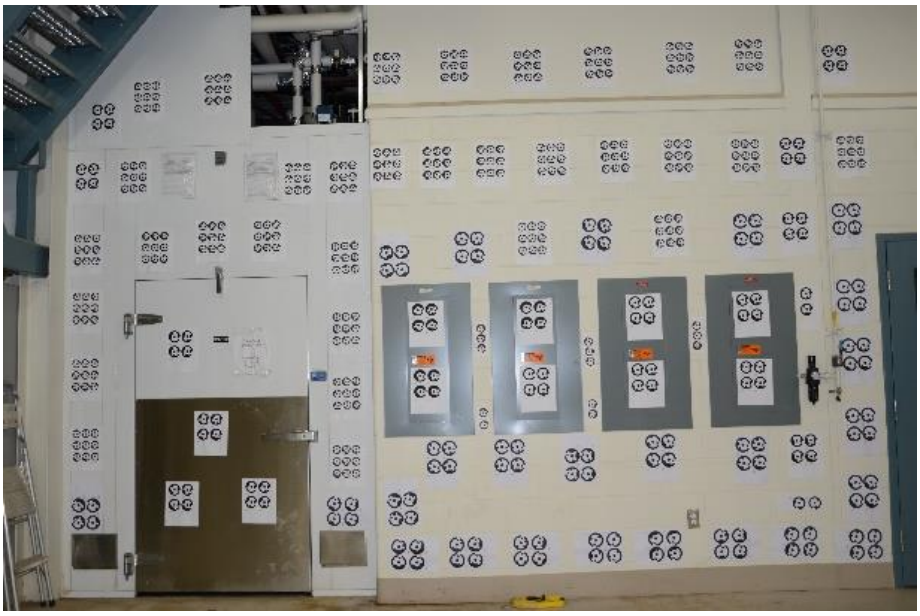

Figure 2.1. Test field for calibration of the photogrammetry methodology.

The close-range photogrammetry was conducted with a frame (CRP-F), a 2 m x 6 m aluminum platform with legs and poles for installing the cameras (Fig. 2.2). Legs with wheels were welded to the four corners of the platform so it sits at a height of ~1.1 m and can be moved easily. Two brackets were established on the platform to install the poles for holding a pair of cameras. The two poles were 2.1 m apart from each other, each centered at a location 1.95 m away from the side of the platform. The brackets allowed the two poles to be fixed on the platform. The heights of the poles were adjustable. A camera base was installed on the top of each pole. The angle of the camera base was adjustable so that the view angle of the camera was also adjustable. Each camera was connected through a long cable to a laptop computer and was controlled using the DCamCapture software for photo shooting. During the photo shooting, the poles were firstly lowered so the cameras can be mounted on the base and then the poles were raised to desirable height (6 m above the ground maximum).

The platform was established at the starting position and a pair of photos was taken. Then the platform was moved along a straight path and stops were made at a given distance interval and a pair of photos were taken at each stop.

Figure 2.2. Aluminum platform (6 m wide and maximum 6 m high) for CRP method.

To further test the limit of the close-range photogrammetry, it was tested by hand-holding the camera (CRP-H). In these tests, the focusing distance of the lens was not fixed. The lens was autofocused to the board surface firstly. Then, the camera was switched to the manual focusing mode so that the focusing distance will not change during one set of photo shooting. Calibration for lens distortion was performed by the PhotoModeler Scanner® software automatically using a built-in algorithm with multiple (more than 8) overlapped photos. The effect of camera height was tested with two positions of the photographer, on the ground (CRP-H1) and on the stand (CRP-H2). For CRP-H1, the camera was at ~1.2 m above the

ground and for CRP-H2, it was at ~2.0 m above the ground. The effect of shooting angle (the included angle between the horizontal line and the shooting direction) was also tested with a series of shooting angle settings (details below).

2.2.2 Indoor board test

Plywood boards were used to build an approximate 2.4 m x 3.6 m board surface (Fig. 2.3). Two by four lumbers (approximately 3.6 cm x 8.6 cm) were fixed onto the board surface to make seven Artificial Morphological Features (AMF, Table. 2.1), mimicking the morphological types observed in the field (i.e. channel and ridge).

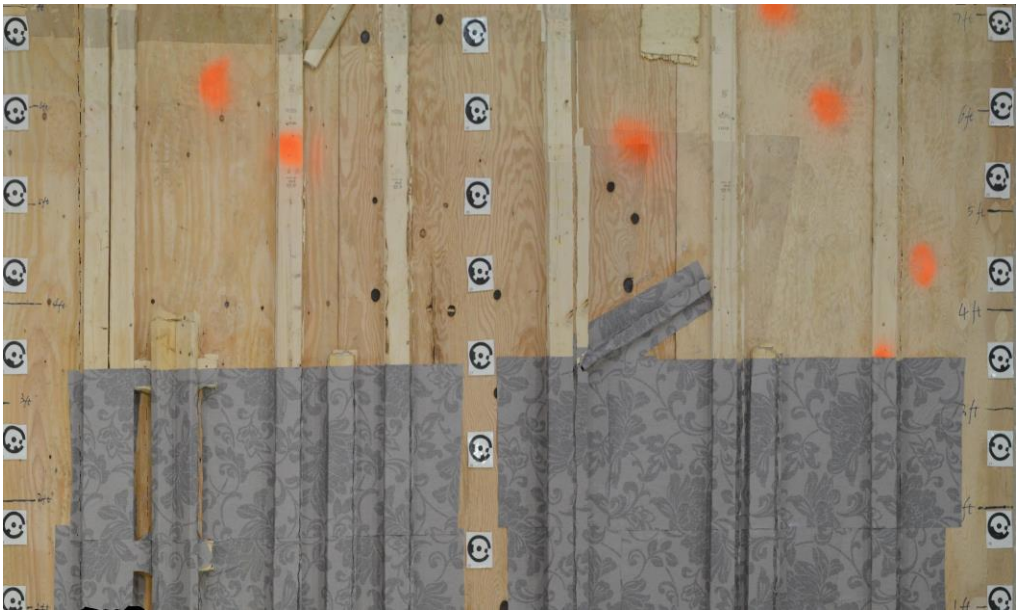

Figure 2.3. Manmade plywood surface for assessing remote sensing methods.

Dimensions of these AMFs were manually measured using a tape measure to determine three parameters characterizing the geometry of these AMFs: the widths, depths/heights, and cross-sectional areas. These parameters were determined at 2 locations along each AMF. The differences between the 2 locations were minimal so

that average values of the 2 locations were used as reference values (Table. 2.1) characterizing the AMFs.

Table 2.1. Measured value (width, depth and area) of each artificial morphological feature (AMF) for the indoor test.

AMF #	1	2	3	4	5	6	7
Description	Wide square ridge	V-shape channel	Wide square channel	Medium square ridge	High square ridge	Narrow square channel	Medium square ridge
Acronym	WSR	VSC	WSC	MSR	HSR	NSC	MSR
Width (cm)	18.7	11.2	10.2	8.6	8.6	5	8.7
Depth (cm)	3.6	4.3	3.7	3.8	7.6	3.6	3.9
Area (cm^2)	67.3	24.1	37.7	32.7	65.4	18	33.9

For the TSS method, the Trimble VX was mounted on a tripod at a height of ~1.5 m above the ground. The total station was located along the center line of the board, 5 m away from its edge. The scanning was conducted at spacings of approximately 1 cm horizontally and 1 cm vertically at 6.5 m distance. A total of 95596 raw data points were collected.

For the CRP method, plastic target plates were installed on the board surface in three rows at an interval of 0.3 m (Fig. 2.3). For CRP-F, The two cameras were raised on the pole to approximately 5 m above the ground. Horizontal shooting angles for both cameras were set at 70°. Each photo covered and area of approximately 4.9 m x 4.3 m on the ground and the overlap rate for the paired photos was around 60%. For the first pair of photos, the platform was located 10 m away from the board. The platform then was moved towards the board and subsequent photo pairs were taken at 1.5 m interval, obtaining a longitudinal (along the moving path of the platform)

overlap rate of approximate 80%. In total, 34 photos were taken to cover the entire board surface.

For CRP-H, all photos were taken along the two long edges of the board surface. For all photos, the photographer was located ~0.2 m to ~0.5 m away from the long edges of the board and the camera was facing toward the surface. The first photo was taken at one corner of the board, then the photographer moved along the long edge and subsequent photos were taken at 0.5 m interval, ensuring a horizontal overlap rate of at least 60%. The same procedure was repeated for the other edge to take another pair of photos. In total, 16 photos were taken to cover the entire surface. Two camera height treatments (CRP-H1 and CRP-H2) and four shooting angle treatments (approximately at 90°, 70°, 45° and 20°) were applied.

2.2.3 Outdoor field test

To exam the performance of the two remote sensing methods under real field conditions, a field test was conducted. The field site (Fig. 2.4) for this test was located on a slope (~10% slope gradient) in the experimental farm of the Fredericton Research and Development Centre (FRDC). A 6 m wide and 20 m long field section was tilled up-down-slope for multiple times and was harrowed to create a relatively smooth surface. On one side of the field, three potato hills were created using a potato hill. The hills were trapezoidal in shape with a height of ~30 cm and a spacing of ~91 cm. On the other side of the field, two up-down-slope channels were manually dug using a specially made hoe (10 cm by 10 cm). One channel was made

to be approximately 10 cm wide by 10 cm deep and the other one 20 cm wide by 15 cm deep. The smaller channel was ~1 m away from the field edge and the larger channel was between the potato hill and the smaller channel (~1.2 m away from the smaller channel).

Figure 2.4. Bare-earth plot for assessing remote sensing methods.

Morphological parameters of these AMFs (width and depth) were manually measured along 5 cross-sectional transects. Average values of these manually measured parameters were used as “true” values (Table. 2.2) to validate the remote sensing methods.

Table 2.2. Measured value (width and depth) of each artificial morphological feature (AMF) for the outdoor test.

AMF #	1	2	3	4
Description	Narrow channel	Wide channel	Channel between potato hills	Channel between potato hills
Acronym	NC	WC	CBH1	CBH2
Width (cm)	10	20	91	91
Depth (cm)	10	15	19	19.4

For the TSS method, the Trimble VX was always set at a height of 1.5 m above the ground and at a distance of 5 m down slope the field edge. However, three horizontal positions (i.e., left, middle and right) were tested. For the middle position, the Trimble VX was aligned with the center line of the field whereas for the left and right position, the Trimble VX was ~2 m left and right of the center line, respectively. The scan was conducted at 1.5 cm horizontal and vertical intervals at 15 m distance. Overall, a total of 244423 points were collected for the entire field section.

For the CRP method, plastic target plates were installed on both sides of the field at an interval of ~1 m. Cameras were set up on the platform the same as in the board test. In particular, the heights of the cameras were ~5 m above the ground and horizontal shooting angles for both cameras were set at 70° as well. However, different horizontal and longitudinal overlaps were tested. The first pair of photos was taken at 5 m away from the plot. The platform was moved downwards the plot and subsequent photo pairs were taken at different intervals (Table. 2.3), and the default setup of two poles was 2.1 m apart from each other, so each photo covered

and area of approximately 4.9 m x 4.3 m on the ground and the horizontal overlap rate for the paired photos was around 60%. In order to test different horizontal overlaps, an aluminum post was installed onto the top of two poles. Several pairs of holes were drilled on the post at different spots to mount two cameras (Table 2.3). The center of the aluminum post was lined up with the center of the platform. In total, the number of photos which were taken to cover the entire field varies from 14 to 82 due to different overlap rates.

Table 2.3. Camera distance (m) and photos taking interval (m) for different overlap rates (%).

Horizontal Overlap	57%	49%	39%	29%	18%
Camera Distance (m)	2.1	2.5	3.0	3.5	4.0
Longitudinal Overlap	88%	77%	53%	30%	7%
Photos Taking Interval (m)	0.5	1.0	2.0	3.0	4.0

The further test of the CRP method was conducted as well; photos were taken by hand-holding the camera and the camera was facing toward the surface. The photographer moved along two long edges and subsequent photos were taken at 0.5 m interval as same as the indoor board test. In both cases, two height treatments (CRP-H1 and CRP-H2) and 4 shooting angle treatments (90°, 70°, 45°, 20°) were used to capture entire field. In total, 42 photos were taken for each shooting angles at different camera heights.

2.2.4 Data extraction and analysis

For the TSS method, the collected raw data were 3D point locations that could be directly used to derive the surface morphology model whereas for the CRP method,

the raw data were photo images. These photo images were imported into PhotoModeler Scanner®, which uses an algorithm based on the scale-invariant feature transform (SIFT) developed by Lowe (2004) to extract point cloud with 3D point location information. For both methods, the 3D point location data were imported into Surfer® and default kriging interpolation was used to generate grid format DEMs. For the indoor board test, all DEMs generated were in 1 cm resolution (cell size = 1 cm) and for the outdoor field test, all DEMs generated were in 1.5 cm resolution (cell size = 1.5 cm). The resolution was set to match the raw data resolution of the TSS method. After the DEMs were generated, randomly selected 10 and 5 cross-sectional transects, 10 for the indoor board test and 5 for the outdoor field test, respectively, were extracted. Morphological parameters (cross-sectional areas, width, and depth) for the shapes and AMFs (i.e., ridges, channels, and potato hills) were calculated on each transect using tools provided in Surfer®. For a given method, the average value of a morphological parameter from all transects was calculated. The accuracy of the method was assessed by comparing the value derived from the DEMs to the value derived from manual measurements. The uncertainty of the method was evaluated using Root Mean Square Error (RMSE), defined as:

$$\mathrm{RMSE} = \sqrt{\frac{\sum_{i=1}^{N}(X_i - X_{Ref})^2}{N}}$$

Where: X_i is the parameter value for the i^{th} transect and Ref denotes reference value.

Besides, the precision of the method was assessed by comparing the values derived from the DEMs to the average of these values. Therefore, Standard deviation (SD)

was used as a measure to evaluate uncertainty for different methods as well, and it is defined as:

$$SD = \sqrt{\frac{\sum_{i=1}^{N}(X_i - \overline{X})^2}{N}}$$

Where: X_i is the parameter value for the i^{th} transect and $\overline{X}$ indicates average parameter value of all N transects. In both calculations, a lower value indicates a better method to detect a surface or a field.

For the indoor board surface, an additional test was conducted on the extracted DEMs to examine whether there are zonal differences in the measurements. For this test, the board was divided into nine same-sized zones (~120 cm x 80 cm, Fig. 2.5). In each zone, the elevation difference between the board base and the top of the lumber in this zone was manually measured. The same parameter was calculated from the DEMs by subtracting the average elevation of the points in selected area on the board base from that of points in selected area on the lumber top.

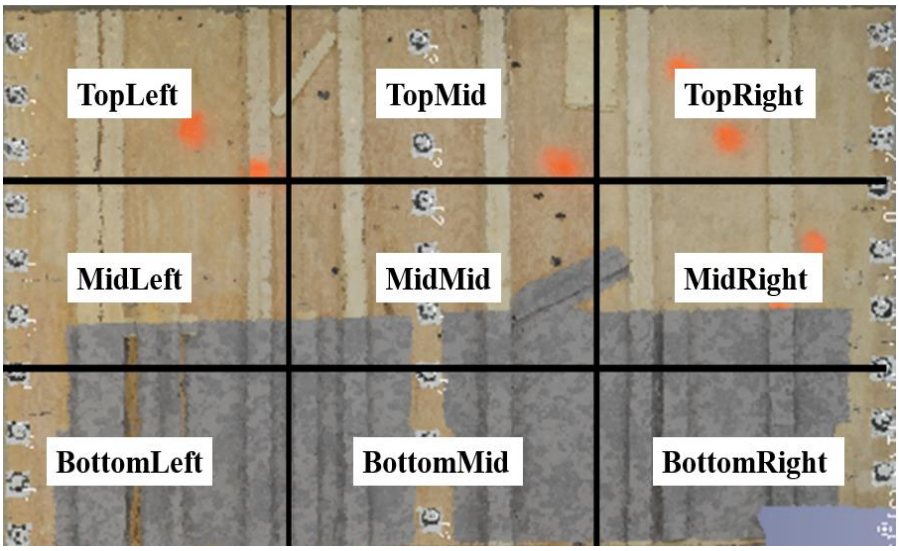

Figure 2.5. Nine zone labels of manmade plywood surface.

For the outdoor field, another test was conducted to exam whether there are zonal differences visually. In this case, the AMFs were not well-defined square in shape so that the “true” values of morphological parameters for the whole area were not able to be measured correctly. The statistical analysis of the outdoor field test was able to provide the most accurate method on detecting AMF among all settings. DEM extracted from the most accurate method was treated as the reference DEM to compare with the other DEMs extracted from the other methods. The comparisons were derived from the DEMs by subtracting the reference DEM from the DEMs extracted from the other methods.

In additional, for both indoor and outdoor tests, the applicability of both remote sensing methods on detecting AMFs was tested by comparing equipment, number of operator, time consumptions and detection range (Fig. 2.6). For this test, the equipment, the # of operator and the time consumption of each method were recorded during experiments. Besides, the detection ranges were estimated. For the TSS, the detection range was determined by the scanner of total station whereas for the CRP methods, those with different settings were determined based on the camera field of view and shooting angles.

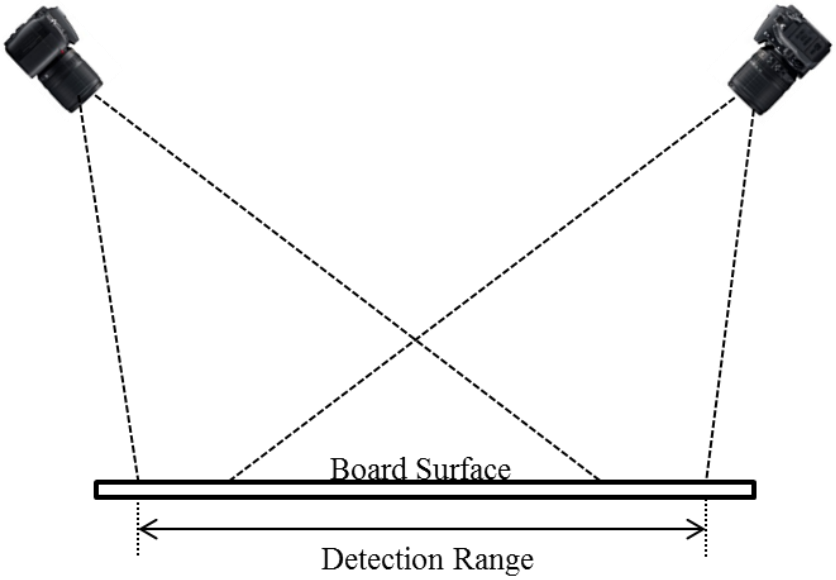

Figure 2.6. Illustration of detection range for the handheld CRP methods.

2.3 Results and Discussion

2.3.1 Indoor board test

2.3.1.1 Visual observations

Figure 2.7 illustrates example transect derived from each remote sensing technology, compared with transect drawn from manually measured data (on the top).

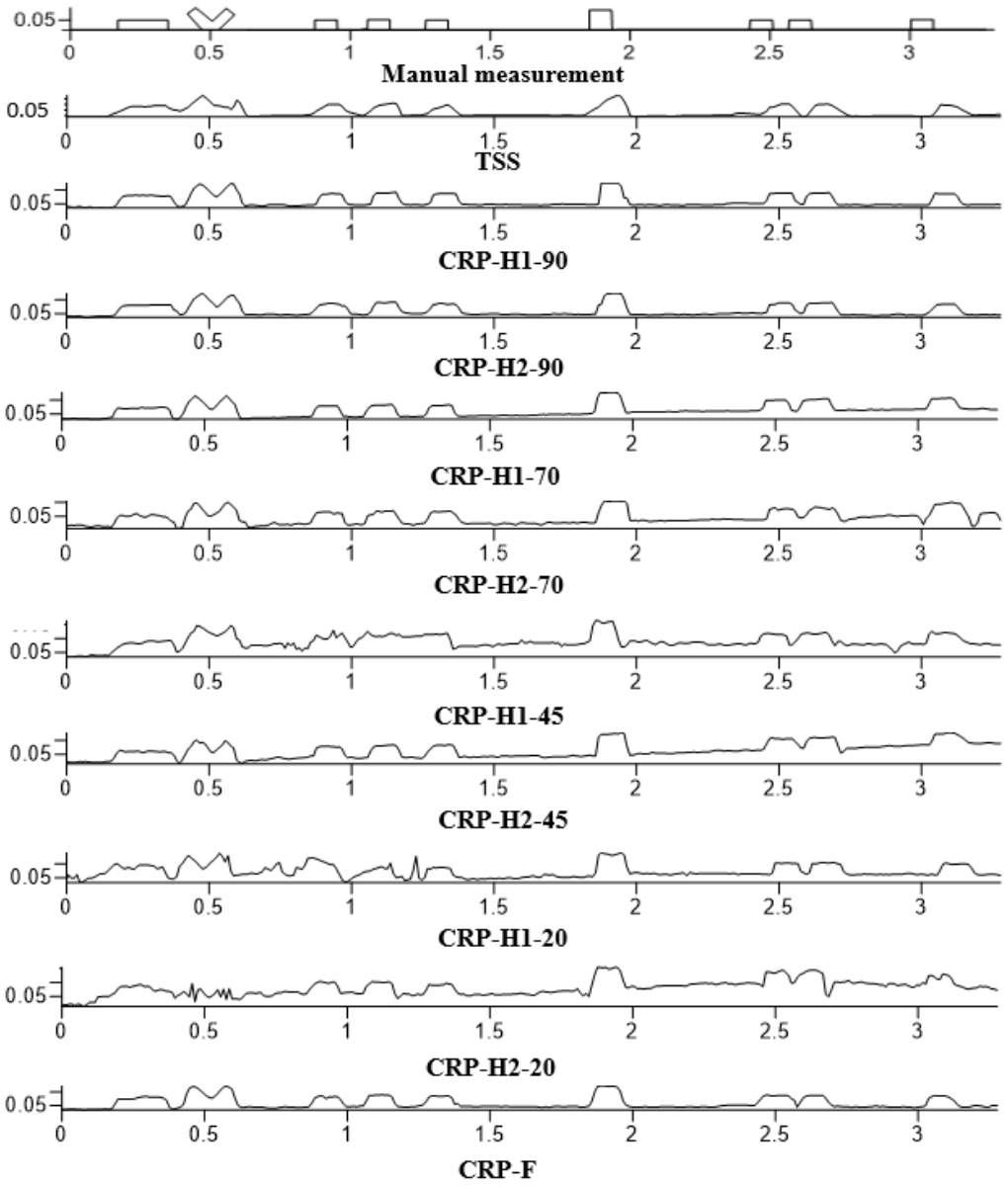

Figure 2.7. A transect extracted from each DEM generated using different remote sensing methods for the indoor test.

All the methods were able to correctly identify the location of each AMF. Visually, it appeared that the TSS method produced smoother transect but it displayed triangle shapes for AMFs that are square in shape. The CRP methods had higher local variations (e.g., higher noises in the flat area) than the TSS method and among the handheld CRP methods. There was a clear trend of rougher surface with lower

shooting angle, indicating the high errors associated with the low shooting angles. However, most square shaped AMFs extracted using the CRP methods were trapezoidal in shape, with a flatter top and sloping sides, which were closer to the true square shapes than the triangle shapes extracted using the TSS method. The smoother surfaces of the TSS method were probably a reflection of the amount of its raw data points, which were typically only about 1% of those with the CRP methods. The sloping sides extracted with the CRP methods were likely a result of the shadow effect during photograph shooting—when there is a shooting angle, there will be a shadowed area at the corner of a straight wall. For the two height settings of the handheld CRP methods, the CRP-H2 method provided smoother transect than the CRP-H1 except for the CRP-H-20 method. The CRP-F method extracted transect was close to those of the CRP-H-90 and CRP-H-70 methods, which were the best among all methods.

For AMF #6 (Narrow Square Channel - NSC), the extracted shapes from all tested remote sensing methods were triangles, indicating the difficulty of detecting narrow morphological features with these methods. The TSS method provided a smoother surface which tends to overestimates the width of this narrow channel. Whereas the CRP methods showed less smoothing effect, they were not able to detect the bottom of the channel, likely a result of strong shadow effects when the opening space between the walls was too narrow. For AMF #2 (V-shape Channel - VSC), the TSS method was not able to detect the shape well, with the center of the V-shape channel

moved to the right and the two side slopes poorly defined. The CRP methods, on the other hand, were all able to produce the V-shape with approximately symmetric side slopes, except for CRP-H-20.

2.3.1.2 Width of the AMFs

Measured and DEM-extracted values for the three parameters (width, depth, and cross-sectional area) of the seven AMFs were summarized in the following tables (Table 2.4; Table 2.5; Table 2.6).

Table 2.4. Average width (cm), SD (cm) and RMSE (cm) of each morphological feature derived from manual measurement & different remote sensing methods for the indoor test.

	Methods	#1 Wide Square Ridge	#2 V-shape Channel	#3 Wide Square Channel	#4 Medium Square Ridge	#5 High Square Ridge	#6 Narrow Square Channel	#7 Medium Square Ridge	Average
Average	Measured width (cm)	18.7	11.2	10.2	8.6	8.6	5.0	8.7	
	TSS	18.2	12.2	9.7	9.2	9.9	5.8	9.6	
	CRP-H1-90	19.8	11.3	9.9	9.3	9.1	4.2	9.7	
	CRP-H2-90	19.2	11.0	9.4	9.2	9.1	3.9	9.6	
	CRP-H1-70	19.8	10.9	9.3	9.4	9.3	4.1	9.9	
	CRP-H2-70	19.8	10.8	8.7	9.7	9.6	4.0	10.2	
	CRP-H1-45	21.0	12.0	6.9	9.1	8.6	4.0	10.4	
	CRP-H2-45	21.0	9.7	9.1	9.9	9.9	3.9	10.5	
	CRP-H1-20	19.4	9.7	8.3	9.8	11.5	4.1	11.1	
	CRP-H2-20	18.7	6.8	9.4	9.8	9.4	3.6	10.3	
	CRP-F	19.4	10.9	8.7	10.2	9.8	4.1	9.3	
SD	TSS	1.1	1.5	1.3	1.1	1.3	0.7	0.7	1.1
	CRP-H1-90	0.6	0.5	0.8	0.6	1.0	0.4	1.0	0.7
	CRP-H2-90	0.6	0.2	0.4	0.4	0.6	0.4	0.6	0.5
	CRP-H1-70	0.4	0.2	0.4	0.3	0.9	0.4	0.4	0.4
	CRP-H2-70	0.6	0.4	1.2	0.6	0.7	0.3	0.6	0.6
	CRP-H1-45	0.5	1.1	1.3	3.2	0.6	0.5	0.6	1.1
	CRP-H2-45	2.1	2.3	0.6	0.4	1.4	0.3	0.9	1.1
	CRP-H1-20	3.5	1.9	3.1	0.7	1.2	0.4	0.5	1.6
	CRP-H2-20	4.3	3.2	0.6	0.4	0.8	1.1	0.7	1.6
	CRP-F	2.4	0.4	0.4	0.7	1.3	0.3	1.0	0.9
RMSE	TSS	1.2	1.7	1.2	1.2	1.8	1.0	1.1	1.3
	CRP-H1-90	1.3	0.5	0.8	0.9	1.1	0.9	1.4	1.0
	CRP-H2-90	0.8	0.3	0.9	0.7	0.8	1.2	1.1	0.8
	CRP-H1-70	1.2	0.3	1.0	0.8	1.1	0.9	1.3	0.9
	CRP-H2-70	1.2	0.5	1.9	1.2	1.2	1.1	1.6	1.2
	CRP-H1-45	2.3	1.3	3.5	3.0	0.6	1.1	1.8	2.0
	CRP-H2-45	3.1	2.6	1.2	1.3	1.8	1.1	2.0	1.9
	CRP-H1-20	3.4	2.3	3.4	1.3	3.1	1.0	2.4	2.4
	CRP-H2-20	4.1	5.3	0.9	1.3	1.1	1.7	1.7	2.3
	CRP-F	2.3	0.5	1.6	1.7	1.7	0.9	1.1	1.4

Both the TSS and CRP methods were able to provide good width values. Except for those for the AMF #6 (NSC), most of the estimated width values were close to the measured values, having errors less than 20% (Table 2.4). The accuracy of TSS was similar to those of the CRP-H1-90 and CRP-H2-90, which were the best among all settings of the CRP method. For the handheld CRP method, there was not much

difference between H1 and H2 but there was a clear trend of decreasing accuracy (i.e., increasing error) with the decrease of the shooting angle. Errors with shooting angles of 90˚ and 70˚ were mostly < 10% whereas those with shooting angles of 45˚ or 20˚ were mostly > 15%. The accuracy of the CRP-F method was at approximately the same level as those of the CRP-H1-70 and CRP-H2-70, probably because the shooting angle of CRP-F was approximately 70˚.

For the CRP methods, except for a few cases, there was a consistent trend of underestimation of channel width and overestimation of ridge width for all AMFs. Such trend was not observed for the TSS (Table 2.4). This may be a reflection of the principles behind the two methods. For the CRP methods, the strong shadow effects at corners of straight walls tended to create sloping sides that extended beyond the edges of ridges and tilted into channels, resulting wider ridges but narrower channels. For the TSS method, the SD values of width were mostly > 1 cm whereas for the CRP method, they were mostly < 1 cm. Among the handheld CRP methods, there was not much difference in SD value between the two height settings and a trend of increasing SD value with decreasing shooting angles can be observed except for the CRP-H1-70 method. Most SD values with shooting angles of 90º and 70º were < 0.6 cm whereas around half of those with shooting angles of 45º and 20º were > 1 cm, indicating a decreasing precision with the decrease of shooting angles. Except for the AMF #1 (Wide Square Ridge - WSR), SD values of CRP-F for all AMFs were at a

similar level as those for the CRP-H-90 and CRP-H-70, which were the lowest among all methods.

Trends for the RMSE values (indicating absolute accuracy) among all remote sensing methods were similar to those for the SD values. The RMSE values of the TSS method were at the same level as those of the CRP-F and handheld CRP methods with shooting angles of 70˚ or 90˚. Among the handheld CRP methods, there was little difference between the two height settings and there was a trend of increasing RMSE (with the drop of shooting angles. Overall, the RMSE values suggested that the absolute accuracy of CRP-H2-90 was the best among all methods.

2.3.1.3 Depth of the AMFs

Table 2.5. Average depth (cm), SD (cm) and RMSE (cm) of each morphological feature derived from manual measurement & different remote sensing methods for the indoor test.

	Methods	#1 Wide Square Ridge	#2 V-shape Channel	#3 Wide Square Channel	#4 Medium Square Ridge	#5 High Square Ridge	#6 Narrow Square Channel	#7 Medium Square Ridge	Average
Average	Measured depth (cm)	3.6	5.5	3.6	3.8	7.6	3.6	3.9	
	TSS	2.5	3.5	3.5	3.3	6.7	3.2	3.4	
	CRP-H1-90	4.0	4.6	3.9	3.8	7.7	3.9	3.8	
	CRP-H2-90	3.7	3.7	3.8	3.8	7.7	3.8	3.9	
	CRP-H1-70	3.9	4.7	4.0	3.9	7.6	3.9	3.8	
	CRP-H2-70	4.1	4.7	4.1	4.2	7.6	3.6	4.1	
	CRP-H1-45	3.8	3.7	5.0	3.8	8.0	4.1	4.1	
	CRP-H2-45	4.2	4.2	4.2	4.1	7.7	3.7	3.9	
	CRP-H1-20	5.0	4.3	5.8	3.8	8.0	3.7	4.0	
	CRP-H2-20	4.2	4.5	4.7	4.1	8.8	4.3	4.1	
	CRP-F	4.0	3.7	3.9	3.7	7.5	3.2	3.8	
SD	TSS	0.5	1.2	0.3	0.4	1.2	0.5	0.3	0.6
	CRP-H1-90	0.3	0.1	0.1	0.1	0.2	0.1	0.2	0.2
	CRP-H2-90	0.2	0.6	0.2	0.1	0.2	0.3	0.1	0.2
	CRP-H1-70	0.2	0.3	0.1	0.2	0.2	0.1	0.2	0.2
	CRP-H2-70	0.3	0.5	0.3	0.2	0.5	0.3	0.3	0.3
	CRP-H1-45	0.6	0.5	1.2	0.9	0.9	0.4	0.3	0.7
	CRP-H2-45	1.2	0.4	0.1	0.4	0.2	0.3	0.1	0.4
	CRP-H1-20	1.8	0.6	0.3	0.2	0.2	0.8	0.1	0.6
	CRP-H2-20	0.8	1.0	0.6	0.6	0.3	0.2	0.4	0.6
	CRP-F	0.5	0.7	0.2	0.2	0.3	0.7	0.2	0.4
RMSE	TSS	1.2	2.3	0.3	0.6	1.4	0.6	0.6	1.0
	CRP-H1-90	0.5	1.0	0.3	0.1	0.2	0.3	0.3	0.4
	CRP-H2-90	0.2	1.9	0.3	0.1	0.2	0.3	0.1	0.4
	CRP-H1-70	0.3	0.8	0.4	0.2	0.2	0.3	0.2	0.4
	CRP-H2-70	0.6	0.9	0.5	0.5	0.5	0.3	0.4	0.5
	CRP-H1-45	0.6	1.9	1.8	0.8	0.9	0.6	0.4	1.0
	CRP-H2-45	1.3	1.3	0.6	0.4	0.2	0.2	0.1	0.6
	CRP-H1-20	2.2	1.3	2.2	0.2	0.5	0.7	0.2	1.0
	CRP-H2-20	1.0	1.4	1.2	0.6	1.2	0.7	0.5	0.9
	CRP-F	0.6	1.9	0.3	0.2	0.3	0.8	0.2	0.6

For the second extracted parameter (depth), depth values derived from most of the CRP methods were close to the measured depths, indicating that most of the CRP methods were able to provide good depth values. For the TSS method, the depth values had errors larger than those derived from most of the CRP methods. Except

for those of the AMF #2 (VSC), the errors of estimated depth derived from TSS mostly were > 10% whereas those derived from CRP-H2-90, which was the best among all methods, were < 7%. For the handheld CRP methods, there was a difference in error between two height settings. For the errors with the shooting angle of 90° and 70°, errors of H1 methods were less than those of H2 whereas for the errors with shooting angle of 45° and 20°, errors showed an opposite trend. Moreover, a trend of decreasing accuracy with the decrease of shooting angle can be observed, the accuracy between the CRP-H-90 and CRP-H-70 methods were at a similar level. Furthermore, the accuracy of CRP-F was at an approximately similar level as those derived from CRP-H1-90.

The AMF #2 (VSC) basically carried the largest error among all AMFs, which had errors greater than 15%. For the VSC, there was a consistent trend of underestimation of depth for all remote sensing technologies. For the rest of the AMFs, there was a trend of overestimation of depth for CRP methods whereas for the TSS method, there was a trend of underestimation of depth.

The SD values of the TSS were second largest (averaged ~0.6 cm) among all methods. With respect to the handheld CRP methods, there was not much difference in SD values between H1 and H2 except that with shooting angle of 45°, and a trend of increasing SD values with the decrease of shooting angle can be observed. Most SD values of estimated depth with shooting angles of 90° and 70° were < 0.3 cm, which provided the least values among all methods, whereas half of those with

shooting angles of 45° and 20° were > 0.5 cm. The SD values of CRP-F had similar values as those of CRP-H2-70.

It appeared that trends for RMSE values among all methods were similar to those for SD values. The TSS was most inaccurate (averaged ~1.0 cm) among all methods, which was at a similar level as the handheld CRP methods with shooting angles of 45° and 20°, whereas the CRP-H1-90 was the most accurate method with the least RMSE (~0.4 cm). Moreover, the RMSE values of the CRP-F were at a similar level as those of the CRP-H2-70, the RMSE value of each AMF mostly was < 0.6 cm. Overall, the RMSE results indicated that the CRP-H1-90 was most accurate on detecting depth among all methods.

2.3.1.4 Area of the AMFs

Table 2.6. Average area (cm^2), SD (cm^2) and RMSE (cm^2) of each morphological feature derived from manual measurement & different remote sensing methods for the indoor test.

	Methods	#1 Wide Square Ridge	#2 V-shape Channel	#3 Wide Square Channel	#4 Medium Square Ridge	#5 High Square Ridge	#6 Narrow Square Channel	#7 Medium Square Ridge	Average
Average	Measured area (cm^2)	67.3	24.1	37.7	32.7	65.4	18.0	33.9	
	TSS	50.1	23.7	37.0	31.5	64.3	21.3	35.4	
	CRP-H1-90	75.9	27.2	40.4	34.7	69.1	15.8	35.2	
	CRP-H2-90	69.9	20.3	34.8	33.7	68.9	13.8	37.8	
	CRP-H1-70	75.2	27.0	36.1	36.3	70.5	14.8	37.6	
	CRP-H2-70	77.8	27.1	36.1	40.8	72.4	13.3	41.3	
	CRP-H1-45	75.7	21.4	30.7	34.6	69.1	15.0	42.1	
	CRP-H2-45	85.3	22.8	37.2	39.3	75.6	13.4	40.1	
	CRP-H1-20	90.9	22.5	45.0	36.5	90.6	13.5	44.6	
	CRP-H2-20	65.4	16.0	43.8	38.7	78.7	14.7	42.0	
	CRP-F	73.9	20.6	33.2	36.7	70.1	13.0	34.0	
SD	TSS	13.0	8.7	6.9	5.3	7.8	2.0	2.8	6.6
	CRP-H1-90	4.6	2.4	2.0	2.2	5.9	2.0	4.3	3.3
	CRP-H2-90	3.4	3.2	2.4	2.0	4.7	0.4	2.9	2.7
	CRP-H1-70	5.6	1.1	0.8	1.0	8.0	1.7	2.3	3.0
	CRP-H2-70	6.2	4.4	6.5	2.6	5.7	1.7	3.9	4.4
	CRP-H1-45	8.4	4.8	8.5	15.3	12.4	3.0	4.3	8.1
	CRP-H2-45	27.8	2.4	3.0	3.6	9.9	2.0	3.8	7.5
	CRP-H1-20	40.9	7.5	16.0	3.0	14.9	2.4	2.1	12.4
	CRP-H2-20	15.8	8.1	5.0	4.0	7.3	4.1	7.3	7.4
	CRP-F	6.1	3.5	1.7	2.1	9.2	2.0	5.3	4.3
RMSE	TSS	21.2	8.0	6.2	5.1	7.5	3.7	3.0	7.8
	CRP-H1-90	9.7	3.8	3.2	2.9	6.7	2.9	4.3	4.8
	CRP-H2-90	4.1	4.8	3.7	2.1	5.7	4.2	4.7	4.2
	CRP-H1-70	9.5	3.1	1.8	3.7	9.1	3.6	4.3	5.0
	CRP-H2-70	12.0	5.0	6.0	8.5	8.9	4.9	8.2	7.7
	CRP-H1-45	11.5	5.2	10.4	14.7	12.3	4.1	9.2	9.6
	CRP-H2-45	32.0	2.5	2.7	7.5	13.8	5.0	7.2	10.1
	CRP-H1-20	45.4	7.0	16.1	4.8	28.9	5.0	10.9	16.9
	CRP-H2-20	15.1	10.9	7.6	7.1	15.0	5.0	10.7	10.2
	CRP-F	8.8	4.8	4.8	4.5	9.9	5.3	5.0	6.1

The area values derived from both the TSS and CRP methods were close to the measured values except for the AMF #1 (WSR), indicating that all methods were able to provide good area values for most AMFs. Except for the AMF #1 (WSR), #6 (NSC) and #7 (MSR), the accuracy of the TSS was the best among all remote

sensing methods, the errors of those AMFs were < 5% whereas for the handheld CRP methods, most of the estimated area had errors > 10%. For the handheld CRP methods, there was a difference in accuracy between H1 and H2. For the methods with shooting angle of 90º and 20º, the errors of H2 was basically less than those of H1 whereas for the methods with shooting angle of 70º and 45º, the trend was opposite. Moreover, a trend of increasing error with the decrease of shooting angle can be observed. The errors with shooting angle of 90º and 70º were mostly < 12% whereas those with shooting angle of 45 and 20º were mostly > 16%. Furthermore, the accuracy of CRP-F method was similar to that of CRP-H1-90, which had the second best accuracy among all methods.

For CRP methods, the errors of VSC and NSC mostly were > 12% and 18% respectively. There was a consistent trend of underestimation of channel area and overestimation of ridge area except for a few cases. Such trend was not observed for the TSS in most AMFs. The similar trends of area values were also observed in the of width values, probably because the AMFs derived from the CRP methods were also influenced by the strong shadow effects.

Most SD values of the TSS was > 5 cm^2, which were at an approximately similar level as those of the CRP-H2-20, which had the second largest SD values among all remote sensing methods. For the handheld CRP methods, trends for SD values were similar to those for average area values except for the CRP-H-45. Moreover, the SD

values of CRP-F were at a similar level as CRP-H2-70, this trend was similar to those of the width and depth values as described earlier.

For the WSR, the RMSE values of most remote sensing methods were the largest among all AMFs. Except those of WSR, the RMSE of the TSS were at a similar level as those of the CRP-F and CRP-H1-70 methods. For the handheld CRP methods, similar trends of the average area and SD values were able to be observed in the RMSE values as well. Moreover, the best accuracy (lowest RMSE) among all methods was obtained using the CRP-H-90.

The zonal analysis below is another way to detect the elevation difference spatially.

2.3.1.5 Zonal analysis

Table 2.7. Measured elevation differences (cm) and elevation differences (cm) derived from DEM using different methods by zone for the indoor test.

Row Column	**Top Left**	**Top Middle**	**Top Right**	**Middle Left**	**Middle Middle**	**Middle Right**	**Bottom Left**	**Bottom Middle**	**Bottom Right**	**RMS**
Measured difference (cm)	3.6	7.6	3.9	3.6	7.6	3.9	3.6	7.6	3.9	
TSS	3.0	6.3	3.5	3.5	6.7	3.7	3.5	6.5	3.5	0.7
CRP-H1-90	3.1	7.3	3.8	3.6	7.4	3.8	3.3	7.4	4.0	0.2
CRP-H2-90	3.4	7.9	3.8	3.6	7.7	3.8	3.4	7.3	4.0	0.2
CRP-H1-70	3.1	6.8	4.4	3.1	7.7	4.2	3.7	8.0	3.9	0.4
CRP-H2-70	3.2	7.4	4.9	3.2	7.8	4.6	3.1	7.8	4.6	0.5
CRP-H1-45	0.2	1.4	3.4	0.2	4.7	3.7	5.0	6.4	4.1	2.9
CRP-H2-45	2.7	7.4	4.5	3.1	7.3	4.7	3.5	8.0	4.9	0.6
CRP-H1-20	3.9	2.3	4.3	0.7	5.3	4.0	3.7	8.4	2.7	2.5
CRP-H2-20	0.1	6.1	2.0	2.4	7.7	3.4	4.7	9.0	2.2	1.7
CRP-F	3.0	6.3	3.7	3.2	7.2	3.6	3.6	7.2	3.9	0.5

The RMS values of zonal analysis provided a similar result as depth analysis for different methods except for the CRP-H1-45 and CRP-H1-20, which provided the two largest RMS values

For the TSS method, most elevation differences had error larger than 10% whereas for the handheld CRP methods, expect for those with shooting angles of 20º and 45º, most elevation differences had an error less than 5%. There was a dramatic increase of error when the shooting angles dropped to 45º and 20º; the most errors were larger than 30%. The accuracy of CRP-F was at an approximately level as CRP-H-70, probably because shooting angles of these two methods were similar.

The errors of elevation difference varied with different positions. For the TSS method, the elevation difference at the middle column had the largest error comparing to the others, it occupied around 65% of total error. Besides, the differences at the top row had larger errors than other rows, probably because the top row was the furthest area from the total station scanner. For the CRP methods, most errors of the left column were the largest among all columns. Trends of middle row with the least error values can be found in the most CRP methods with shooting angles of 90° and 70°, probably because the photos were taken at the top and bottom positions. Whereas there was no a clear trend of error can be observed in the CRP methods with shooting angles of 45° and 20°, which error was randomly distributed over the board surface.

Overall, the ability of CRP-H-90 method on detecting AMFs was the best among all, and most CRP methods were able to detect the AMFs correctly. Whereas the ability of the TSS method for detecting the depth of AMFs was much worse than the most CRP methods, indicating that the elevation difference is hard to be detected

accurately using the TSS method. Unlike the shapes of AMFs derived from the CRP methods, those derived from the TSS were not able to be showed correctly. With respect to the handheld CRP methods, the ability on capturing AMFs and measuring elevation difference became worse while shooting angle drops. Moreover, there was a clear difference between different height settings of CRP methods with shooting angles of 45° and 20°, the DEM derived from the H2 was more accurate than that derived from the H1, indicating that higher elevation provided a better accuracy with the low shooting angles. Compared with the handheld CRP methods, the CRP-F method was at an approximately same level as the CRP-H-70 methods. It usually had a worse performance than those with shooting angle of 90°. Oppositely, the performance of CRP-F was better than those with a shooting angle of 45° and 20°.

Furthermore, the applicability of these two remote sensing technologies was assessed as well. The equipment, number of operators, time consumption, and detecting range varied with different methods. Which method is more practicable for experiments at the larger scale? The table below may provide some useful information.

2.3.1.6 Applicability analysis

Table 2.8. Consumptions (operator, time) and detecting range (m) of different methods for the indoor test.

Method	Equipment	# of Operator	Data Collection Time (min.)	Data Processing Time (min.)	Detection Range Limit (m)
TSS	a total station scanner	1	~200	~20	~150.0
CRP-H1-90	a camera	1	~10	~40	~2.0
CRP-H2-90	a camera, a meter stand	1	~15	~40	~2.5
CRP-H1-70	a camera	1	~10	~40	~3.0
CRP-H2-70	a camera, a meter stand	1	~15	~40	~4.0
CRP-H1-45	a camera	1	~10	~40	~4.5
CRP-H2-45	a camera, a meter stand	1	~15	~40	~5.0
CRP-H1-20	a camera	1	~10	~40	~10.0
CRP-H2-20	a camera, a meter stand	1	~15	~40	~15.0
CRP-F	a platform, two cameras, two laptops	2	~20	~40	~7.0

Conducting CRP-F method required multiple equipment and at least 2 people. Compared with the CRP-F, all other methods needed less equipment and operator. However, the price for total station scanner was the most expensive (~$20,000) among all methods.

With respect to the time consumption with different methods, TSS method usually took ~10 to 20 times longer as the CRP methods to collect morphological data whereas for the time of raw data processing, TSS method just took half time as CRP method. Overall, TSS was still the most time-consuming method comparing to other CRP methods. However, the TSS method just required ~20 mins to setup the station then the operator can leave the station alone, whereas the CRP methods required the operator to stay during all the data collection period.

Settings of remote sensing methods changed the detection range. The detection range of the TSS can reach ~150 m, which was able to detect the largest area among all

methods due to free rotation scanner. The detection range of the CRP methods was much less than that of the TSS. For the handheld CRP methods, there were clear trends of a rising elevation and a decreasing shooting angle with the greater detection range. Moreover, the detection range of the CRP-F method can reach ~7 m based on the design of the platform.

Although the TSS method was able to produce some reasonably accurate DEMs, it was still the most time-consuming one among all remote sensing technologies. For both CRP-H-90 and CRP-H-70 methods, they were able to detect AMFs accurately while they had the largest limits of detection range, indicating that these methods were not able to capture large areas but can detect channels or small gullies correctly. Oppositely, the detection range of the CRP-H-20 was the largest among CRP methods, but the values of morphological parameters derived from this method were less reliable. Moreover, the software (PhotoModeler Scanner®, 2014) usually experiences a hard time to process the photos with shooting angles 20º. Furthermore, the CRP-F method was a good option for detecting AMFs at plot/field scale with relatively high accuracy.

2.3.2 Outdoor field test

2.3.2.1 Visual observations

The photos which were taken by the handheld CRP methods were not able to be processed by the software (PhotoModeler Scanner®, 2014), probably because the longitudinal overlaps of photos taken with shooting angles of 90º, 70º and 45º were

too few and the numbers of photos were not enough. For photos taken with shooting angle of 20º, the software experienced a hard time and failed to process these photos. Figure 2.8 illustrated example transect derived from DEM with different remote sensing methods.

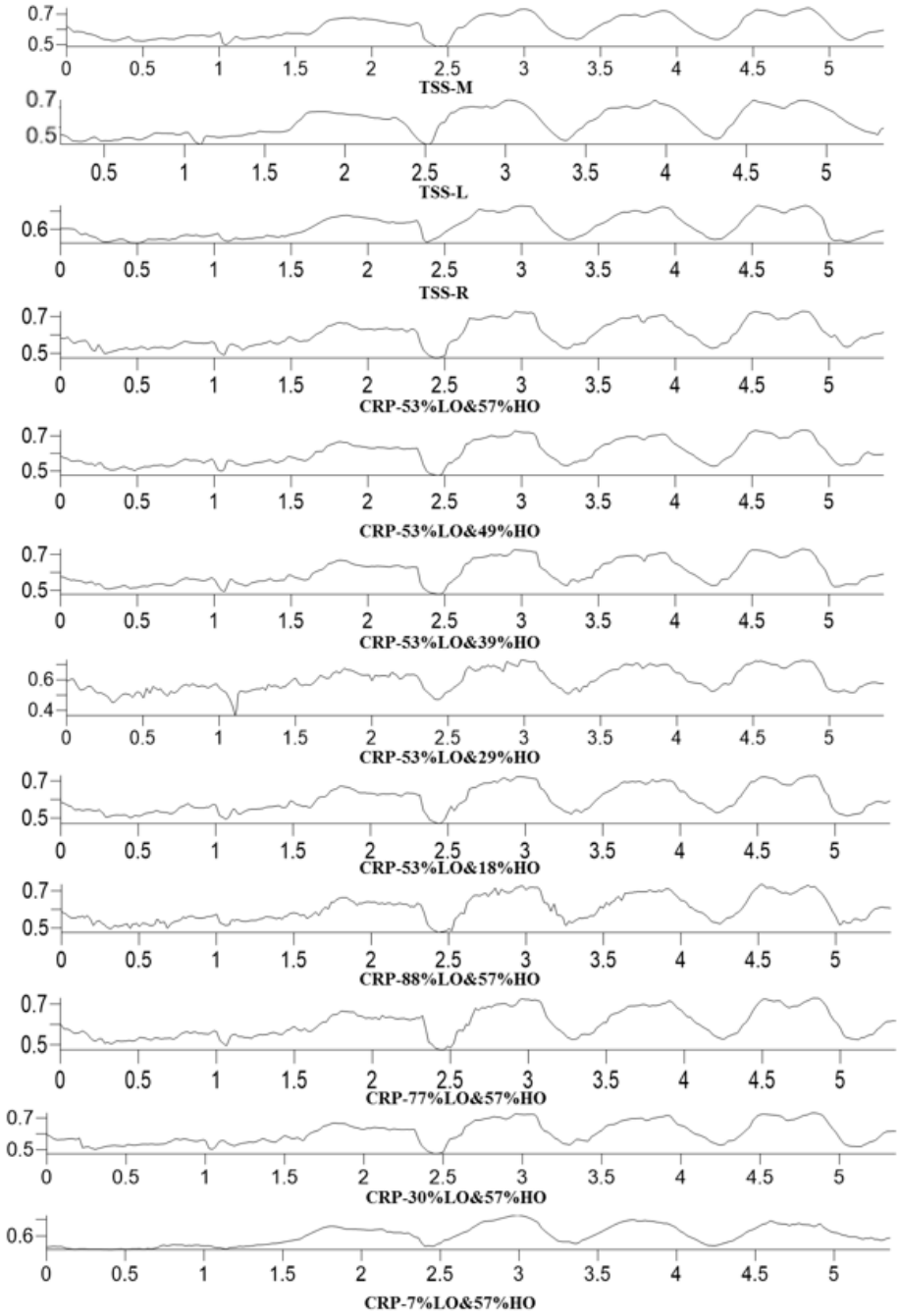

Figure 2.8. A transect extracted from each DEM generated using different remote sensing methods for the outdoor test.

Both TSS and CRP methods were able to identify the location of each AMF correctly. It appeared that transect derived from the TSS was smoother than those derived from the CRP methods. For the CRP methods, there was a clear trend of rougher surface with the increasing horizontal and longitudinal overlaps. This trend was probably a reflection of the number of its raw data points, which increased with the large overlaps.

For the TSS methods, the channels extracted from the TSS-M had symmetric sloping sides whereas for those extracted from the TSS-L and TSS-R methods, the right and left sides of channels were poorly defined respectively. This may be a reflection of the principle behind the TSS. Areas at the corner of channel banks were not able to be captured by the scanner which was located at the sides of the plot. However, the sides of each channel were able to be captured using almost all CRP methods expect for the CRP-7%LO&57%HO.

For the different horizontal overlaps, the estimated depth of the AMF #1 (NC) derived from CRP-53%LO&29%HO method was much deeper than that derived from the other CRP methods. Moreover, all AMFs were able to be captured using the CRP methods with different longitudinal overlaps until the overlap rate dropped to 7%.

2.3.2.2 Width of AMFs

Measured and DEM-extracted values for the two parameters (width, depth) of the four AMFs were summarized in Table 2.9 and table 2.10, respectively.

Table 2.9. Average width (cm), SD (cm) and RMSE (cm) of each morphological feature derived from manual measurement & different remote sensing methods for the outdoor test.

	Methods	#1 Narrow Channel	#2 Wide Channel	#3 Channel Between Potato HIlls	#4 Channel Between Potato Hills	Average
Average	Measured width (cm)	10.0	20.0	91.0	91.0	
	TSS-M	12.6	23.9	93.6	92.8	
	TSS-L	13.8	26.1	94.1	94.3	
	TSS-R	10.8	25.6	94.2	92.7	
	CRP-53%LO&57%HO	10.3	23.1	91.7	91.9	
	CRP-53%LO&49%HO	9.9	22.3	92.2	93.1	
	CRP-53%LO&39%HO	10.5	21.7	93.2	93.9	
	CRP-53%LO&29%HO	11.9	23.8	92.6	92.2	
	CRP-53%LO&18%HO	12.1	21.7	93.6	94.1	
	CRP-88%LO&57%HO	10.4	21.5	91.1	91.1	
	CRP-77%LO&57%HO	11.1	21.7	92.0	91.4	
	CRP-30%LO&57%HO	11.0	22.4	93.6	90.6	
	CRP-7%LO&57%HO	9.5	21.2	87.5	85.1	
SD	TSS-M	1.5	3.9	1.2	2.3	2.2
	TSS-L	2.1	4.6	9.3	4.1	5.0
	TSS-R	4.2	5.7	4.0	1.4	3.8
	CRP-53%LO&57%HO	0.7	3.0	0.8	0.7	1.3
	CRP-53%LO&49%HO	1.3	2.8	2.4	1.9	2.1
	CRP-53%LO&39%HO	1.0	2.5	1.9	2.9	2.1
	CRP-53%LO&29%HO	1.4	3.0	1.5	0.2	1.5
	CRP-53%LO&18%HO	1.2	3.0	1.4	1.8	1.8
	CRP-88%LO&57%HO	1.6	1.2	0.6	0.4	1.0
	CRP-77%LO&57%HO	1.3	3.6	2.1	2.9	2.5
	CRP-30%LO&57%HO	2.2	4.9	3.5	4.5	3.8
	CRP-7%LO&57%HO	2.6	11.8	11.2	10.9	9.1
RMSE	TSS-M	3.0	5.3	2.8	2.7	3.4
	TSS-L	4.3	7.4	8.8	5.0	6.4
	TSS-R	3.8	7.6	4.8	2.1	4.6
	CRP-53%LO&57%HO	0.7	4.1	0.9	1.1	1.7
	CRP-53%LO&49%HO	1.2	3.4	2.5	2.6	2.4
	CRP-53%LO&39%HO	1.1	2.8	2.8	3.9	2.6
	CRP-53%LO&29%HO	2.3	4.6	2.1	1.2	2.6
	CRP-53%LO&18%HO	2.4	3.1	2.9	3.5	3.0
	CRP-88%LO&57%HO	1.5	1.9	0.5	0.4	1.1
	CRP-77%LO&57%HO	1.6	3.6	2.2	2.6	2.5
	CRP-30%LO&57%HO	2.2	5.1	4.0	4.0	3.8
	CRP-7%LO&57%HO	2.4	10.6	10.6	11.4	8.7

CRP methods were able to provide some good width values of AMFs, which were close to the manual measurements whereas TSS methods provided width values much differed from the “true” values. It appeared that the TSS-M was able to obtain the best estimation of width among all TSS methods followed by the TSS-R, and the accuracy of the TSS-M was at a similar level as those derived from CRP-53%LO&18%HO. With respect to the CRP methods with different overlap rates, there was a trend of increasing errors with the decreasing overlap (horizontal and longitudinal). For the AMF #1 (NC) and #2 (WC), the CRP methods with 29% and 18% horizontal overlaps had errors mostly greater than 18% whereas the CRP methods with the rest horizontal overlaps just had errors mostly less than 10%. The accuracy of CRP-88%LO&57%HO was the best among all technologies, probably because CRP with 88% overlap rates was able to provide the rawest data points of the field.

For the AMF #1 (NC) and #2 (WC), the estimated width values derived from TSS had errors mostly > 20% whereas the CRP methods had errors mostly < 12%. Besides, for those for the AMF #3 (CBH1) and #4 (CBH2), errors of both remote sensing methods were mostly < 4%, probably because of the size of the channel. Moreover, for all remote sensing settings, there was a consistent trend of overestimation of the AMF (channel in this case) width except for a few cases. This unexpected result was different to the trend of the board test, may because the channels in the field test were not exact square in shape.

Except for those for the CBH2, the SD values of the TSS-M method, which were mostly < 3 cm, were superior to those of the TSS methods at side positions. Compared with the CRP methods, which had SD values mostly < 2cm, the SD values of the TSS methods were mostly > 4 cm. Moreover, there was a trend of a rising SD value with the falling overlap rates except for few cases.

Trends for the RMSE values among all methods were similar to those for the SD values. The RMSE values of the TSS-M were the best among all TSS settings, which were at the approximately same level as those of the CRP-30%LO&57%HO method. Overall, the RMSE values indicated that the absolute accuracy of the CRP-88%LO&57%HO was the best among all technologies.

2.3.2.3 Depth of AMFs

Table 2.10. Average depth (cm), SD (cm) and RMSE (cm) of each morphological feature derived from manual measurement and different remote sensing methods for the outdoor test.

	Methods	#1 Narrow Channel	#2 Wide Channel	#3 Channel Between Potato HIlls	#4 Channel Between Potato Hills	Average
Average	Measured depth (cm)	10.0	15.0	19.0	19.4	
	TSS-M	6.5	13.8	18.1	18.0	
	TSS-L	5.2	13.9	17.1	16.8	
	TSS-R	2.5	12.3	18.2	17.7	
	CRP-53%LO&57%HO	8.2	13.4	19.4	18.1	
	CRP-53%LO&49%HO	8.3	12.8	18.8	18.4	
	CRP-53%LO&39%HO	8.1	13.3	18.2	18.0	
	CRP-53%LO&29%HO	7.9	13.2	18.8	17.5	
	CRP-53%LO&18%HO	6.5	12.0	19.7	18.7	
	CRP-88%LO&57%HO	7.8	14.8	19.0	19.4	
	CRP-77%LO&57%HO	7.6	13.3	19.3	18.2	
	CRP-30%LO&57%HO	8.2	13.6	18.9	16.9	
	CRP-7%LO&57%HO	5.4	7.9	15.9	12.4	
SD	TSS-M	1.6	0.6	1.5	2.0	1.4
	TSS-L	1.2	1.7	1.7	3.4	2.0
	TSS-R	1.4	2.0	1.4	1.9	1.7
	CRP-53%LO&57%HO	1.4	2.4	1.4	2.1	1.8
	CRP-53%LO&49%HO	1.5	3.0	1.1	2.3	2.0
	CRP-53%LO&39%HO	1.5	1.9	0.6	2.9	1.7
	CRP-53%LO&29%HO	0.4	1.5	1.2	2.3	1.4
	CRP-53%LO&18%HO	2.3	2.2	1.8	2.1	2.1
	CRP-88%LO&57%HO	1.4	1.6	2.0	0.8	1.4
	CRP-77%LO&57%HO	2.1	3.1	0.9	2.3	2.1
	CRP-30%LO&57%HO	2.7	2.9	1.4	5.8	3.2
	CRP-7%LO&57%HO	4.6	4.9	6.8	8.5	6.2
RMSE	TSS-M	3.8	1.3	1.6	2.3	2.2
	TSS-L	4.9	1.9	2.4	4.0	3.3
	TSS-R	7.6	3.3	1.5	2.4	3.7
	CRP-53%LO&57%HO	2.2	2.7	1.3	2.2	2.1
	CRP-53%LO&49%HO	2.2	3.5	1.0	2.3	2.2
	CRP-53%LO&39%HO	2.3	2.4	1.0	2.9	2.1
	CRP-53%LO&29%HO	2.2	2.2	1.1	2.8	2.1
	CRP-53%LO&18%HO	4.1	3.6	1.7	2.0	2.9
	CRP-88%LO&57%HO	2.5	1.4	1.8	0.7	1.6
	CRP-77%LO&57%HO	3.0	3.2	0.8	2.4	2.4
	CRP-30%LO&57%HO	3.0	3.0	1.2	5.8	3.3
	CRP-7%LO&57%HO	6.2	8.3	6.8	10.3	7.9

For the second parameter (depth), the TSS methods had errors mostly larger than the CRP methods, indicating that the estimated depth values derived from the CRP methods were closer to the manual measurements than those of the TSS. For the TSS methods, the TSS-M provided the best estimation of depth, which was at a similar level as the CRP-53%LO&18% method. Besides, all TSS methods had errors mostly > 10%. For the CRP methods with different overlap rates (horizontal and longitudinal), there was a trend of increasing errors with the decreasing overlap rates. Moreover, the CRP-88%LO&57%HO method estimated the best depth values among all methods.

Trends for the average depth values of different AMFs were similar to the average width values. The NC and WC had larger errors than CBH1 and CBH2 for the most cases. The errors of the NC and WC were mostly larger than 12% whereas those of the CBH1 and CBH2 were mostly less than 7%. There was a consistent trend of underestimation of channel depth for each setting except for few cases. A similar trend of the V-shape channel depth was observed in the board test.

The SD values of the TSS methods were at an approximately same level as the CRP methods. For the TSS methods, the middle position setting still had the best performance compared to the other two settings whereas for the CRP methods, the CRP-88%LO&57%HO method provided the best depth estimation. There was not much difference in the SD value among the CRP methods with different overlap rates. However, for the CRP methods with different longitudinal overlaps, the

method with 7% overlap had the largest SD values (averaged ~6.2 cm) among all settings.

Trends for the RMSE values among all were similar to those for the SD values. The worst absolute accuracy was obtained using the CRP-7%LO&57%HO method whereas the best RMSE values were derived from the CRP-88%LO&57%HO method.

2.3.2.4 Zonal analysis

The ability of the CRP-88%LO&57%HO method on detecting AMFs and measuring elevation difference was the best among all remote sensing methods. For the zonal analysis, the CRP-88%LO&57%HO was used as the reference to compare to DEMs with different remote sensing settings. The graphs below showed the comparisons of different methods. The red color illustrated that elevation of the DEM is higher than that of the reference; oppositely, the blue color indicated that elevation of the DEM is lower than that of the reference.

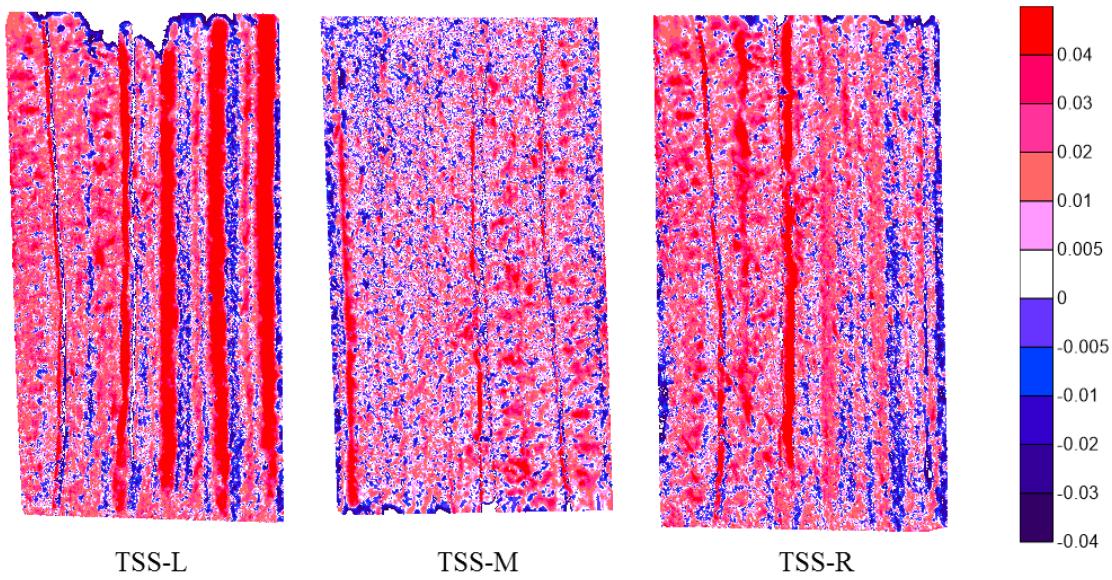

Figure 2.9. Spatial distribution of elevation differences (m) using TSS methods for the outdoor test (red color represents elevation increase to the reference; blue color represents elevation decrease to the reference).

In Fig. 2.9, the TSS-L method showed that the dark red areas were basically located at the right part of the plot, especially on the right sides of potato hills. On the other hand, the TSS-R method illustrated a different pattern; the dark red areas were oppositely located at the left part of the plot. This is a reflection of the principle of the TSS method. The TSS which located at side position might not be able to capture the sides or the bottom of a channel due to the shadow effects. For the TSS-M, the comparison showed that the red and blue colors were distributed evenly over the plot, indicating the TSS-M method was able to provide the closest DEM to the reference among all TSS methods. The same result also can be observed in the analysis for the morphological parameters (width, depth).

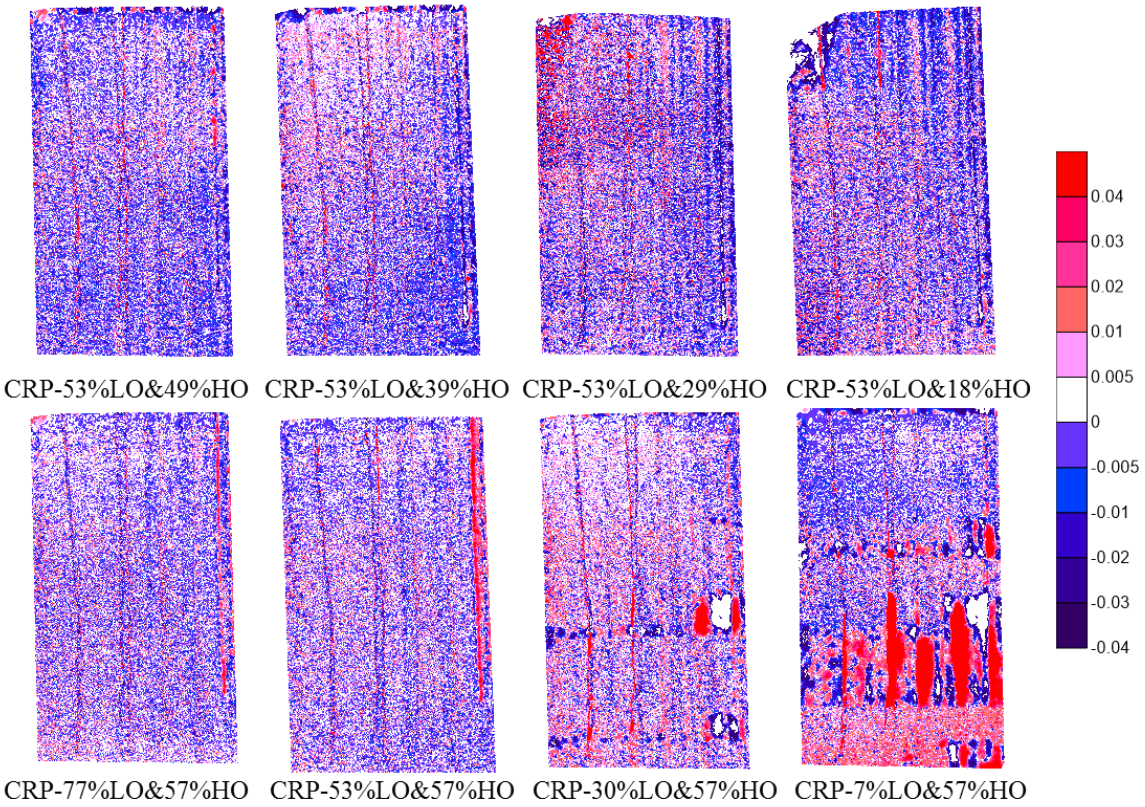

Figure 2.10. Spatial distribution of elevation differences using CRP methods for the outdoor test (red color represents elevation increase to the reference; blue color represents elevation decrease to the reference).

Compared with the TSS methods, in Fig. 2.10, the light blue color of the CRP methods occupied most areas of the plot, indicating that the elevations extracted from the CRP methods were slightly lower than the reference. For all CRP methods, there was a consistent trend that the elevations extracted from the sloping sides of the channel were higher than those of the reference.

For the CRP methods with different horizontal overlap rates, there was not much difference visually whereas for the CRP methods with different longitudinal overlap rates, an obvious change can be observed while the longitudinal overlap dropped to

30%. The CRP method with 7% longitudinal overlap showed a larger error over the whole plot, probably because the overlap was too few to generate a quality DEM.

2.3.2.5 Applicability analysis

The applicability of these two remote sensing technologies was assessed as well. The table 2.11 indicated characteristics of each remote sensing setting.

Table 2.11. Consumptions (operator, time) and detecting range (m) of different methods for the outdoor test.

Method	Equipment	# of Operator	Data Collection Time (min.)	Data Processing Time (min.)	Detection Range Limit (m)
TSS-M	a total station scanner	1	~420	~20	~150.0
TSS-L	a total station scanner	1	~420	~20	~150.0
TSS-R	a total station scanner	1	~420	~20	~150.0
CRP-53%LO&57%HO	a platform, two cameras, two laptops	2	~20	~40	~7.0
CRP-53%LO&49%HO	a platform, two cameras, two laptops	2	~20	~40	~7.4
CRP-53%LO&39%HO	a platform, two cameras, two laptops	2	~20	~40	~7.9
CRP-53%LO&29%HO	a platform, two cameras, two laptops	2	~20	~40	~8.4
CRP-53%LO&18%HO	a platform, two cameras, two laptops	2	~20	~40	~8.9
CRP-88%LO&57%HO	a platform, two cameras, two laptops	2	~30	~50	~7.0
CRP-77%LO&57%HO	a platform, two cameras, two laptops	2	~25	~40	~7.0
CRP-30%LO&57%HO	a platform, two cameras, two laptops	2	~15	~30	~7.0
CRP-7%LO&57%HO	a platform, two cameras, two laptops	2	~10	~20	~7.0

The time consumptions of the TSS methods experienced a dramatic increase for detecting a relatively large plot. The TSS method required ~7 hours to scan a 60 m^2 plot at 1.5 cm horizontal and vertical intervals. One time battery switch for the total station was necessary during the field scanning. For the rest of the time, the total station was able to work alone without an operator. The CRP methods required two operators and less time to conduct the field detection.

For the TSS methods, the detection range was ~150 m on conducting field scan whereas for the CRP methods, there was a clear trend of the increasing detection range with the drop of horizontal overlap rate. However, the detection range of the

CRP methods with different longitudinal overlap rates was at the same level, because they had same horizontal overlap.

Overall, the ability of the TSS-M method on detecting AMFs and measuring elevation difference was at a similar level as that CRP method with 53%LoO&18%HO, which would be able to produce some reasonably accurate DEMs. The TSS-M was still the most consuming method among all settings. For the CRP methods with different overlap rates, most of them were able to detect AMFs accurately expect for the CRP-30%LO&57%HO and the CRP-7%LO&57%HO. The accuracy of the CRP-88%LO&57%HO method on detecting AMFs was the best followed by the CRP-53%LO&57%HO and the CRP-77%LO&57%HO. In comparison among these methods, the detection range of all three methods was at the same level but the time consumption of them was different. For the CRP-88%LO&57%HO method, the time consumption was the longest whereas for the CRP-53%LO&57%HO method, that was the shortest among these three methods.

2.4 Conclusion

In this study, the CRP method with large shooting angle (90º and 70º) performed better than the TSS methods for both the indoor and outdoor tests. For the indoor tests, the handheld CRP method with large shooting angle detected AMFs and elevation differences accurately. The results showed that the RMSE derived for the AMF areas, widths and depths were 4.2 cm^2, 0.8 cm, and 0.4 cm, respectively, i.e.,

smaller than those derived from smaller shooting angle settings. In comparison, the CRP-F performance was similar to the handheld CRP performance with a 70º shooting angle. Both handheld CRP and CRP-F performed better than the TSS method. For the outdoor tests, it is clear that the TSS method, when centered on the middle position, provided the most accurate results among TSS methods. In addition, the CRP-F performances improved with increasing overlap rates.

For practical purposes, the TSS method required the least amount of the equipment and operational effort, and the detection range is less limiting as well. However, using TSS takes more time to cover large areas than using the CRP methods. For accurate measurement of small sized channels and gullies, the handheld CRP method with large shooting angle is best. For a larger area, the CRP-F method with 53% longitudinal overlap & 57% horizontal overlap is the best to determine changes in morphological features and measure elevation differences.

Reference

Abd Elbasit, M.A., Anyoji, H., Yasuda, H., Yamamoto, S., 2009. Potential of low cost close-range photogrammetry system in soil microtopography quantification. Hydrological Processes. 23(10): 1408-1417.

Aguilar, F.J., Mills, J., 2008. Accuracy assessment of lidar-derived digital elevation models. The Photogrammetric Record. 23(122): 148-169.

Aguilar, M.A., Aguilar, F.J., Negreiros, J., 2009. Off-the-shelf laser scanning and close-range digital photogrammetry for measuring agricultural soils microrelief. Biosystems engineering. 103(4): 504-517.

Ali, M. E. N. O., Eliwa, M. A., Mohanmed, A. A. E., Abbas, E. A. M., 2000. Accuracy analysis for new close-range photogrammetric systems. International Archives of Photogrammetry and Remote Sensing. 33: Part B5.

Berger, C., Schulze, M., Rieke-Zapp, D., Schlunegger, F., 2010. Rill development and soil erosion: a laboratory study of slope and rainfall intensity. Earth Surface Processes and Landforms. 35(12): 1456-1467.

Bewket, W., Sterk, G., 2003. Assessment of soil erosion in cultivated fields using a survey methodology for rills in the Chemoga watershed, Ethiopia.Agriculture, ecosystems & environment. 97(1): 81-93.

Blaes, X., Defourny, P., 2008. Characterizing bidimensional roughness of agricultural soil surfaces for SAR modeling. IEEE Transactions on Geoscience and Remote Sensing. 46(12): 4050–4061.

Boehler, W., Vicent, M.B., Marbs, A., 2003. Investigating laser scanner accuracy. The International Archives of Photogrammetry, Remote Sensing and Spatial Information Sciences. 34(Part 5): 696-701.

Butler, J.B., Lane, S.N., Chandler, J.H., 1998. Assessment of DEM quality for characterizing surface roughness using close range digital photogrammetry. The Photogrammetric Record. 16(92): 271-291.

Couper, P., Stott, T., Maddock, A., 2002. Insights into river bank erosion processes derived from analysis of negative erosion-pin recordings: Observations from three recent UK studies. Earth Surf. Process. Landf. 27: 59–79.

Gessesse, G.D., Fuchs, H., Mansberger, R., Klik, A., Rieke-Zapp, D.H., 2010. Assessment of erosion, deposition and rill development on irregular soil surfaces using close range digital photogrammetry. The Photogrammetric Record. 25(131): 299-318.

Ghimire, S.K., Higaki, D., Bhattarai, T.P., 2013. Estimation of soil erosion rates and eroded sediment in a degraded catchment of the Siwalik Hills, Nepal. Land. 2(3): 370-391.

Herweg, K., 1996. Field manual for assessment of current erosion damage. SCRP, Ethiopia and Centre for Environment and Development, University of Berne, Switzerland.

Lawler, D.M., Couperthwaite, J., Bull, L., Harris, N.M., 1997. Bank erosion events and processes in the Upper Severn Basin. Hydrol. Earth Surf. Sci. 1: 523–534.

Lowe, D.G., 2004. Distinctive image features from scale-invariant keypoints. International Journal of Computer Vision. 60: 91-110.

Milan, D.J., Heritage, G.L., Hetherington, D., 2007. Application of a 3D laser scanner in the assessment of erosion and deposition volumes and channel change in a proglacial river. Earth surface processes and landforms. 32(11): 1657-1674.

Miri, M., Varshosaz, M., 2011. Evaluating parameters affecting the georeferencing accuracy of terrestrial laser scanners. International Archives of the Photogrammetry, Remote Sensing and Spatial Information Sciences. 38: 5/W16.

Montane, J.M., Torres, R., 2006. Accuracy assessment of LIDAR saltmarsh topographic data using RTK GPS. Photogrammetric Engineering & Remote Sensing. 72(8): 961-967.

Nadal-Romero, E., Revuelto, J., Errea, P., López-Moreno, J.I., 2015. The application of terrestrial laser scanner and SfM photogrammetry in measuring erosion and deposition processes in two opposite slopes in a humid badlands area (central Spanish Pyrenees). SOIL. 1(2): 561-573.

Nasermoaddeli, M.H., Pasche, E., 2008. Application of terrestrial 3D laser scanner in quantification of the riverbank erosion and deposition. Proceedings of Riverflow. 3-5 p.

Peter Heng, B.C., Chandler, J.H., Armstrong, A., 2010. Applying close range digital photogrammetry in soil erosion studies. The Photogrammetric Record. 25(131): 240-265.

Rieke-Zapp, D., Wegmann, H., Santel, F., Nearing, M.A., 2001, April. Digital photogrammetry for measuring soil surface roughness. In Proceedings of the year 2001 annual conference of the American Society for Photogrammetry & Remote Sensing ASPRS. 23-27 p.

Salleh, M.R.M., Ismail, Z., Rahman, M.Z.A., 2015. Accuracy Assessment of Lidar-Derived Digital Terrain Model (dtm) with Different Slope and Canopy Cover in Tropical Forest Region. ISPRS Annals of the Photogrammetry, Remote Sensing and Spatial Information Sciences. 2(2): 183.

Samad, A.M., Ahmad, A., Ishak, N., 2010. Assessment of digital camera for mapping stream using close range photogrammetric technique. Proc. 20106th Int. Colloq. Signal Process. Its Appl. (CSPA). 1 -5 p.

Schowengerdt, R. A., 2007. Remote Sensing: models and methods for image processing (3rd ed.). Academic Press. 2 p.

Schmid, T., Schack-Kirchner, H., Hildebrand, E., 2004. October. A case study of terrestrial laser scanning in erosion research: calculation of roughness and volume balance at a logged forest site. In Proceedings of the ISPRS Working Group VIII/2: Laser-Scanners for Forest and Landscape Assessment. 3-6 p.

Stott, T. A., 1997. Comparison of stream bank erosion processes on forested and moorland streams in the Balquhidder catchments, Central Scotland. Earth Surf. Process. Landf. 22: 383–399.

Taconet, O., Ciarletti, V., 2007. Estimating soil roughness indices on a

ridge-and-furrow surface using stereo photogrammetry. Soil and Tillage Research. 93(1): 64–76.

Vinci, A., Brigante, R., Todisco, F., Mannocchi, F., Radicioni, F., 2015. Measuring rill erosion by laser scanning. Catena. 124: 97-108.

Zribi, M., Ciarletti, V., Taconet, O., Paille, J., Boissard, P., 2000. Characterisation of the soil structure and microwave backscattering based on numerical three-dimensional surface representation: analysis with a fractional Brownian model. Remote Sensing of Environment. 72(2): 159–169.

Chapter 3

Quantifying soil surface evolution during winter and snow melting using total station scanning and close-range photogrammetry

Abstract

Soil surface morphology is strongly affected by land management practices and soil biophysical processes such as soil erosion. Traditional methods on measuring soil surface morphology changes have been costly, time-consuming and causing extra soil disturbance. Alternatively, remote sensing technologies involving 3D scanning and photogrammetry are becoming available and capable of measuring surface morphology correctly and quickly. However, most studies just focused on small-scale rill erosion during short snow-free periods.

A field experiment was conducted at the AAFC Fredericton Research and Development Centre, New Brunswick, on 6 m by 80 m large plots to determine surface morphological changes under three tillage treatments during winter. The treatments involved (i) potato cropping with up-down-slope tillage, (ii) potato cropping with contour tillage, and (iii) fallowing with up-down-slope tillage (control). Surface morphologies (elevation, slope, curvature) were scanned and evaluated at the beginning and end of winter.

For the winter period, there was an about 2.1 cm to 2.9 cm drop in elevation for the plots as a whole, which can be translated to a net soil loss of 231 Mg ha^{-1} to 319 Mg ha^{-1}. However, this elevation change would not only be due to soil erosion, but to other soil-structure affecting changes as well, such as freeze-thaw action and biophysically affected changes in soil aggregation and pore volumes. For the two rills derived from the winter period, CRP yields higher and more accurate value than

TSS by about 11 Mg ha^{-1} and 0.9 Mg ha^{-1} respectively. In addition, there was no obvious difference of surface morphological change between tillage treatments, indicating that the effect of tillage treatment was not strong on morphological change during the winter period.

3.1 Introduction

In New Brunswick, the potato is the main cash crop. After harvest, potato fields are usually bare during winter and snowmelt seasons. In this period, soil morphology can be influenced by many soil biophysical processes such as gravitational subsidence, compactions by snow, soil freeze-thaw action, and snowmelt erosion and rainfall erosion when the ground is snow free. Gravitational subsidence occurs after harvesting or fall tillage when the loosened soil gradually subsides due to its own weight. If the ground is not frozen before the first snowfall events, a thick layer of snow building up during the winter may cause compaction of soil underneath. The freeze-thaw action occurs in a wet environment where the temperature fluctuates above and below freezing point. During the freezing period, ice is formed, so that the soil is hard to be eroded. Meanwhile, due to the expansion in volume from water to ice, soil particles are pushed apart. However, soil erosion probably has a very strong impact on soil surface morphology during snowmelt period as well. For snowmelt erosion, the main mechanism of soil particles detachment in winter is freeze-thaw action instead of rainfall splashing. When the snow starts to melt, a large amount of melting snow accumulated during the winter months can generate a large volume of flow over frozen soil with no infiltration (Li, 2012), resulting in a large amount of soil detachment and movement and channel generation in the field (Spomer and Hjelmfeldt, 1983). Auzet et al. (1993) indicated that soil loss of ephemeral channel erosion after snow melting equals ~80% of that of rill erosion. Therefore, snowmelt

erosion has a great influence on soil surface morphology, especially in Canada where a large amount of snow is often accumulated in the winter months.

Due to the strong impact of snowmelt erosion on soil surface morphology, several methods have been developed to measure soil erosion rate by detecting surface morphological change.

The traditional manual survey methodology has been used widely to measure rill or gully erosion by assessing the dimensions or density of channels in a field (Bewket and Sterk, 2003). Serval studies have employed this method to investigate rills and gullies created by snowmelt erosion (Edwards et al., 1998; Øygarden, 2003). However, this method is not able to capture inter-rill erosion. Inter-rill erosion can be measured using erosion pin. For this method, a set of erosion pins are placed into the ground and the ground level is recorded over time using those erosion pins as a reference (Ghimire et al., 2013). Evans and Warburton (2011) showed an example of using photo-resistive erosion pins (PREP) in North Pennines, UK to measure surface retreat during the winter period. However, both methods may disturb the natural conditions of the field and require considerable time and efforts to acquire data with high spatial and temporal resolutions.

Another way to measure morphological change is the remote sensing technology. Remote sensing is a technology to obtain information about an object or phenomenon without physical contact (Schowengerdt, 2007). Compared to the traditional methods described above, the remote sensing methods can often acquire

the soil morphology quicker, easier and more accurate. Many scientists have applied the aerial-based remote sensing techniques to detect morphological changes (Croke et al., 2013; Perroy et al., 2010; Welch et al., 1983; Welch et al., 1984; Ventura et al., 2011). However, aerial-based remote sensing methods have some limitations, including their high costs and low resolutions. With recent technical advances, ground-based remote sensing becomes more available to ordinary users. For example, Neugirg et al. (2014) utilized terrestrial laser scanner to monitor long-term soil erosion of a catchment and waste dump site in Germany and Italy. The result showed a good agreement between the annual erosion rate measured and the size of the hydrological catchment. Although the study detected the soil surface after snowmelt, it only focused on rill occurred on the surface. The surface morphological change during the winter was not presented. Li et al. (2014) simulated the environmental conditions after snowmelt in the laboratory and used the close-range photogrammetry method to capture morphological change on the slope due to snowmelt erosion. The result indicated that the close-range photogrammetry method can be applied to snowmelt erosion monitoring.

Most snowmelt erosion studies using remote sensing methods have focused on rill erosion and are conducted on a field under the same tillage treatment. There is a lack of study at the field scale in an operation agricultural field, where multiple processes may occur simultaneously causing surface morphological change.

In this study, both remote sensing methods (3D scanner and close-range photogrammetry) were used to monitor soil surface during the winter.

The objective is to quantify surface morphology evolution under different tillage treatments during winter and snowmelt season.

3.2 Methodology

3.2.1 Site setup

A field in the experimental farm of the Potato Research Centre (PRC) in Fredericton, New Brunswick, was used for this experiment (Fig. 3.1). The field was located on an east-north facing slope with a 17.6% slope of about 200 m long. A 110 m wide and 80 m long area in this field was used to establish 6 plots. Each plot was 80 m long and 6 m wide with 15 m wide space between plots for machine operations.

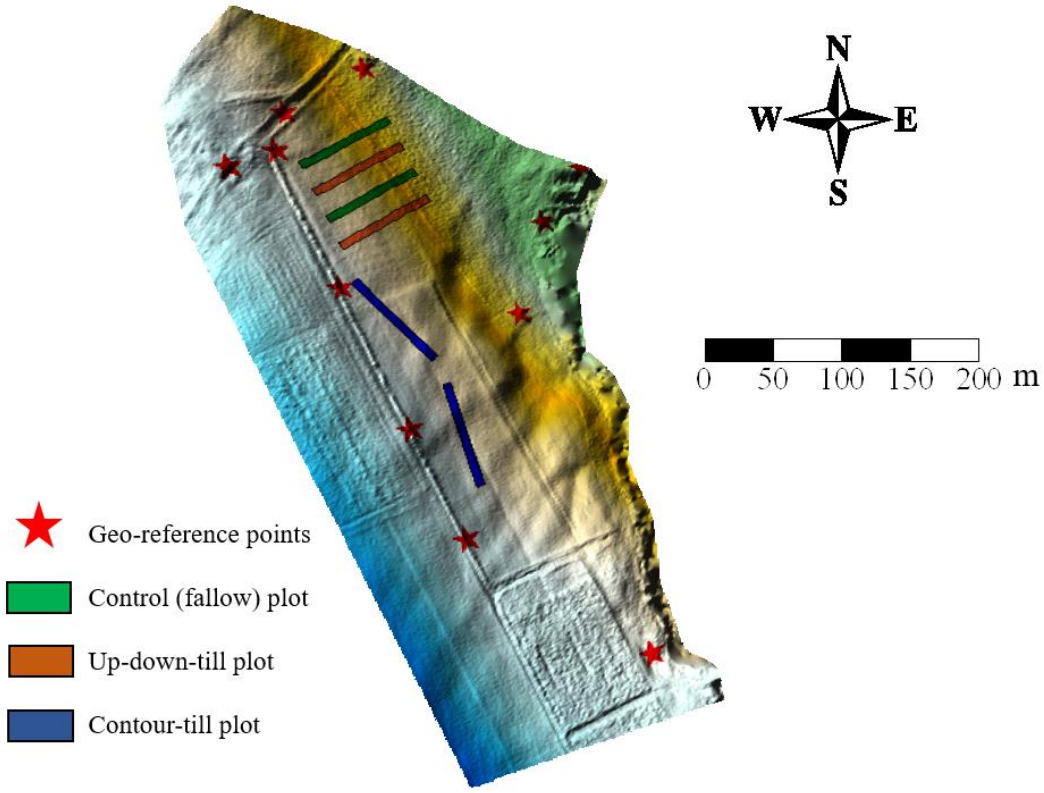

Figure 3.1. The experiment field and the layout of plots and geo-reference points used in this study.

Three tillage treatments, (i) potato, up-down-slope tillage (ii) potato, contour tillage and (iii) fallow, up-down-slope tillage (serving as the control), were examined. The two treatments and one control, each with two repeats, were randomly assigned to the 6 plots (Table 3.1; Fig. 3.1). For the up-down-slope tillage plots, they were oriented along the direction of the slope whereas for the contour tillage plots, they were oriented in the direction at a 5.2% angle to the contour lines of the slope.

Table 3.1. Tillage treatments and symbols for six plots.

Plot No.	Tillage treatment	Symbol
1	Potato contour tillage	T1
2	Potato contour tillage	T1
3	Potato up-down-slope tillage	T2
4	Potato up-down-slope tillage	T2
5	Fallow up-down-slope tillage	T0
6	Fallow up-down-slope tillage	T0

Eleven geo-reference points were established around this site (Fig. 3.1; Fig. 3.2). They were permanently marked with 1.2 m long iron bars of which 1 m was underground. Several plastic targets (Fig. 3.2) were installed along both sides of each plot at 2.5 m spacing. For both the geo-reference points and the targets, their relative coordinates were surveyed with a total station, establishing a coordinate system for both remote sensing methods.

Figure 3.2. Geo-reference point (left) and target (right).

A flume was installed at the bottom of each plot to collect snowmelt runoff, which was designed to monitor and record the flow rate and discharge during snowmelt period. Before snow falls, three HOBO soil temperature data logger were buried at 15cm depth of each plot at locations approximately 20 m, 40 m and 60 m away from the top of the plots, respectively. Three pairs of Echo soil moisture smart sensors were installed at the same locations. The pair of sensors was buried at 15 cm and 30 cm depths, respectively.

3.2.2 Equipment

A total station scanner and a metal frame close-range photogrammetry system were used to capture the soil surface morphology in this study. The previous study (Chapter 2) showed that these two methods can provide relatively high accuracy and spatial resolution.

3.2.2.1 Total station scanning (TSS)

For the TSS method, a Trimble VX spatial station was used. On top of the basic survey functions of a traditional total station, the Trimble VX spatial station is equipped with a camera and is able to scan a user-defined area at user-specified horizontal and vertical intervals. The detection range for scanning is ~150 m and the typical scanning speed is 5 points per sec. The theoretical accuracy of a single 3D point can reach 10 mm within the range of 150 m.

3.2.2.2 Close-range photogrammetry (CRP)

For the CRP method, Nikon D7000 cameras were used. The Nikon D7000 is based on a DX-format (23.6 x 15.6 mm) CMOS image sensor with 16.2 effective megapixel resolution. The maximum image dimensions are 4,928 x 3,262 pixels (Nikon Corporation, 2010). The weight of the camera is approximately 690 g, which is convenient to carry. A calibrated AF Nikkor 24 mm f/2.8D lens was used. The distortion of the lens was adjusted in the PhotoModeler Scanner® software. A detailed procedure of the calibration is attached in Annex I. To capture overlapped photos for the whole plot, the cameras were mounted on a platform. This platform had four legs welded to its four corners so that it can be moved easily (Fig. 2.2). Two brackets were established on the platform to install the poles for holding cameras. They were 2.1 m apart from each other and were 1.95 m away from the side of the platform. A camera base was installed on the top of each pole for adjusting the view angle of the camera. The height of the pole was adjustable as well (a maximum of 6 m above the ground). The poles were raised to the desired height, then each camera on the pole was connected to a laptop through a long cable and was controlled using the DCamCpature software for photo shooting.

3.2.3 Field experiment

To capture the morphological change for the period from after harvesting to snowmelt, plot surface morphology was captured at the beginning (November) and ending (May) of this period using the two remote sensing technologies (TSS and

CRP). The experiments were carried out in 2012 November/2013 May and 2013 November/2014 May respectively. However, some morphology data collected in 2012 November were unusable due to human errors. Therefore, only the morphology data collected in 2013 May, November, and 2014 May were used for the following analyses.

For the TSS method, the Trimble VX was mounted on a tripod at a height of ~1.5 m above the ground. Each plot was divided into three areas for scanning: upper-slope (covering the 6 m by 40 m length from the top), mid-slope (covering the following 20 m length) and lower-slope (covering the 20 m length to the bottom). For the upper slope and lower slope positions, the total station was located along the center line of the plot, 10 m away from the top and bottom edge of plot, respectively, whereas for the mid-slope position, the total station was located 5 m away from the side of the plot, 50 m away from the top of the plot. The scanning was all conducted at ground spacings of approximately 5 cm horizontally and 5 cm vertically (Fig. 3.3).

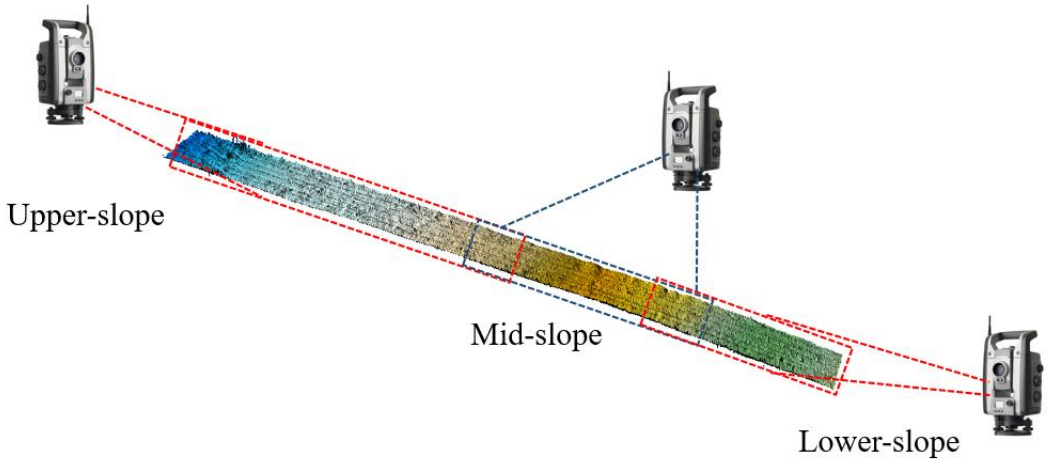

Figure 3.3. Setup of total station (three positions) for TSS method.

For the CRP method, the two cameras were raised to approximately 5 m above the ground to ensure a 60% horizontal overlap for the paired photos. Horizontal shooting angles for both cameras were ~70°. Each photo covered about a 4.9 m x 4.3 m area on the ground. The first pair of photos was taken at 6 m away from the top or the bottom of the plot, then the platform was moved downwards or upwards the plot, respectively, and subsequent photo pairs were taken at 2 m intervals, obtaining a 60% longitudinal overlap between two consecutive photos along the path. In total, 82 photos were taken for each plot.

3.2.4 Data extraction and analysis

3.2.4.1 DEM generation

For the TSS method, the raw 3D point cloud data were collected directly whereas for the CRP method, the photo images were taken. The images were imported into PhotoModeler Scanner® to extract 3D point cloud using scale-invariant feature transform (SIFT) algorithm. The 3D point cloud derived from both methods were imported into Surfer® software to generate grid format DEMs using kriging interpolation. For both methods, all DEMs were in 5 cm resolution (cell size = 5 cm), matching the raw data resolution of the TSS method.

3.2.4.2 Channel detection

During snowmelt period, channels in agriculture land were only generated through snowmelt runoff scouring. Therefore, the volume of channel derived from the DEMs can reflect soil lost by erosion in the channel correctly. Channelized erosion rate can

be assessed using both remote sensing methods. For both methods, DEMs derived after snowmelt were imported into the Surfer® software. The morphological parameters such as width and length of a channel were measured in Surfer®. In addition, a tool provided in Surfer® software was used to delineate the boundary for each channel. Then a planar surface was created for the delineated area to serve as a non-eroded surface. The volume of soil lost by erosion for each channel was assessed by subtracting the channel DEM from the planar surface DEM, and the volume was used to calculate the channelized erosion rate (Mg ha^{-1}) which was defined as:

$$\text{Channelized Erosion Rate} = \frac{\text{Soil Bulk Density} * \text{Channel Volume}}{\text{Plot Area}}$$

3.2.4.3 Elevation change

In agriculture land, many soil physical and hydrological processes such as gravitational subsidence, compactions by snow, soil freeze-thaw action, and snowmelt erosion and rainfall erosion can affect surface elevation change during snowmelt period. Therefore, elevation change can be considered as a combined morphological result of these processes. The surface elevation changes during winter period can be used to assess erosion if other processes were negligible, and can reflect the pattern of erosion if patterns of other processes were uniform. In order to obtain surface elevation change, the DEM derived before snowfall was subtracted from the DEM derived after snowmelt. Moreover, to compare the elevation change with soil erosion rate, it can be expressed on a mass basis (Mg ha^{-1}) as:

$$\text{Mass-based Elevation Change} = \text{Soil Bulk Density} * \text{Depth-based Elevation Change}$$

Then the elevation changes of the plots under different tillage treatments were compared.

Many soil physical and hydrological processes affecting soil surface elevation change were related to topography such as slope gradient and slope curvature. Therefore, it was valuable to investigate the relationship between the patterns of slope gradient and slope curvature and the pattern of elevation change. Firstly, three straight lines paralleled to the length of the plot were randomly selected. The values of elevation were extracted from the DEM for points every 5 m on these three lines. The elevation values were averaged for points of the three lines at the same distance from the top of the plot. These averaged elevation values were used to calculate slope gradient and slope curvature. The calculation method ensured the elimination of noises from measurement error and micro-topography and considered representative values at the field scale (5 m). With respect to elevation change value, a section centered at each of the 5 m points was created and the elevation change value for that section was extracted by averaging the elevation change values for all original DEM points in section. In the end, slope gradient, slope, slope curvature and elevation change values were determined at 5 m spacing along the length of the plot. The relationships among the three parameters were assessed using correlation analysis.

3.2.4.4 Field verification and validation

The seasonal erosion rate of the entire plot during the snowmelt period was derived from the flow monitoring data and was compared against the surface elevation change rate extracted from the DEMs comparisons, thereby assessing the contribution of snowmelt and rainfall erosion to the elevation change. The seasonal erosion rate (Mg ha^{-1}) was calculated as:

$$\text{Seasonal erosion rate} = \frac{\text{Sediment concentration} * \text{Seasonal runoff discharge}}{\text{Plot Area}}$$

The eroded sediment was obtained from the water samples collected manually from the flume (Fig. 3.4). From April 16th to 18th, 2014, flow rate determination and water sampling were conducted every hour after runoff occurring. A one-liter metal jar was placed under the outlet of the flume to collect water. The time took it to fill the one-liter jar was recorded for three times for which an average flow rate can be determined. Meanwhile, the water samples were collected and delivered to the laboratory in PRC for analysis of sediment concentrations. The weight of each water sample was measured firstly. Then these samples were filtered through a filter disc which had a pore size of 0.45 μm. When filtration was completed, the sediments remained on the disc were washed into a pre-weighed tin plate using distilled water. The plate was placed in the drying oven for at least an hour at 103-105 °C. At last, the amount of sediment in each plate was weighed. The sediment concentration (%) was calculated as below:

$$\text{Sediment concentration} = \frac{\text{Weight of Sediment}}{\text{Weight of Water Sample}} * 100\%$$

Figure 3.4. Manual water sample collection from a flume during snowmelt season.

Another parameter that was taken into account was the seasonal runoff discharge. It is assumed that evapotranspiration, percolation, and storage were negligible during snowmelt period so that the seasonal runoff discharge can increase to the limit under this scenario. Under this condition, two sources of seasonal runoff, melted snow and rainfall, were used to calculate the discharge. The snow depth and rainfall depth were recorded by the weather station located nearby. It was necessary to convert snowpack depth into melted snow depth. In many snow events, a 10% snow water equivalent can be applied, which means 1 cm of snow is equivalent to about 1 mm of water once snow is melted. However, according to the March-May 2014 report from Environmental and Climate Change Canada, parts of New Brunswick and Maine had snowpack had up to 50% snow water equivalent at the end of 2014 April. In order to

obtain the upper limit of seasonal runoff discharge during the snowmelt period, 50% snow water equivalent was applied to calculate the amount of melted snow depth.

After obtaining sediment concentration and seasonal runoff discharge during snowmelt period, the seasonal erosion rate can be calculated and used to compare with the elevation change rate derived from the remote sensing technologies.

On the other hand, during snowmelt period, several soil physical and hydrological processes impacting surface morphology were also related to soil temperature and soil moisture. Therefore, it was also important to test the relationships between the patterns of soil moisture and soil temperature and the pattern of elevation change. During the winter season, both soil moisture and soil temperature were recorded at 20 m, 40 m and 60 m distance from the top of the plot, respectively. At each location, the soil moisture and temperature derived from the sensors of the same depth were averaged. Moreover, three 10 m by 6 m sections at 20 m, 40 m, and 60 m were extracted from the Surfer® software to obtain the average elevation change of each section. After obtaining the value of each parameter (soil moisture, soil temperature, and elevation change) at each location, the relationships between these three parameters were investigated by comparing the patterns of soil moisture and soil temperature collected during winter period against the pattern of elevation change at corresponding locations.

3.3 Results and discussion

3.3.1 Channel detection

For all plots, after snow melting in 2013 spring, there was only one big channel (Fig. 3.5) generated in the Plot 5. The channel was located on the right part of the plot, started from the mid-slope area and ended at the bottom of the plot and the length of the channel was about 40 meters. The channel was clearly identifiable on DEMs of the Plot 5 generated using both remote sensing methods (Fig. 3.6). However, there was a difference between two methods. For the channel extracted from the TSS, a small part of the channel at the middle slope was disappeared in comparison to that extracted from the CRP, probably because the low shooting angle of the TSS which created gaps in the measured point cloud.

Figure 3.5. A large channel in the Plot 5 (T0) in May 2013.

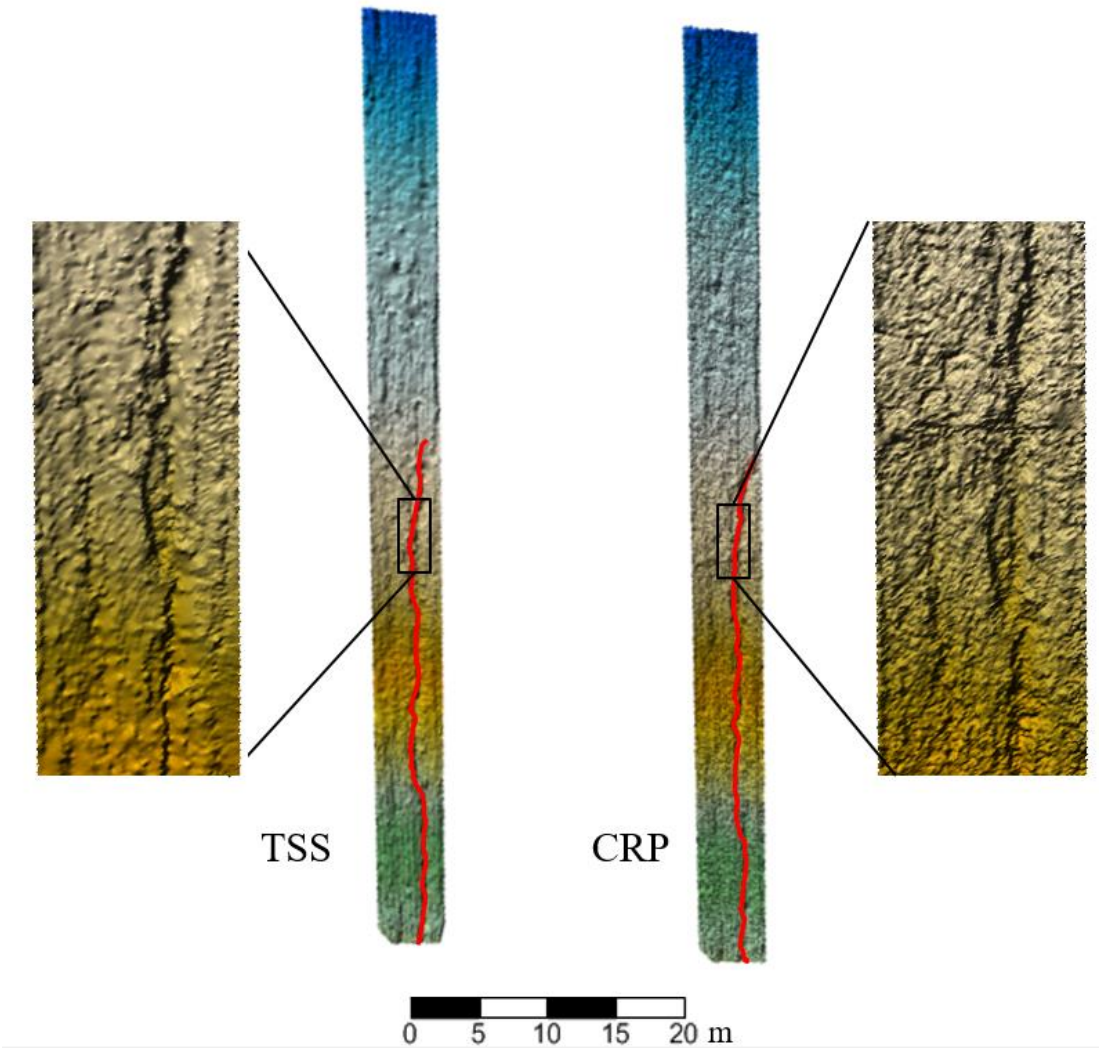

Figure 3.6. DEMs with a channel of Plot 5 (T0) generated using TSS (left) and CRP (right) methods in May 2013.

The result of Chapter 2 indicated that the CRP method usually overestimated channel depth whereas the TSS method usually underestimated that. This trend was observed for the channel depth in this study as well (Table 3.2). The channel depth derived from the TSS was ~1.8 cm less than that from the CRP. On the other hand, the CRP usually underestimated channel width whereas the TSS overestimated that, resulting in the channel width derived from the CRP being ~7.3 cm less than that of the TSS. The area of the channel was approximately 6.3% of the whole plot but soil rates for the channel

calculated on the whole plot basis were 48.6 and 59.8 Mg ha^{-1}, with the TSS and methods, respectively. Although there was a 10 Mg ha^{-1} difference between the two methods, both soil loss rates were much higher than tolerable soil loss rate, which was typically around 10 Mg ha^{-1}. This indicates the significant contribution channelized erosion may have towards total water erosion.

Table 3.2. Dimensions and channelized erosion rate (Mg ha^{-1}) of a channel derived from the DEMs using both methods during 2013 winter period (bulk density = 1.1 g cm^{-3} in AAFC Fredericton Research and Development Centre).

Method	Area (m^2)	Volume (m^3)	Length (m)	Width (cm)	Depth (cm)	Channelized Erosion Rate (Mg ha^{-1})
TSS	30.20	2.12	42.30	71.4	7.0	48.58
CRP	29.56	2.61	46.13	64.1	8.8	59.81

After snow melting of the following year (2014), for all plots, only two channels were created in the Plot 5 as well. Although serval small rills were observed in the photos (Fig. 3.7), they were too small to be captured by both remote sensing methods due to the size of these rills (width < 5 cm). The first channel (A) was located in the distance range of about 60 – 70 m from the top of the plot, and the second channel (B) was located in the range of about 40 – 45 m. Both channels were captured using the CRP method. However, the TSS method only captured channel A but not channel B (Fig. 3.8). It was likely that the low shooting angle of the TSS at side position was not able to capture small sized channel such as channel B.

Figure 3.7. A channel in the Plot 5 (T0) in May 2014.

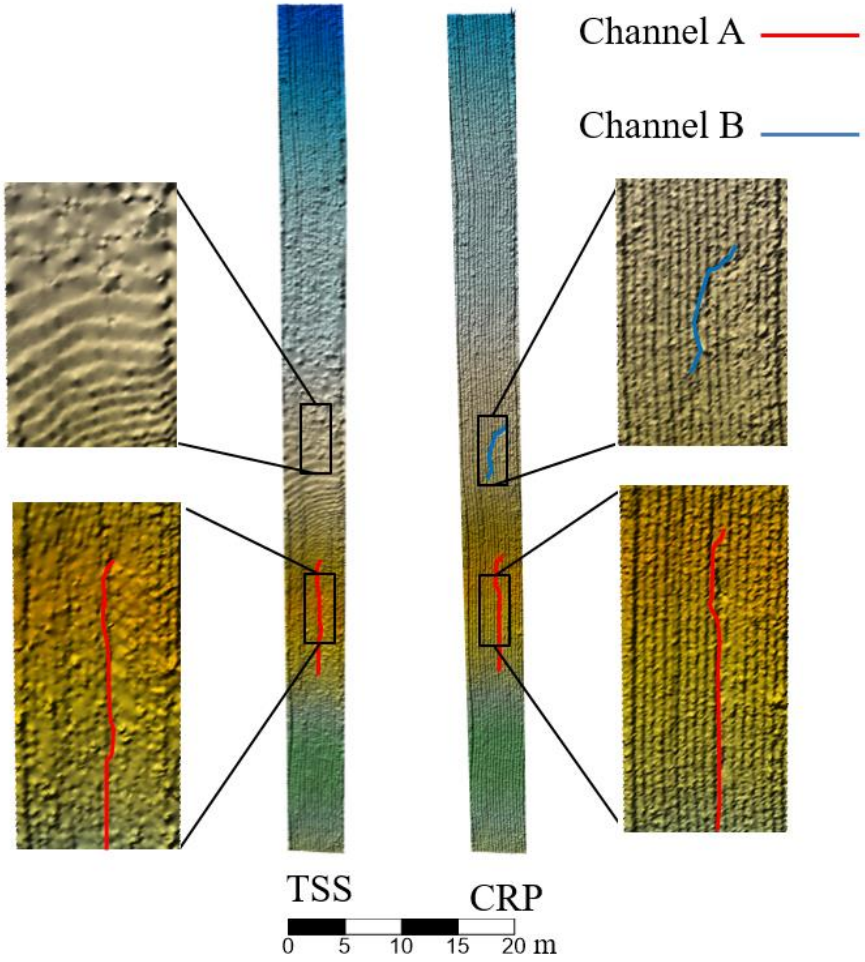

Figure 3.8. DEMs with two channels (channel A and channel B) of Plot 5 (T0) generated using TSS (left) and CRP (right) methods in May 2014.

For channel A, the average channel depth derived from the TSS method was ~1 cm less than that derived from the CRP method whereas the channel width derived from the TSS method was ~2.5 cm greater than that of the CRP method. For channel B, the average channel depth derived from the CRP method was only 0.85 cm, which was a subtle topographical feature to be captured. The total channelized erosion rate calculated from the CRP method was 2.06 Mg ha^{-1}, which was about 30 times less than that caused by the channel in the Plot 5 in 2013 (Table 3.3). A possible for that is probably the different fall tillage management in these two years. For example, more field furrows can be observed in the photos of spring 2014. The reason why channels only occurred in the Plot 5 for two years was not clear but it is likely related to the unique soil and topographic conditions of this plot.

Table 3.3. Dimensions and channelized erosion rate (Mg ha^{-1}) of a channel derived from the DEMs using both methods during 2014 winter period (bulk density = 1.1 g cm^{-3} in AAFC Fredericton Research and Development Centre).

	Method	Area (m^2)	Volume (m^3)	Length (m)	Width (cm)	Depth (cm)	Channelized Erosion Rate (Mg ha^{-1})
Channel A	TSS	3.18	0.05	10.31	30.8	1.6	1.15
	CRP	2.89	0.08	10.17	28.4	2.8	1.83
Channel B	CRP	1.17	0.01	6.36	18.4	0.9	0.23

3.3.2 Elevation change

The patterns of elevation change extracted from DEM comparisons were illustrated in the figures below. Since the CRP usually provided a better accuracy than the TSS on measuring elevation change (Chapter 2), the DEMs derived from the CRP method were used for the elevation change comparisons (Fig. 3.9; Fig. 3.11; Fig. 3.13; Fig.

3.15; Fig. 17; Fig. 19).

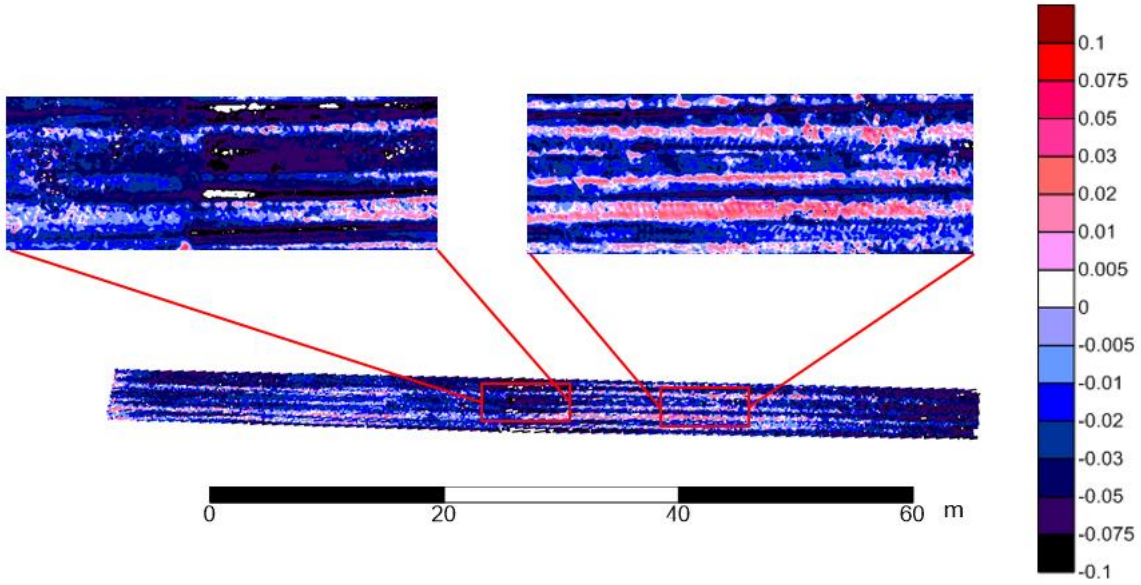

Figure 3.9. Elevation changes (m) of Plot 1 (T1) generated using CRP method for the period from Nov 2013 to May 2014 (red color represents elevation rise; blue color represents elevation drop).

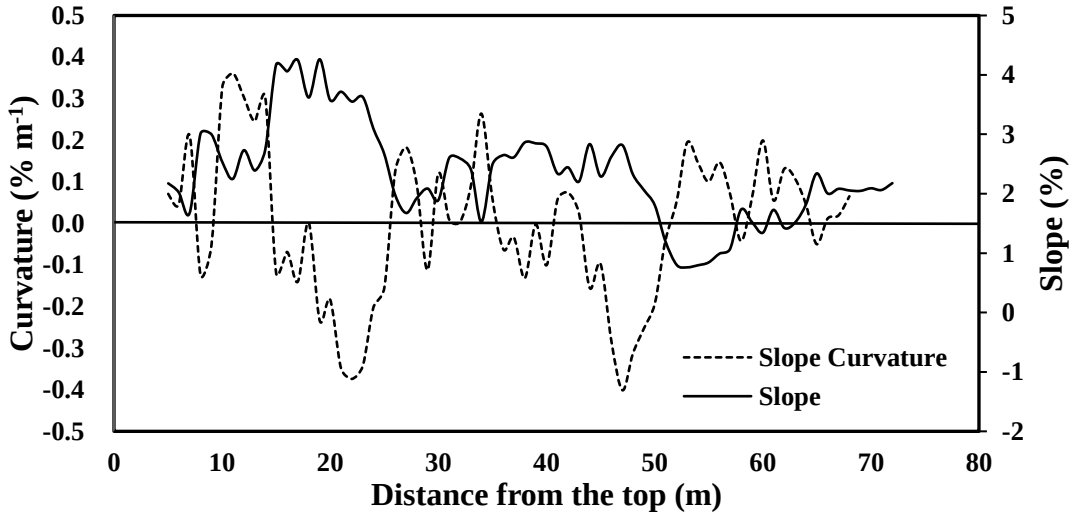

Figure 3.10. Lengthwise slope curvature (% m^{-1}) and slope gradient (%) of Plot 1 (T1) in May 2014.

Plot 1 was a contour plot oriented downslope from left to right (Fig. 3.9). Slope gradient ranged between 1% – 4% and slope curvature ranged between -0.4% m^{-1} – 0.4% m^{-1} (Fig. 3.10). There was a drop in elevation as a whole for this plot. Higher

elevation drop was observed in the distance range of approximately 0 m – 15 m from the left of the slope. Lower elevation drop was observed in the range of 20 m – 25 m and the elevation drop increased again in the range of 30 m – 40 m. At about 40 m – 50 m, there was a substantial decrease of elevation drop due to a slight concave shape at the slope. Beyond 50 m, the higher elevation drop was observed again, probably because of the increasing slope gradient and convex shape at the slope. Patterns have also been observed along the plot with the artificial morphological features–small ridges and furrows created during the harrowing in the fall of 2013. There was an elevation drop on ridges whereas there was a slight elevation rise in many of the furrows.

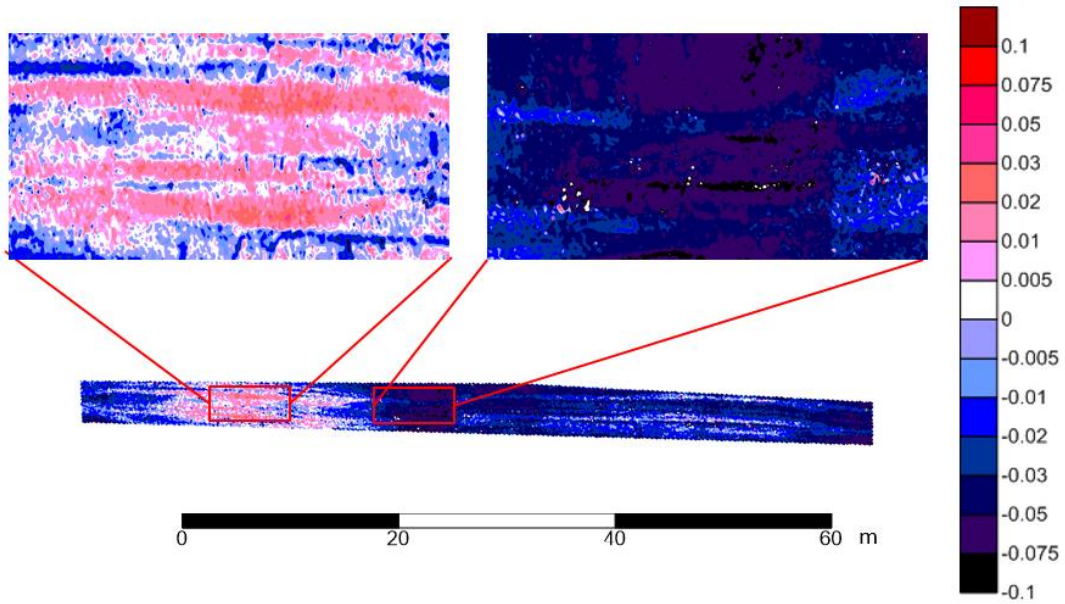

Figure 3.11. Elevation changes (m) of Plot 2 (T1) generated using CRP method for the period from Nov 2013 to May 2014 (red color represents elevation rise; blue color represents elevation drop).

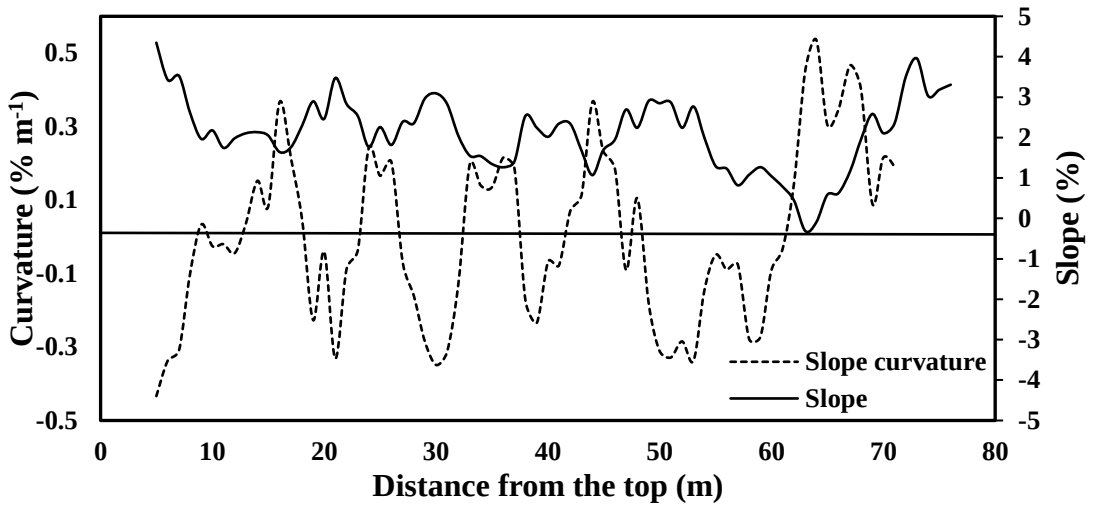

Figure 3.12. Lengthwise slope curvature (% m^{-1}) and slope gradient (%) of Plot 2 (T1) in May 2014.

Plot 2 was a contour plot oriented downslope from right to left (Fig. 3.11). Slope gradient ranged between 0% – 4% and slope curvature ranged between -0.4% m^{-1} – 0.5% m^{-1} (Fig. 3.12). There was an elevation drop in the range of 0 m to 40 m from the right of the plot (Fig. 3.11). From 40 m to 50 m, a higher elevation drop was observed, probably because of a decreasing slope gradient. A substantial elevation rise was observed at 50 m to 60 m due to a concave shape and a dramatic decreasing slope gradient.

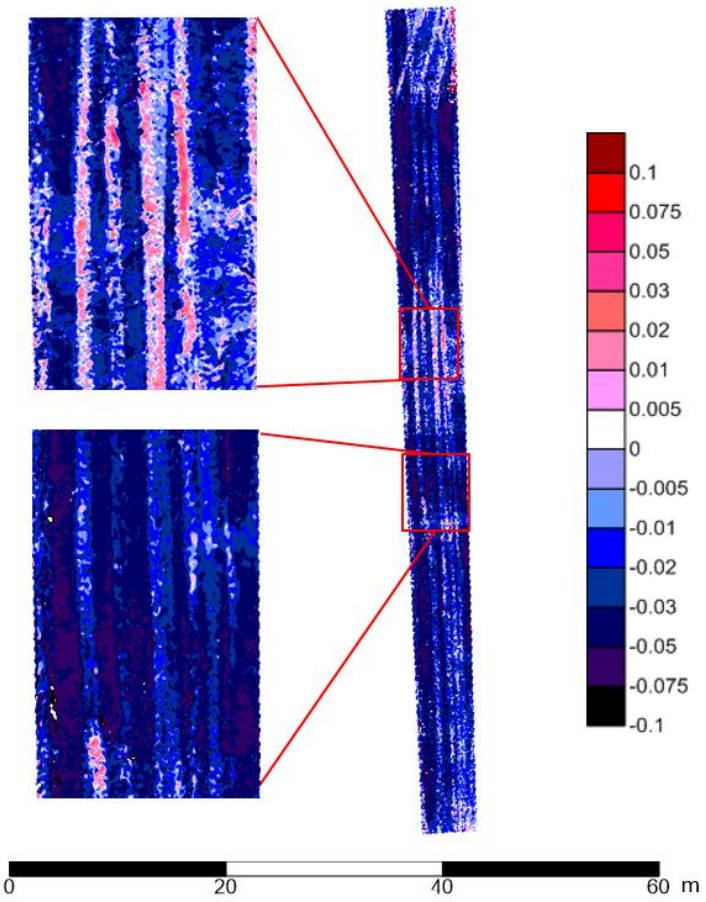

Figure 3.13. Elevation changes (m) of Plot 3 (T2) generated using CRP method for the period from Nov 2013 to May 2014 (red color represents elevation rise; blue color represents elevation drop).

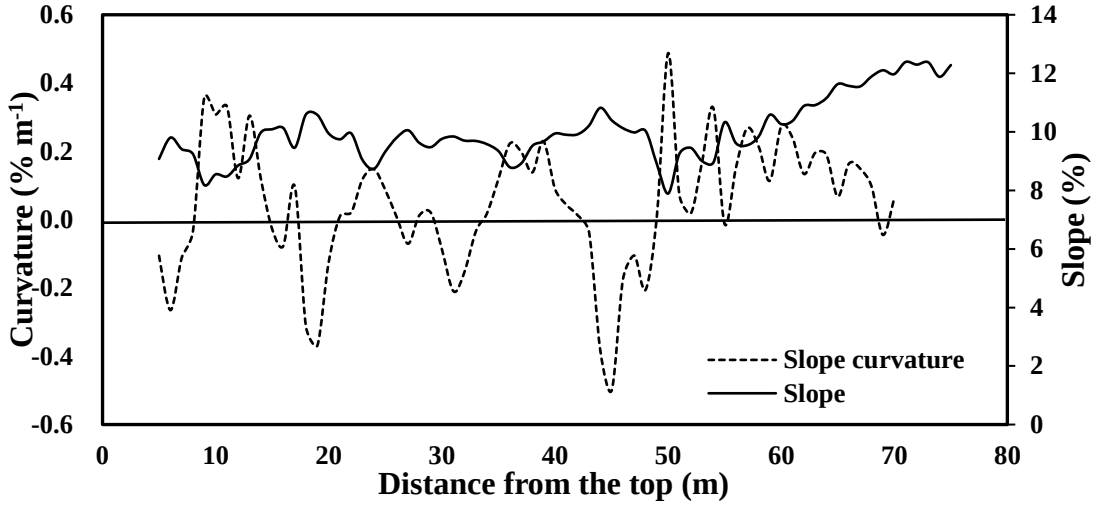

Figure 3.14. Lengthwise slope curvature (% m^{-1}) and slope gradient (%) of Plot 3 (T2) in May 2014.

Plot 3 was an up-down-slope plot oriented downslope from top to bottom (Fig. 3.13). Slope gradient ranged between 8% – 12% and slope curvature ranged between -0.5% m^{-1} – 0.5% m^{-1} (Fig. 3.14). There was a net drop in elevation as a whole for this plot. From 10 m to 25 m from the top, a higher elevation drop was observed. There was a substantial decrease of elevation drop rate in the range of 25 m to 40 m. There were elevation rises observed in the artificial channels at those locations. Beyond 40 m, the elevation drop was increased again, probably because of a convex shape at the slope and an increasing slope gradient. However, in the range of 45 m to 50 m, a large concave shape at the slope with decreasing slope gradient was observed, resulting in a lower elevation drop at this location.

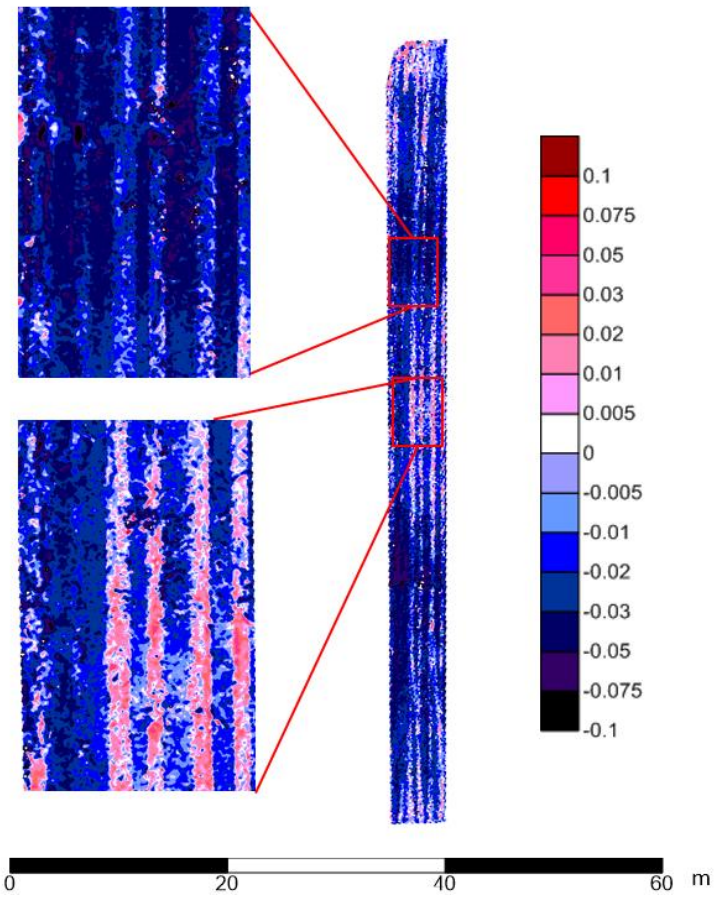

Figure 3.15. Elevation changes (m) of Plot 4 (T2) generated using CRP method for the period from Nov 2013 to May 2014 (red color represents elevation rise; blue color represents elevation drop).

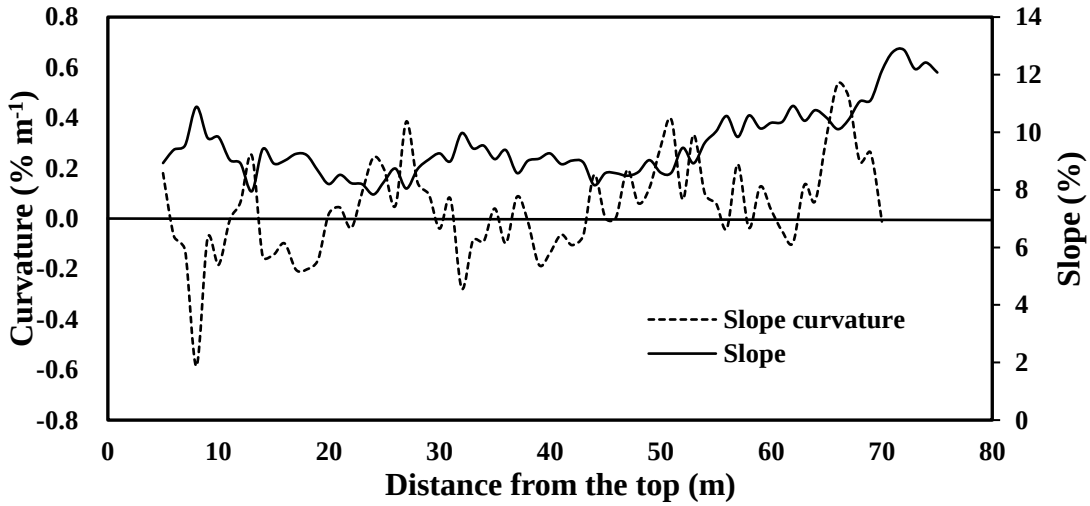

Figure 3.16. Lengthwise slope curvature (% m^{-1}) and slope gradient (%) of Plot 4 (T2) in May 2014.

Slope gradient of the Plot 4 ranged between 8% – 13% and slope curvature ranged between -0.6% m^{-1} – 0.6% m^{-1} (Fig. 3.16). The trend for elevation change of the Plot 4 (Fig. 3.15) was slightly different to that of the Plot 3. The elevation change rate decreased in the range of approximately 30 to 50 m. In addition, soil accumulation was observed in the channel area at the same locations. At about 50 m to 70 m, the slope gradient experienced an increase, resulting in an increase of elevation drop as well.

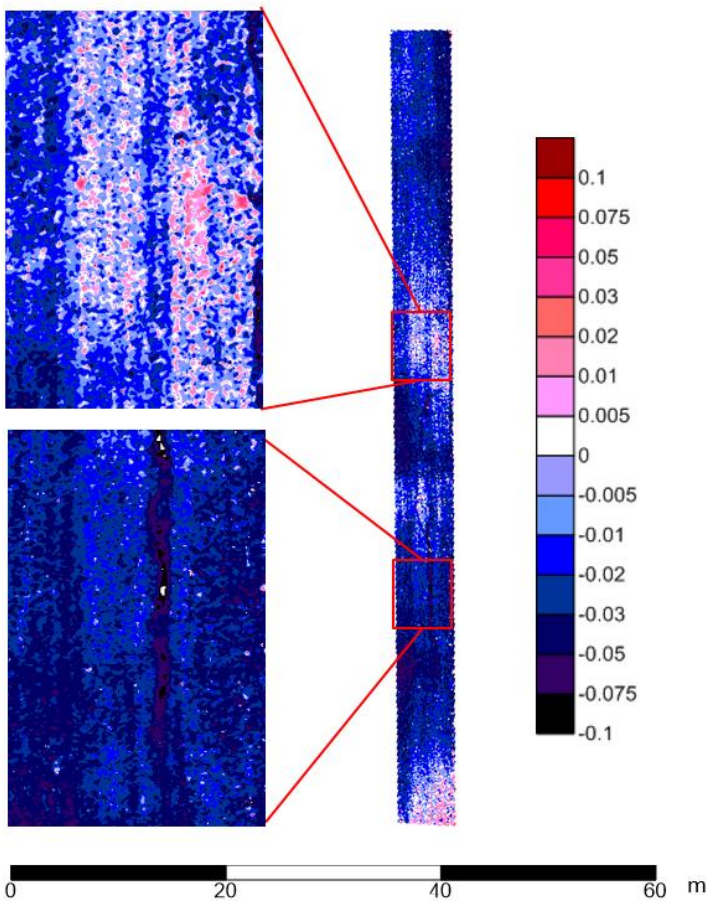

Figure 3.17. Elevation changes (m) of Plot 5 (T0) generated using CRP method for the period from Nov 2013 to May 2014 (red color represents elevation rise; blue color represents elevation drop).

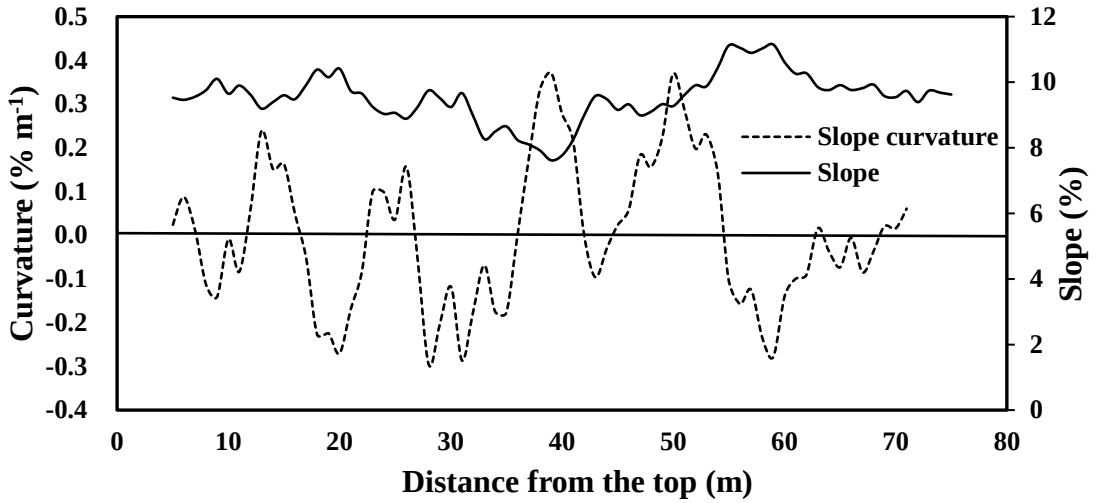

Figure 3.18. Lengthwise slope curvature (% m^{-1}) and slope gradient (%) of Plot 5 (T0) in May 2014.

For Plot 5, slope gradient ranged between 7% – 11% and slope curvature ranged between -0.3% m^{-1} – 0.4% m^{-1} (Fig. 3.18). A substantial decrease of elevation drop was observed in the range of 25 m – 35 m, probably because of a concave shape at the slope and a decrease slope gradient. As a convex shape at slope occurred at 35 m – 45 m, an increase of elevation drop was observed. In the range of 45 m to 55 m, a decrease of elevation drop was observed again, probably caused by a slight concave shape and a mild decreasing slope gradient (Fig. 3.17).

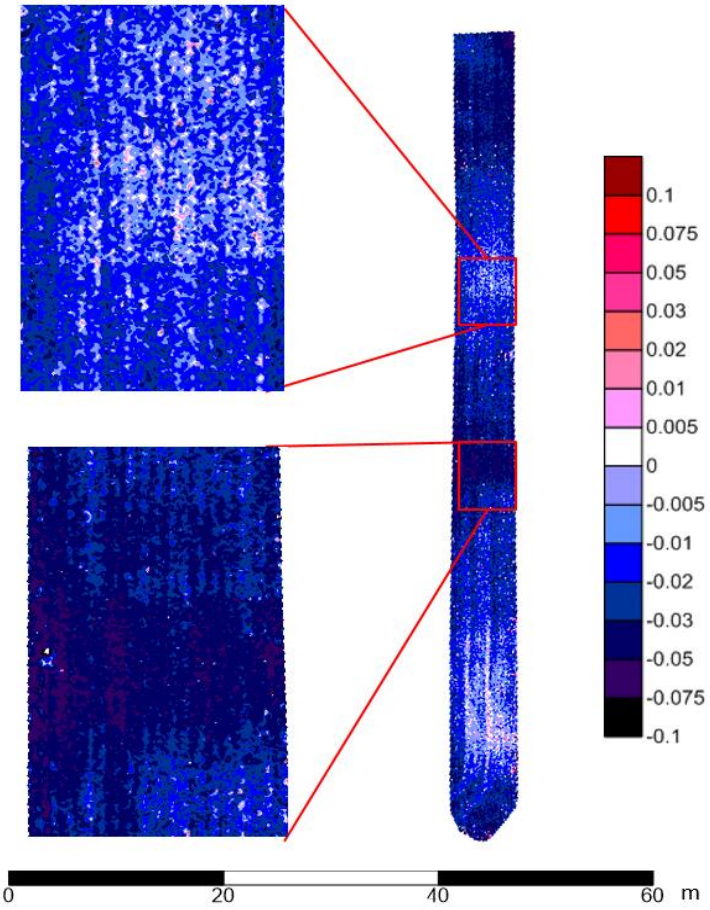

Figure 3.19. Elevation changes (m) of Plot 6 (T0) generated using CRP method for the period from Nov 2013 to May 2014 (red color represents elevation rise; blue color represents elevation drop).

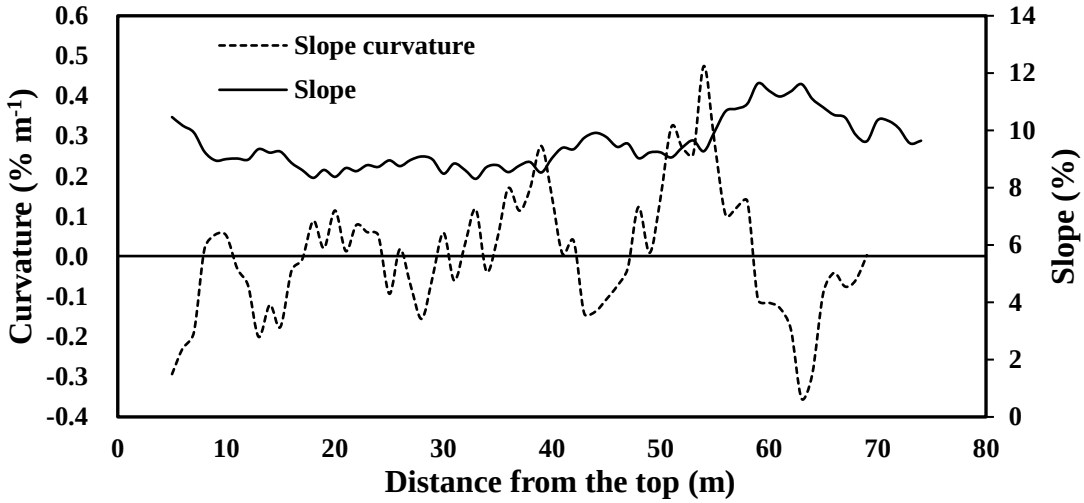

Figure 3.20. Lengthwise slope curvature (% m^{-1}) and slope gradient (%) of Plot 6 (T0) in May 2014.

The trend for elevation change of the Plot 6 was similar to that of the Plot 5 (Fig. 3.19), probably because both plots were plowed under the same treatment. Slope gradient ranged between 8% – 12% and slope curvature ranged between -0.3% m^{-1} – 0.5% m^{-1} (Fig. 3.20). The slope gradient rise resulted in a decrease of elevation drop. Overall, DEMs comparison of all 6 plots showed a lowering of the surface as a whole for all Plots (Table 3.4). The elevation drop ranged from 2.1 cm to 2.9 cm. There was no obvious difference between different tillage treatments, probably because all soil biophysical processes had the similar influence on bare ground for each plot. The largest elevation drop was observed from the Plot 1 under T1 whereas the least elevation drop was found from the Plot 4 under T2. With respect to the pattern of elevation change, for the most plots expect for the Plot 4, higher elevation drop usually was observed at the middle slope whereas before and after this area, lower elevation drop was found. Many soil physical and hydrological processes such as gravitational subsidence, compactions by snow, soil freeze-thaw action, and snowmelt erosion and rainfall erosion have an impact on surface elevation change during the winter period. Therefore, the pattern of elevation change can be considered as a combined morphological result of these processes. The contributions of these processes to elevation change were verified in the following part.

Table 3.4. Mass-based (Mg ha^{-1}) and depth-based (cm) elevation drop with different tillage treatments using remote sensing methods during the winter period (bulk density = 1.1 g cm^{-3} in AAFC Fredericton Research and Development Centre).

Plot No.	Tillage treatment	Mass-based elevation drop (Mg ha^{-1})	Elevation drop (cm)
1	T1	314.49	2.9
2	T1	256.50	2.3
3	T2	299.86	2.7
4	T2	231.67	2.1
5	T0	263.35	2.4
6	T0	258.56	2.4

With respect to local topography, it appeared that the correlation coefficients between the elevation change and slope gradient and between the elevation change and slope curvature of few plots were significant (Table 3.5). For the Plot 2 and the Plot 6, elevation change was found to correlate significantly with slope gradient whereas for the Plot 1 and Plot 3, elevation change was correlated with slope curvature significantly, indicating that the impact of slope gradient and curvature on observed elevation changes were not strong for most of the plots.

Table 3.5. Correlation Coefficient (r) between elevation change and slope gradient and between elevation change and slope curvature for 6 plots during the winter period.

Correlation Coefficient (r)	Plot 1	Plot 2	Plot 3	Plot 4	Plot 5	Plot 6
Between Eleavtion change and Slope gradient	0.08	-0.35 *	0.14	0.11	-0.14	0.53 *
Between Elevation change and Slope curvature	-0.59 *	-0.06	-0.32 *	0.01	-0.22	-0.19

3.3.3 Field verification and validation

Soil moisture experienced a dramatic increase (~0.2 m^3 m^{-3}) on April 9th, 2014 (Julian date 98), probably because snowmelt runoff occurred (Fig. 3.21). Water content started to percolate downwards soil surface. On April 25th (Julian date 114), moisture content at different layers became the same, indicating that most water infiltrated deep into the ground. Moreover, no snow and runoff were observed on the soil surface. Therefore, it is assumed that the snowmelt runoff happened between 2014 April 9th and 25th. However, the water sampling was only conducted from 2014 April 16th to 18th due to field accessibility. In order to obtain the sediment concentration during the whole snowmelt period, it is assumed that sediment concentration was equal for each day so that the measured daily sediment concentration can be used.

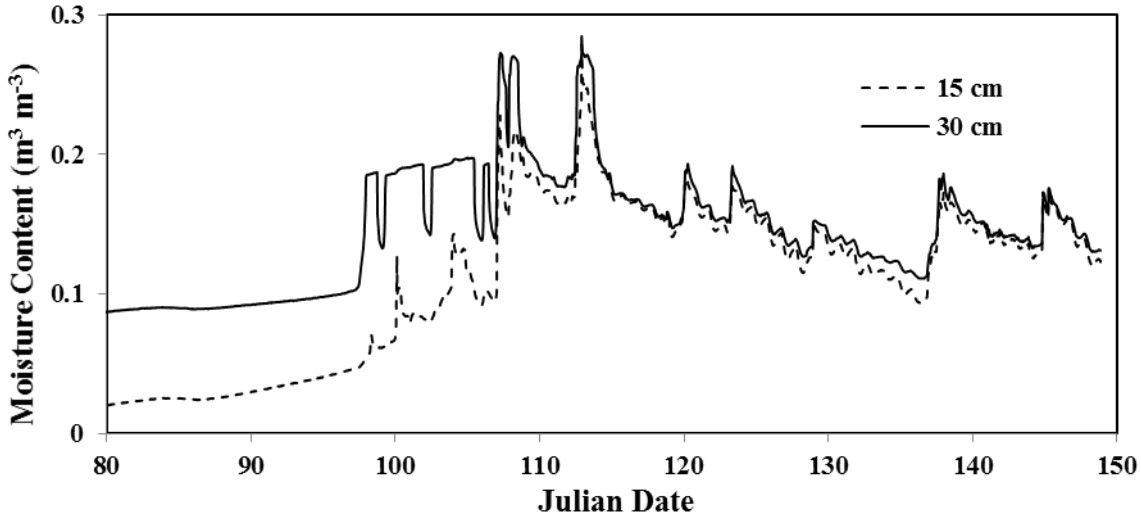

Figure 3.21. Soil moisture (m^3 m^{-3}) during the spring period (from 2014.03.22 to 2014.05.30) in AAFC Fredericton Research and Development Centre.

Water samples were collected for the up-down slope plot during the snowmelt period. On the nearby weather station, snow depth was 42.63 cm during the snowmelt period, which can be translated to 21.32 cm melted snow depth at the end of April 2014. Moreover, the rainfall depth during snowmelt period was 2.89 cm. In total, the depth of seasonal runoff discharge was 24.21 cm. Data in Table 3.6 indicated that the erosion rates derived from the water samples were much smaller than elevation change rate, suggesting that the observed elevation drops were likely not due to snowmelt and rainfall erosion but soil biophysical processes such as gravitational subsidence, snow compaction, and freeze-thaw action. Among these plots, the Plot 4 had the largest seasonal erosion and the least elevation change at same time. Moreover, there was a trend of the plots under T0 treatment with a smaller seasonal erosion rate, probably because T0 had fewer disturbances than T2. However, this trend was not observed in elevation change. In addition, the measured seasonal erosion rate of the Plot 5 was only 0.69 Mg ha^{-1}, which was smaller than the channelized erosion rate (2.06 Mg ha^{-1}) extracted from the CRP method, indicating that most soil loss from the channels was deposited on lower slope of the plot.

Table 3.6. Measured seasonal erosion rate (Mg ha^{-1}) over the entire plot and elevation drop (Mg ha^{-1}) derived from the remote sensing methods under different tillage treatments during the winter period (bulk density = 1.1 g cm^{-3} in AAFC Fredericton Research and Development Centre).

Plot No.	Tillage treatment	Seasonal erosion rate (Mg ha^{-1})	Depth-based seasonal eroison (cm)	Mass-based elevation drop (Mg ha^{-1})	Elevation drop (cm)
3	T2	2.04	0.02	299.86	2.7
4	T2	7.42	0.07	231.67	2.1
5	T0	0.69	0.01	263.35	2.4
6	T0	1.17	0.01	258.56	2.4

On the other hand, it is also important to investigate the relationships between the patterns of soil moisture and soil temperature and the pattern of elevation change during the winter period. The only completed soil moisture and soil temperature dataset was collected from the Plot 4 due to equipment limitations. For the 15 cm deep soil temperature at three different locations, there was no clear difference between them (Fig. 3.22). On Dec. 8th, 2013 (Julian date 341), the soil temperature of the Plot 4 fell below zero degree, indicating the ice was formed in the soil surface so that the surface morphology was hard to be changed.

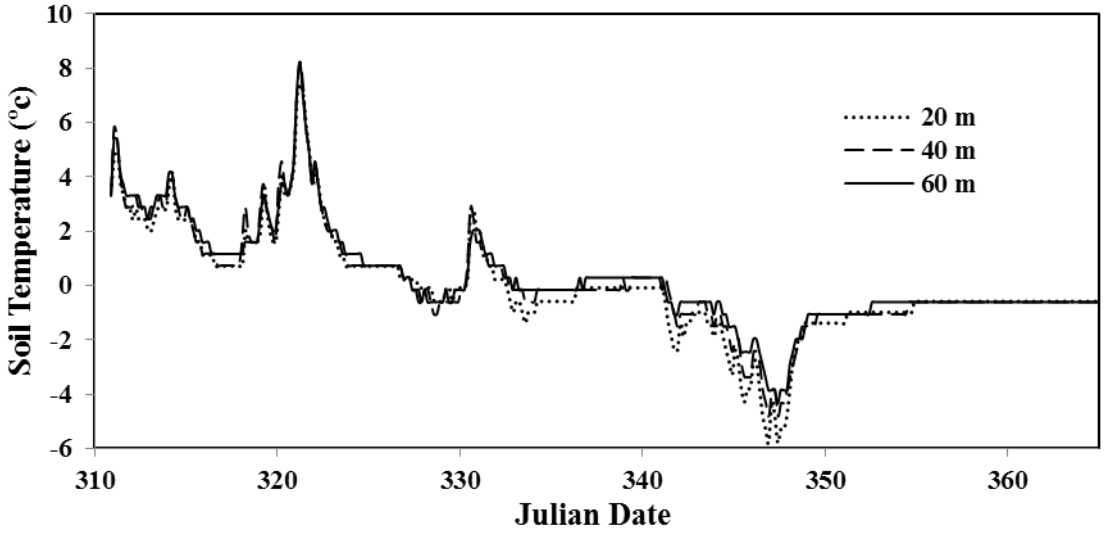

Figure 3.22. Soil temperature (°c) during the winter period (from 2013.11.06 to 2013.12.31) at three locations (20 m, 40 m and 60 m) in Plot 4.

For the 15 cm deep soil moisture at three different locations, obvious differences between them can be observed (Fig. 3.24). When ice was formed in the soil on Dec. 8th (Julian date 341), the soil moisture content at 20 m (0.083 m^3 m^{-3}) was lower than that at 60 m (0.137 m^3 m^{-3}) and the moisture content at 40 m (0.174 m^3 m^{-3}) was the largest among three locations, which was about 2.1 times larger than that at 20 m. This indicated that the greatest expansion in volume from water to ice can be observed at 40 m location. Therefore, after snow melting, lower elevation drop or even elevation rise should be observed at 40 m position.

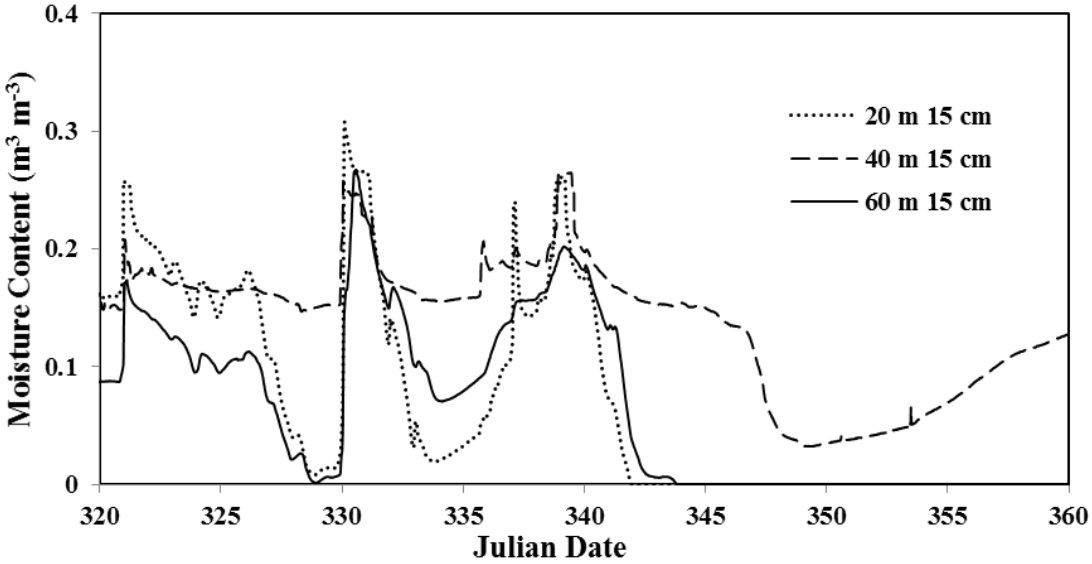

Figure 3.23. Soil moisture (m^3 m^{-3}) during the winter period (from 2013.11.15 to 2013.12.31) at three locations (20 m, 40 m and 60 m) in Plot 4.

During the beginning of the thawing season, the soil moisture content at 40 m was still the greatest among three locations (Fig. 3.25). Meanwhile, the soil moisture content at 60 m experienced an increase as snowmelt runoff flowed downwards the Plot 4. Conversely, the moisture content at 20 m experienced a slight decrease due to the runoff running. In the end, the pattern of moisture content at three locations became similar.

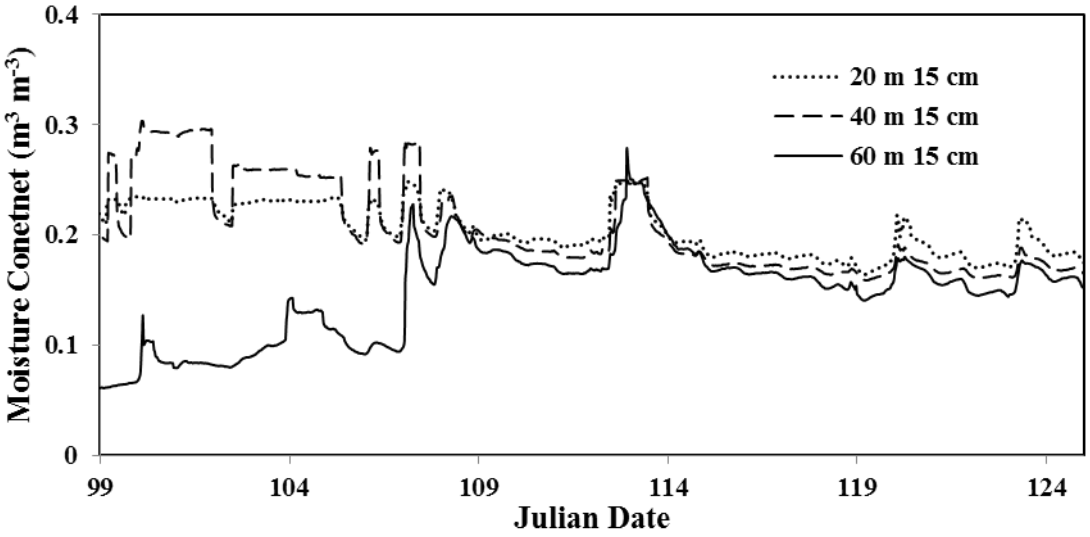

Figure 3.24. Soil moisture (m^3 m^{-3}) during the snowmelt season (from 2014.04.09 to 2014.05.06) at three locations (20 m, 40 m and 60 m) in Plot 4.

By comparing the pattern of elevation drop (Table 3.7) with the pattern of soil moisture, a significant relationship between them can be observed. The largest soil moisture content at 40 m can be found when ice was formed. Meanwhile, moisture content at 60 m was the second largest, followed by that at 20 m. After snow melting, the pattern of elevation drop had a strong negative relationship with the pattern of soil moisture during freezing period. For example, the elevation drop at 40 m was least among three locations, probably because the expanded soil particles reduced the impact of gravitational subsidence, compactions by snow, erosion on soil surface morphology. Therefore, it suggested that the observed elevation drops were likely associated with the freeze-thaw action but not the snowmelt and rainfall erosion actions.

Table 3.7. Soil moisture content (m^3 m^{-3}) during the freezing period and elevation drop (cm) during the winter period at three locations (20 m, 40 m and 60 m) in Plot 4.

Position (m)	Averge soil moisture content on Dec. 8th (m^3 m^{-3})	Elevation drop (cm)
20	0.083	3.2
40	0.174	1.1
60	0.137	2.0

3.4 Conclusion

The TSS and CRP methods differed in their performance to assess soil erosion rates. With the TSS method, side scanning was not able to capture soil surface morphology correctly due to its low shooting angle. With the CRP method, the volume of each channel derived from the CRP-generated DEM can be used to estimate the amount of soil lost by erosion. However, there was no good agreement between the estimates for the surface elevation change rate versus the snowmelt and rainfall erosion rate. Under the highest runoff discharge condition, seasonal erosion just contributed about 1% - 3% of the elevation change. The pattern of elevation change, however, was strongly related to the pattern of soil moisture content, indicating that the elevation changes during winter period were likely more associated with the freeze-thaw action than snowmelt and rainfall erosion actions.

Overall, the CRP method can detect channelized erosion correctly. The TSS method can also be used determine channelized soil erosion but only by avoiding side scanning. Neither method could be used to determine sheet erosion correctly.

Reference

Auzet, A.V., Boiffin, J., Papy, F., Ludwig, B., Maucorps, J., 1993. Rill erosion as a function of the characteristics of cultivated catchments in the North of France. Catena. 20(1-2): 41-62.

Bewket, W., Sterk, G., 2003. Assessment of soil erosion in cultivated fields using a survey methodology for rills in the Chemoga watershed, Ethiopia.Agriculture, ecosystems & environment. 97(1): 81-93.

Croke, J., Todd, P., Thompson, C., Watson, F., Denham, R., Khanal, G., 2013. The use of multi temporal LiDAR to assess basin-scale erosion and deposition following the catastrophic January 2011 Lockyer flood, SE Queensland, Australia. Geomorphology. 184: 111-126.

Edwards, L., Richter, G., Bernsdorf, B., Schmidt, R.G., Burney, J., 1998. Measurement of rill erosion by snowmelt on potato fields under rotation in Prince Edward Island (Canada). Canadian journal of soil science. 78(3): 449-458.

Evans, M., Warburton, J., 2011. Geomorphology of upland peat: erosion, form and landscape change. John Wiley & Sons.

Ghimire, S.K., Higaki, D., Bhattarai, T.P., 2013. Estimation of soil erosion rates and eroded sediment in a degraded catchment of the Siwalik Hills, Nepal. Land. 2(3): 370-391.

Li, L., Collins, R., Zhang, X., Wei, H., 2014. A Photogrammetric Method to Evaluate the Erosiveness of Fairbanks Silt with Different Treatments. In Climatic Effects on Pavement and Geotechnical Infrastructure. ASCE Publications. 176-182 p.

Li, S., 2012. Soil erosion and conservation. Encyclopedia of environmentrics, 2nd edition. John Wiley & Sons, Ltd.

Neugirg, F., Kaiser, A., Schmidt, J., Becht, M., Haas, F., 2014. Quantification, analysis and modelling of soil erosion on steep slopes using LiDAR and UAV photographs. Sediment Dynamics from the summit to the sea, IAHS Publ.

Øygarden, L., 2003. Rill and gully development during an extreme winter runoff event in Norway. Catena. 50(2): 217-242.

Perroy, R.L., Bookhagen, B., Asner, G.P., Chadwick, O.A., 2010. Comparison of gully erosion estimates using airborne and ground-based LiDAR on Santa Cruz Island, California. Geomorphology. 118(3): 288-300.

Quarterly Climate Impacts and Outlook: Gulf of Maine Region, 2014. Environmental and Climate Change Canada. Retrieved from: https://www.ec.gc.ca/eau-water/default.asp?lang=En&n=F121D795-1

Schowengerdt, R. A., 2007. Remote sensing: models and methods for image processing (3rd ed.). Academic Press. 2 p.

Spomer, R.G., Hjelmfeldt, A.T., 1983. Snowmelt runoff and erosion on Iowa loess soils. Transactions of the ASAE. 26: 1109–1116.

Welch, R., Jordan, T. R., 1983. Analytical Non-metric Close-Range Photogrammetry for Monitoring Stream Channel Erosion, PE & RS. 49(3): 367-374.

Welch, R., Jordan, T. R., Thomas, A. W., 1984. A photogrammetric technique for measuring soil erosion, Journal of soil and water conservation. 39(2): 191-194.

Ventura, G., Vilardo, G., Terranova, C., Sessa, E.B., 2011. Tracking and evolution of complex active landslides by multi-temporal airborne LiDAR data: The Montaguto landslide (Southern Italy). Remote Sensing of Environment. 115(12): 3237-3248.

Chapter 4

Quantifying soil surface evolution during summer using total station scanning and close-range photogrammetry

Abstract

Soil surface morphology is strongly affected by land management practices and soil biophysical processes such as soil erosion. Several remote sensing technologies such as 3D scanner and photogrammetry have been utilized to detect the surface morphology. However, studies up to date have focused on small-scale rill erosion.

In this study, a field experiment was conducted at the AAFC Fredericton Research and Development Centre, New Brunswick, on 6 m by 80 m large plots to determine surface morphological changes under three tillage treatments during summer. The treatments involved (i) potato cropping with up-down-slope tillage, (ii) potato cropping with contour tillage, and (iii) fallowing with up-down-slope tillage (control). Surface morphologies (elevation, slope, curvature) were scanned and evaluated at the beginning and end of the summer period.

For the summer period, the plots showed a drop in elevation in the distance ranges of approximately 0 m – 20 m and 40 m – 50 m from the top of the plot. On the other hand, the surface rise was observed at approximately 20 – 40 m and 50 – 70 m. Assuming these elevation changes were due to soil erosion, they can produce a net soil loss of 55 Mg ha^{-1} to 110 Mg ha^{-1} for the cropped plots, and a net soil gain of 22 Mg ha^{-1} to 88 Mg ha^{-1} for the fallowed plots. For the fallowed plots, the reason caused a net soil gain probably because the presence of vegetation. Therefore, more developments are needed to reduce the impact of vegetation on the results.

4.1 Introduction

Potato is the main cash crop in New Brunswick. Summer period is a critical period for potato growth. In this period, the soil surface morphology is subject to great changes and may affect soil properties and many biophysical processes such as runoff generation and plant growth. Soil surface morphology can be affected by many soil biophysical processes such as gravitational subsidence after tillage and wet/dry process. However, the process which has the most important influence is often soil erosion. For example, water erosion can be caused by rain drops hitting on inadequately protected soil surface and by the action of runoff. When raindrops hit the soil surface, soil particles can be detached from the ground. When rainfall intensity exceeds the infiltration rate or when the soil is saturated, overland flow is generated, initially as a thin layer of the sheet runoff. The splashed soil particles can be carried away by the thin layer of runoff, resulting in sheet erosion (Meyer et al., 1975). As runoff water accumulates downslope, its velocity accelerates. Usually, some small rills are formed downslope under this condition on bare soil after major rainfall events. According to the soil science society of America, rill is defined as “a small, intermittent water course with steep sides” and it is easy to be erased by tillage operations. Flow in rills through scouring is more erosive than sheet flow. Rills also serve as major pathways for soil particles detached by rill flow, raindrops, and sheet flow (Laflen et al., 1994). As a rill develops, it can be cut deeper and wider by water. Another form of water erosion is gully erosion. Gully can start from near the bottom

of the slope and gradually cuts its way back uphill. However, it can also be developed from rills or due to the clasped subsurface flow channel. Most ephemeral gullies in cultivated fields are topographically defined. They are often filled by tillage erosion but appeared repeatedly at roughly the same locations year after year. When a channel is too large to be filled by ordinary tillage operations, it becomes a classic gully (Poesen et al., 2003).

Due to the strong impact of soil erosion on the surface morphology, quantifying surface morphological change has been applied in many studies to assess soil erosion in the summer season. For example, manual survey methods have been used by many researchers to measure rill erosion (Bewket and Sterk, 2003; Govers, 1991; Hancock et al., 2008). Herweg (1996) indicated that this method usually has an error less than 15% with a careful measurement. However, this method cannot be used to detect inter-rill erosion. Inter-rill erosion can be detected using the erosion pin method where an erosion pin was established in the field and surface elevation change was recorded relative to a reference mark on the pin. This method has also been widely used to monitor the stream bank erosion (Couper et al. 2002; Lawler et al., 1997; Stott, 1997). Overall, these traditional survey methods are usually time-consuming and labor intensive. Also, these methods may cause disturbance to the soil surface, resulting in extra soil erosion and making repeated measurement impossible.

Morphological change can also be measured using remote sensing methods. Remote sensing is a technology to acquire information about an object or phenomenon

without physical contact (Schowengerdt, 2007). Many scientists used aerial-based remote sensing methods to measure the morphological changes at a large scale. However, aerial-based remote sensing methods have many limitations, including high costs, low resolution, and low mobility. With technical developments in the last decades, ground-based remote sensing methods have been used for measuring micro-topography. Emerging ground-based remote sensing methods include ground-based 3D scanner and close-range photogrammetry. As a useful technology, 3D scanner has been used widely. A decade ago, Schmid et al. (2004) conducted a small-scale study of erosion at a forest site near St. Märgen, Germany. In 2008, Nasermoaddeli and Pasche used this technology to quantify the change of the riverbank. Studies have shown that rill erosion can also be captured by laser scanning (Vinci et al., 2015). Many studies also utilized close-range photogrammetry to quantify soil erosion. Berger et al. (2010) conducted several rainfall simulation experiments in a 1 m by 2 m box and used the close-range photogrammetry technology to monitor the rill network. Gessesse et al. (2010) also employed this technology to assess the erosion, deposition and rill development on an irregular surface at a small scale.

Most erosion studies using remote sensing methods focused on rill erosion at a small scale, usually in a small plot. There is a lack of study at the field scale, for which soil surface is subjected to the influences of multiple processes and soil morphology change may have a spatial pattern relates to topography and soil conditions. Also,

there is a lack of study on an operating farm field, where the real-world conditions can be better represented and reflected. Potato fields in New Brunswick are under intensive cultivation, which may lead to severe soil erosion. Understanding how soil surface evolves at the field scale can provide useful information for erosion control on these fields.

In this study, soil surface morphology was measured using two ground-based remote sensing methods (3D scanner and close-range photogrammetry) during the early summer period (from after seeding to about one third canopy coverage), a critical period when the soil surface is bare and subject to the effects of many processes. The objectives were: (i) to quantify surface evolutions at the field scale under different potato tillage treatments during the early summer period, and (ii) to investigate the performance of the two ground-based remote sensing on detecting soil surface elevations during the early summer period.

4.2 Methodology

4.2.1 Site setup

The site of this study is located in the experimental farm of the Potato Research Centre (PRC) in Fredericton. A detailed description of the site can be found in the previous study (Chapter 3). In brief, 6 plots were established in the field. Each plot was 80 m long and 6 m wide.

Three treatments: (i) potato with up-down-slope tillage, (ii) potato with contour tillage, and (iii) fallow with up-down-slope tillage (serving as a control treatment), were examined in this study. Each treatment with two repeats was assigned to the 6 plots (Table 3.1; Fig. 3.1).

Eleven geo-reference points were established around this site (Fig. 3.1; Fig. 3.2). Each geo-reference point was permanently marked with a 1.2 m long iron bar, of which 1 m was buried underground to ensure that its location is not affected by frost heaving. Plastic targets were installed along both sides of each plot at 2.5 m intervals (Fig. 3.2). For both the geo-reference points and the targets, their relative coordinates were surveyed with a total station, establishing a coordinate system for both remote sensing methods.

4.2.2 Equipment

Soil surface morphology was captured using a total station scanner (TSS) and a close-range photogrammetry system (CRP). The equipment used in this study was the same as that used in the previous study and was described in detail elsewhere (Chapter 3). In brief, for the total station scanner, a Trimble VX spatial station was used. The machine features a scanning function which has a detection range of ~150 m with scanning speed of 5 points per second. The 3D point accuracy can reach 10 mm within the range of 150 m. For the close-range photogrammetry (CRP), Nikon D7000 cameras with a calibrated AF Nikkor 24 mm f/2.8D lens were used. This photogrammetry system used a metal frame as the platform (Fig. 2.2). Two cameras

were installed on two poles on the metal frame. The poles can be raised to a desirable height (max 6 m above the ground), and then each camera was connected with a laptop via a cable and was controlled using the laptop for photo shooting.

4.2.3 Field experiment

In this study, the goal was to capture the morphological change for the period when the soil surface is bare. The experiment was carried out in 2014 and soil surface morphology was captured on June 20th (approximately one week after seeding) and again on July 8th (when the potato field is at approximately one third canopy coverage). In addition, since there was a huge hurricane (Arthur) occurring on July 5th, 2014, an additional round of CRP measurements was conducted before this event on July 4th. Due to the limited time, TSS was not conducted on this date.

Procedures used in the field experiments were the same as those described in Chapter 3. For the TSS method, the Trimble VX was mounted on a tripod at a height of ~1.5 m above the ground. Each plot was divided into three areas (Fig. 3.4) for scanning: upper-slope (covering the 6 m by 40 m length from the top), mid-slope (covering the following 20 m length) and lower-slope (covering the 20 m length to the bottom). These scannings at different locations were conducted at ground spacings of approximately 5 cm horizontally and 5 cm vertically. For the scanning at the upper-slope or lower-slope locations, the total station was placed along the center line of the plot, 10 m away from the short edge of plot, whereas for the scannings at

the mid-slope location (50 m away from the top of the plot), the total station was placed at 5 m away from the side of the plots (Fig. 3.4).

For the CRP method, the two cameras were raised to approximately 5 m above the ground to capture photo pairs of approximately 60% horizontal overlap. Horizontal shooting angles for both cameras were ~70°. Each photo covered about 4.9 m x 4.3 m area on the ground. The first pair of photos was taken at 6 m away from the plot on the top, then the platform was moved downslope towards the plot and subsequent photo pairs were taken at 2 m intervals, obtaining around 60% longitudinal overlap. In total, 82 photos were taken for each plot.

4.2.4 Data extraction and analyses

4.2.4.1 DEM generation

Figure 4.1. An original photo (left) and a processed photo (right) of soil surface.

For the TSS method, the raw 3D point cloud data were obtained directly whereas for the CRP method, the photo images were imported into the PhotoModeler Scanner® to obtain 3D point clouds using the scale-invariant feature transform (SIFT) algorithm. For measurements obtained on July 4th and July 8th, because of crop and grass growth, the canopies interfered with the measurements so that the point clouds

data were for the surface of the canopy rather than for the bare soil surface. Since bare soil surface data are needed for measuring soil surface morphological changes, the effects of vegetation canopies must be removed. Unfortunately, there is no efficient way to distinguish vegetation canopy points from soil surface points with the TSS methods so that such filtering cannot be performed. However, since the CRP method is based on photos, vegetation canopy points and soil surface points can be distinguished by their color (green versus brown). In this study, the filtering was conducted in the MATLAB software. Prior to feeding the raw photo images into the PhotoModeler Scanner® software, they were imported into MATLAB. The green colored pixels in each photo were identified, and were converted to black (Fig. 4.5). The MATLAB processed photos were then imported into the PhotoModeler Scanner® software, in which black areas were considered as no data zone. Thus, the vegetation canopy points were eliminated in further processing.

For both remote sensing methods, the final 3D point cloud data were imported into the Surfer® software to generate grid format DEMs using kriging interpolation. All DEMs were in 5 cm resolution (cell size = 5 cm), matching the raw data resolution of the TSS method.

4.2.4.2 Channel detection

Channels were assessed based on one-time DEMs. For both remote sensing methods, DEMs of the plots at the time of about one third canopy coverage were imported into the Surfer® software. Channels were identified and the morphological parameters

such as width, depth, length and volume of these channels were measured in Surfer® software. In addition, a tool provided in Surfer® was used to delineate the boundary for each channel. A planar surface was then created on the top of each channel based on the boundary lines and was used as a reference surface for channel volume calculation. The volume of soil lost in each channel was assessed by subtracting the channel DEM from the planar surface, and it was used to calculate the channel erosion rate (Mg ha^{-1}) which was defined as:

$$\text{Channelized Erosion Rate} = \frac{\text{Soil Bulk Density} * \text{Channel Volume}}{\text{Entire Plot Area}}$$

4.2.4.3 Elevation change

Surface elevation change was assessed by the differences in DEMs taken at two times. For the early summer period, it was calculated by subtracting the DEM derived for July 8th, 2014 (approximate one-third canopy coverage) from the DEM derived for June 20th, 2014 (after seeding). The results of DEM comparisons reflect the pattern of the surface morphological changes during the early summer period. Depth-based elevation changes were converted to mass-based elevation change (Mg ha^{-1}) for the purpose of comparing with soil erosion rates:

$$\text{Mass-based Elevation Change} = \text{Soil Bulk Density} * \text{Depth-based Elevation Change}$$

Then the elevation changes of the plots under different tillage treatments were compared.

Many soil physical and hydrological processes affecting soil surface elevation change are related to topography. In order to investigate such relationship in our experiment, three topographical parameters (slope gradient (%), slope curvature (% m^{-1}) and elevation change (m)) were extracted from DEMs generated using the CRP method. Firstly, three straight lines paralleled to the length of the plot were randomly selected. The values of elevation were extracted from the DEM for points every 5 m on these three lines. The elevation values were averaged for points on the three lines at the same distances from the top of the plot. These averaged elevation values were used to calculate slope gradient and slope curvature. The calculation method ensured the elimination of noises from measurement error and micro-topography and considered representative values at the field scale (5 m). With respect to elevation change value, a section centered at each of the 5 m points was created and the elevation change value for that section was extracted by averaging the elevation change values for all original DEM points in the section. In the end, slope gradient, slope curvature, and elevation change values were determined at 5 m spacing along the length of the plot. The relationships among the three parameters were assessed using correlation analysis.

4.2.4.4 Method verification

No runoff or sediment data or soil property data were collected in this study so that direct validation of channel detection or elevation results was not possible. The method was verified by examining small areas that judged from the photos are

obvious soil loss or depositional areas. The photos taken from the CRP method were used to check the reliability of each DEM. For example, it can be visually determined on some photos that sediment were carried downwards the plot by runoff and rocks were buried underneath the soil surface. If these changes captured in the photos taken at the beginning and ending times of the early summer period were detected in the corresponding DEM comparison, it indicated that the DEM comparisons were able to reflect the reality of surface morphological change.

The obvious soil depositional areas can be easily found in the photos taken after the hurricane event. Two random soil depositional areas were selected from all plots. Then the photos taken before and after the hurricane event of these two areas were imported into PhotoModeler Scanner® to generate 3D point cloud data respectively. The final 3D point cloud data were imported into the Surfer® software to generate grid format DEMs with 5 cm resolution using kriging interpolation. In the end, surface elevation change was extracted by the differences in DEMs taken before and after the hurricane event.

4.3 Results and discussion

4.3.1 Channel detection

There was no channel observed in the early summer period due to the low amount of precipitation. After this early summer period, one channel was generated by the Arthur hurricane on July 5th, 2014. The channel was located in the Plot 5, which is

under the fallow up-down-slope tillage. In the photos (Fig. 4.2) taken in the Plot 5, a channel was observed in the distance range from approximately 40 m to 70 m from the top of the plot. A channel (red line) was also observed in DEMs (Fig. 4.3) using both remote sensing methods. However, there was a difference between two methods. For the channel extracted from the TSS method, a large portion of the channel was disappeared in comparison to that extracted from the CRP method. For the DEM extracted from the TSS, the whole channel was captured at the mid-slope location, probably because the side shooting of the TSS had less impacted by the grass canopies than the front shooting.

Figure 4.2. A channel of Plot 5 (T0) generated after the hurricane event.

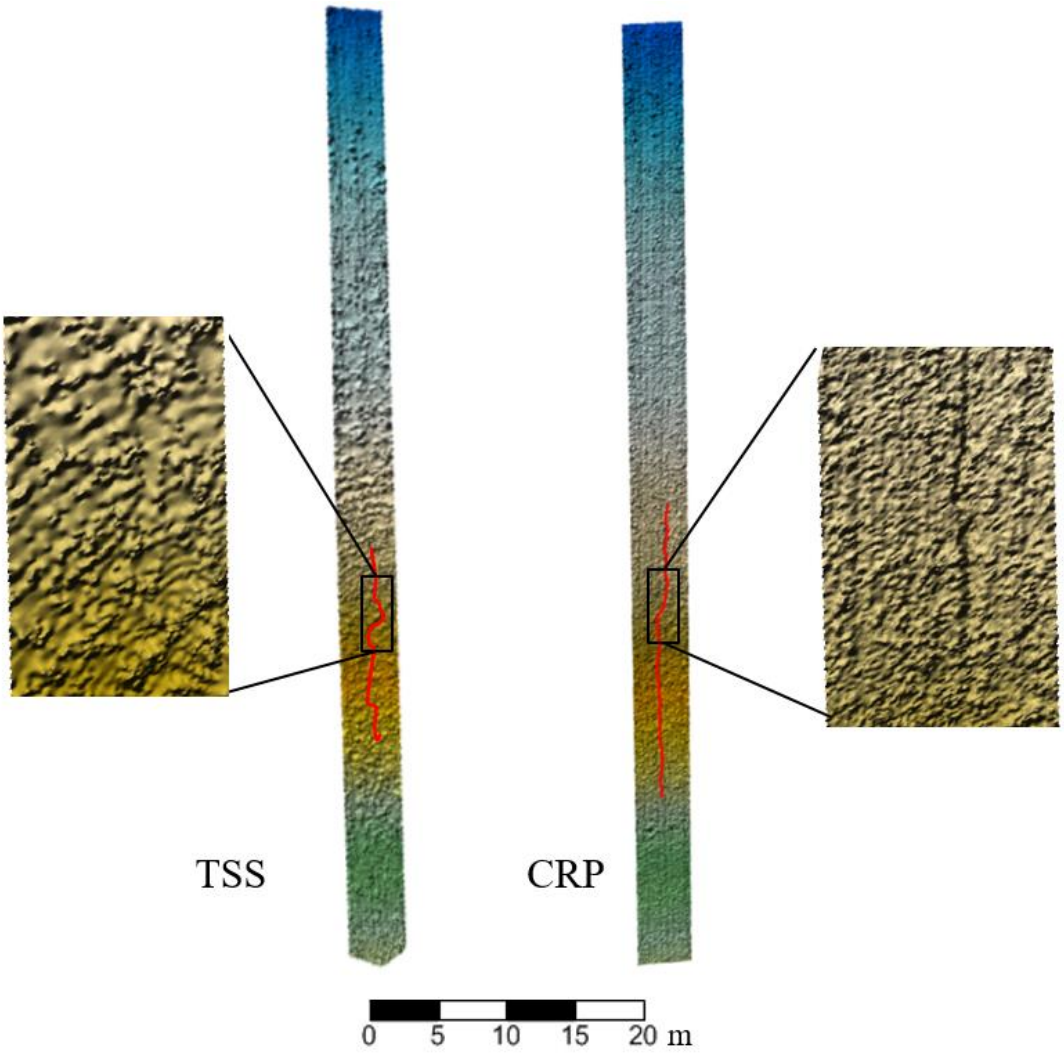

Figure 4.3. DEMs with a channel of Plot 5 (T0) generated using TSS (left) and CRP (right) methods on July 8th, 2014.

On July 5th, the precipitation depth of Arthur hurricane was 89.4 mm, which was equivalent to 4.7 mm $hour^{-1}$, generating a large runoff over the plots. By comparing the results of both methods (Table 4.1), it indicated that the channel width extracted from the TSS was twice wider than that extracted from the CRP, probably because most laser lights emitted from the total station were reflected back by the grass canopies, causing an error on detecting channel width. The soil loss rate extracted from the TSS was considered less accurate because the width was too wide compared

to field observation and two portions of the channel were missing. The result indicates that grass canopy poses a great challenge for the TSS method to capture the size of a channel accurately.

Table 4.1. Dimensions and channelized erosion rate (Mg ha^{-1}) of a channel derived from the DEMs using both methods during the summer period (bulk density = 1.1 g cm^{-3} in AAFC Fredericton Research and Development Centre).

Method	Area (m^2)	Volume (m^3)	Length (m)	Width (cm)	Depth (cm)	Channelized Erosion Rate (Mg ha^{-1})
TSS	8.90	0.25	17.22	51.7	2.8	5.73
CRP	6.45	0.21	27.85	23.2	3.3	4.81

4.3.2 Elevation change

4.3.2.1 The TSS method

The TSS measurement was not conducted before hurricane event due to time limitations. Therefore, for the TSS method, DEM comparisons were only conducted between the June 20th data (after seeding) and the July 8th data (after the storm event), representing surface evolution during the early summer period with a storm event towards the end of this period. Three examples were shown below.

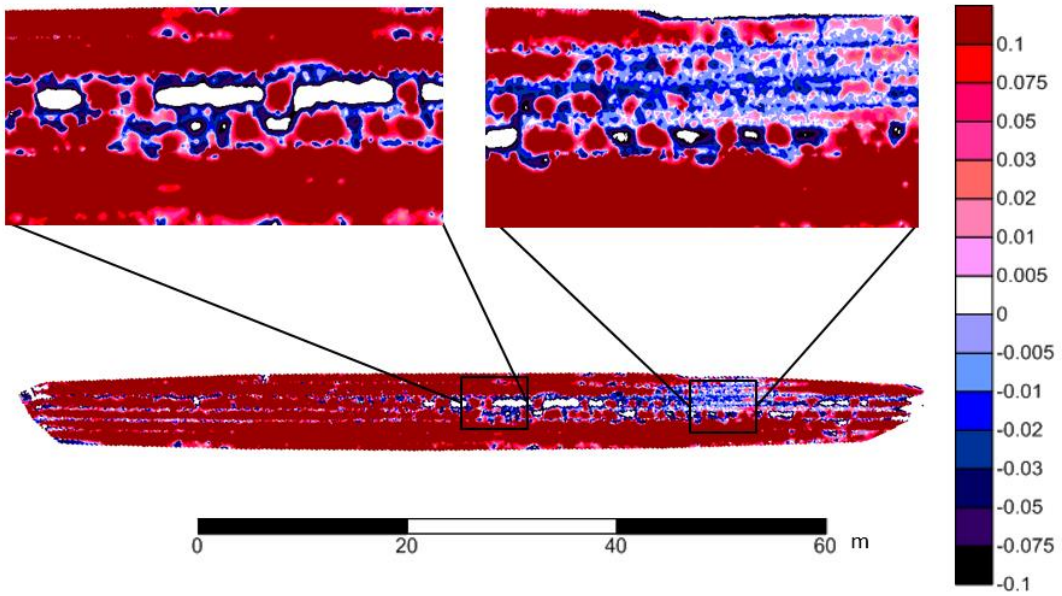

Figure 4.4. Elevation changes (m) of Plot 2 (T1) generated using TSS method for the period from June 20th, 2014 to July 8th, 2014 (red color represents elevation rise; blue color represents elevation drop).

Plot 2 was a contour plot with an approximately 0% – 4% slope along the long edge of the plot. As illustrated in Fig. 4.4, most areas of the plot had increases in elevation by more than 10 cm. Just a few areas without potato canopy coverage showed elevation drop. Such large elevation increases for most areas of the plot was likely a reflection of canopy growth (the view of the total station scanner to the soil surface was blocked by the standing potato canopy), which was not filtered with the TSS method.

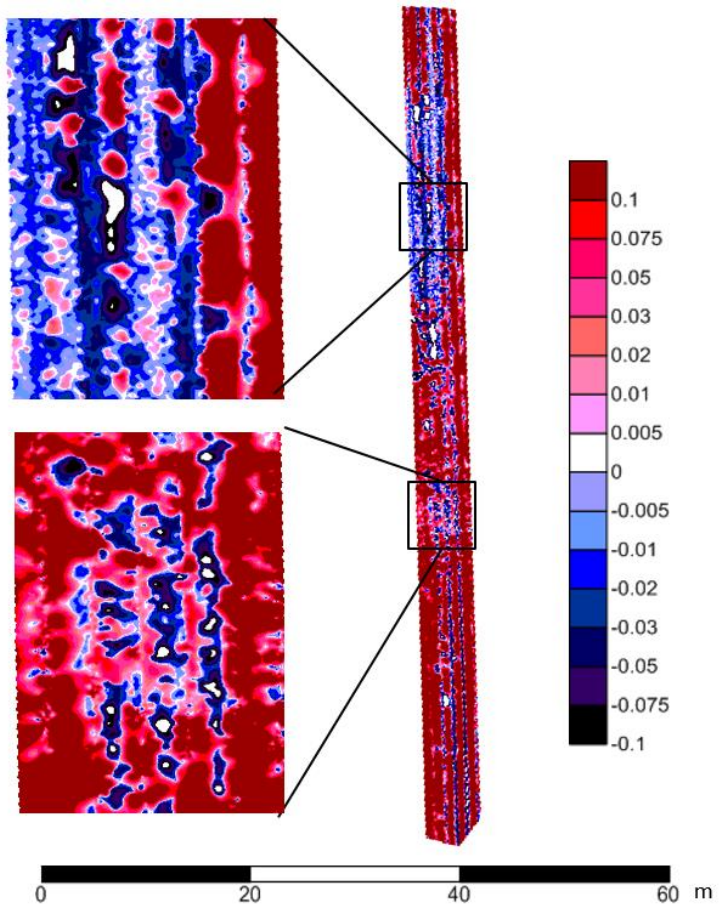

Figure 4.5. Elevation changes (m) of Plot 4 (T2) generated using TSS method for the period from June 20th, 2014 to July 8th, 2014 (red color represents elevation rise; blue color represents elevation drop).

Plot 4 was an up-down-slope plot, with slope gradient, ranged from 8% to 16%. The pattern of elevation change was similar to that of the Plot 2 (Fig. 4.5). Elevation drop was observed on the upper-slope location where no potato grew. However, for most areas of the plot, the elevation raised for more than 10 cm. The Plot 5 was under the up-down-slope fallow tillage treatment (Fig. 4.6). The comparison again showed net elevation rise as a whole, although slight elevation drops were observed sporadically in the range of 0 m – 20 m and 40 m – 60 m from the top of the plot.

During the early summer period and the storm event, rainfall erosion usually had the

strongest impact on soil surface elevation. Under this condition, a net elevation drop was expected. Overall, for the TSS method, the DEMs of the plots under the potato tillage treatments were not able to reflect the soil surface morphology correctly due to the canopy effect.

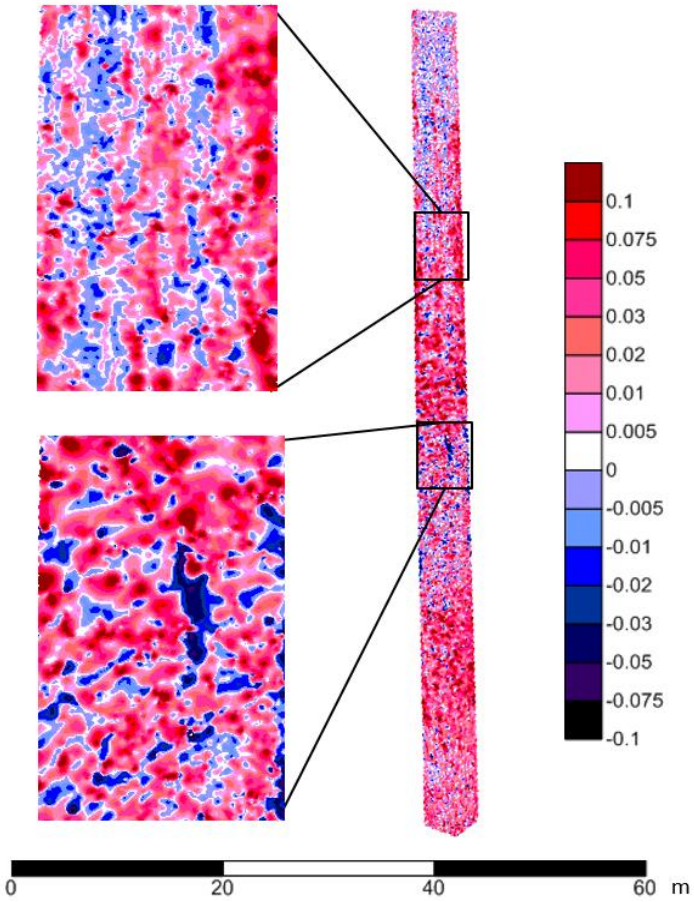

Figure 4.6. Elevation changes (m) of Plot 5 (T0) generated using TSS method for the period from June 20th, 2014 to July 8th, 2014 (red color represents elevation rise; blue color represents elevation drop).

4.3.2.2 The CRP method

The DEM comparisons derived from the CRP method were also only conducted between the June 20th data (after seeding) and the July 8th data (after the storm event), matching the comparisons derived from the TSS method. The results for all plots

were shown in Fig. 4.7; Fig. 4.9; Fig. 4.11; Fig. 4.13; Fig. 15; Fig. 4.17. It should be noted that canopy filtering was conducted for all photos used for generating DEM. As a result, most areas shown as white in color in these maps were blanked area covered by potato canopy.

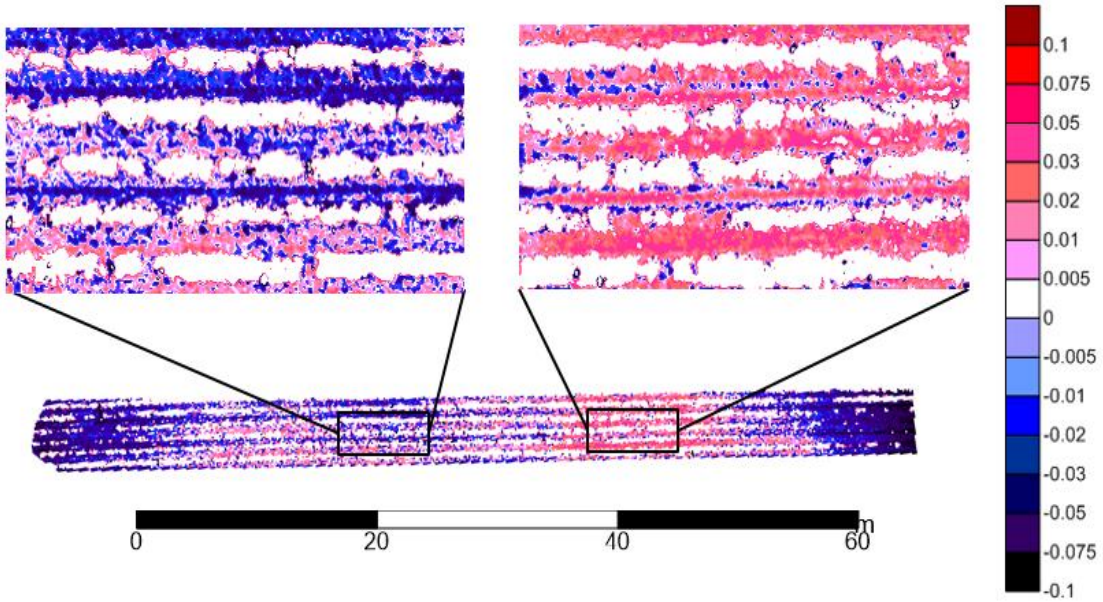

Figure 4.7. Elevation changes (m) of Plot 1 (T1) generated using CRP method for the period from June 20th, 2014 to July 8th, 2014 (red color represents elevation rise; blue color represents elevation drop).

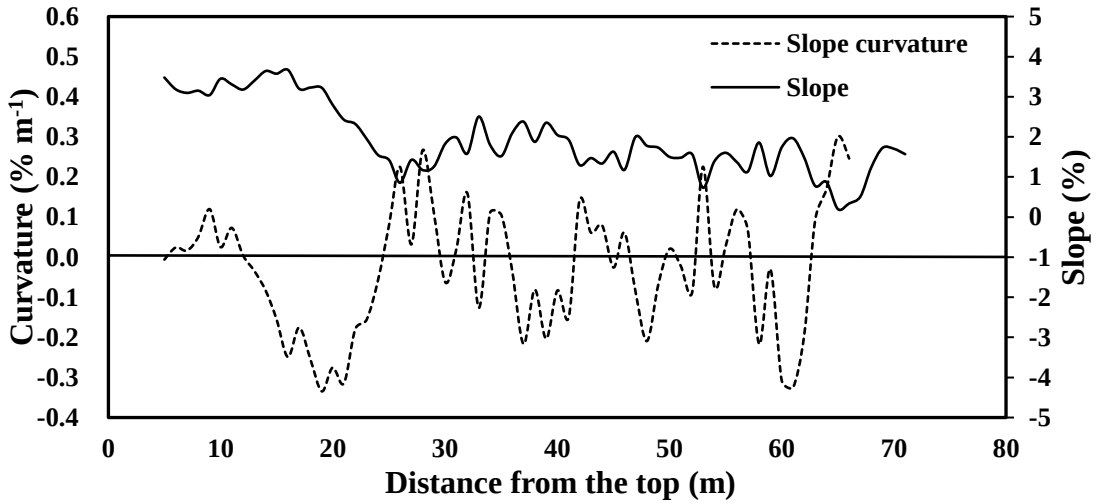

Figure 4.8. Lengthwise slope curvature (% m^{-1}) and slope gradient (%) of Plot 1 (T1) in July 2014.

Plot 1 was oriented along the contour with a slight angle (Fig 4.7). Slope gradient ranged approximately from 0% to 4% and slope curvature ranged from -0.3% m^{-1} to 0.3% m^{-1} (Fig. 4.8). During the detecting period, there was a drop in elevation within ranges of 0 m - 10 m and 25 m – 40 m in the plot, probably because of increasing slope gradient at the same locations. At 10 – 25 m, a convex shape, and a decreasing slope gradient were observed, resulting in an elevation rise. Beyond 40 m, an elevation rise was observed at approximately 50m - 65 m, where slope gradient decreases. Then there was a high elevation drop again at the bottom of the plot.

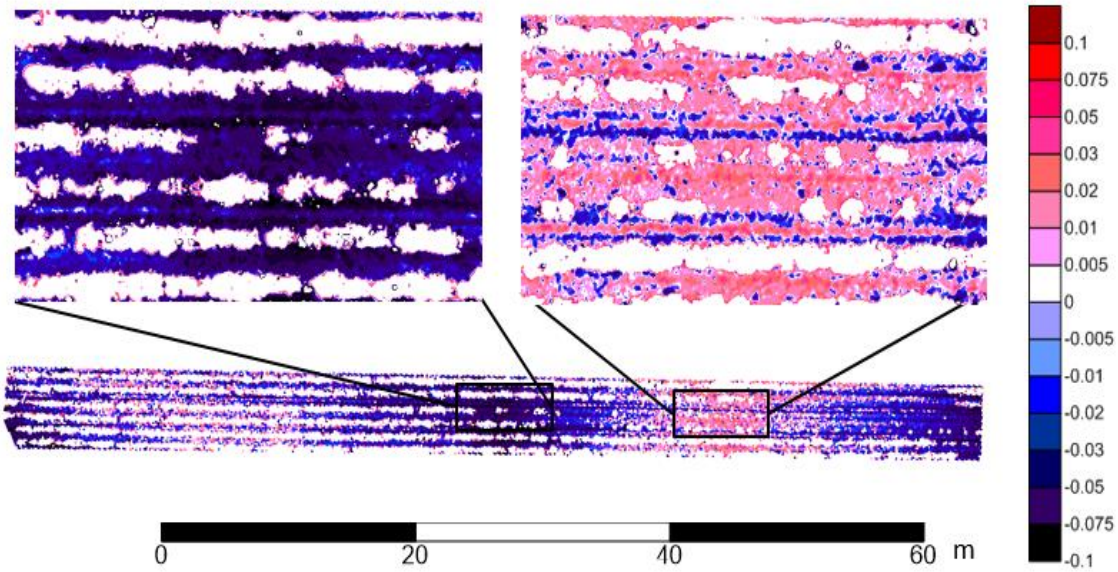

Figure 4.9. Elevation changes (m) of Plot 2 (T1) generated using CRP method for the period from June 20th, 2014 to July 8th, 2014 (red color represents elevation rise; blue color represents elevation drop).

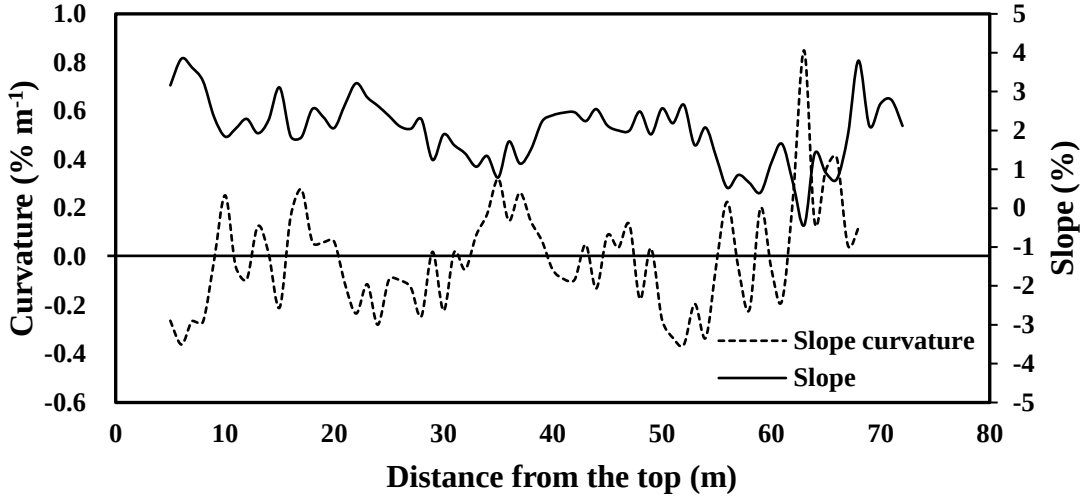

Figure 4.10. Lengthwise slope curvature (% m^{-1}) and slope gradient (%) of Plot 2 (T1) in July 2014.

Plot 2 was also a contour plot. Slope gradient ranged approximately from 0% to 4% and slope curvature ranged from -0.4% m^{-1} to 0.8% m^{-1} (Fig. 4.10). A high elevation drop was observed at about 0 m - 20 m from the right of the plot. There was an elevation rise at about 20 m to 30 m, probably because of a decreasing slope gradient. Then a high elevation drop was observed again at approximately 30 - 50 m, where the slope is convex in shape. At about 50 m – 60 m, elevation raised slightly again at concave locations. In comparison to elevation change extracted from the TSS method, the pattern of elevation change can be observed clearly. Moreover, the average elevation change extracted from the TSS was about 22 cm higher than that extracted from the CRP method, which was approximately the same as the average height of the canopy.

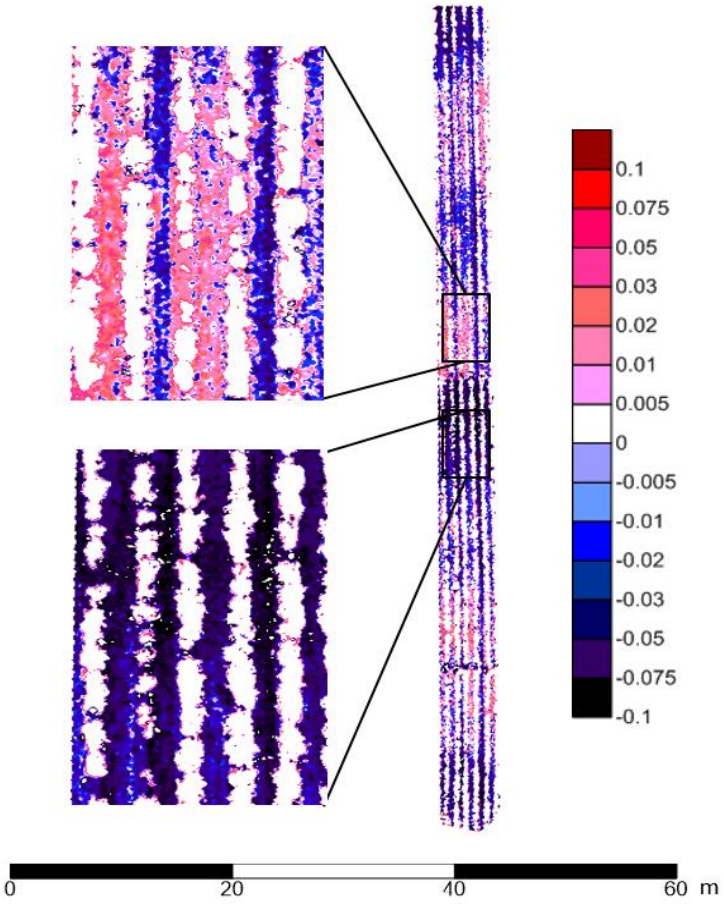

Figure 4.11. Elevation changes (m) of Plot 3 (T2) generated using CRP method for the period from June 20th, 2014 to July 8th, 2014 (red color represents elevation rise; blue color represents elevation drop).

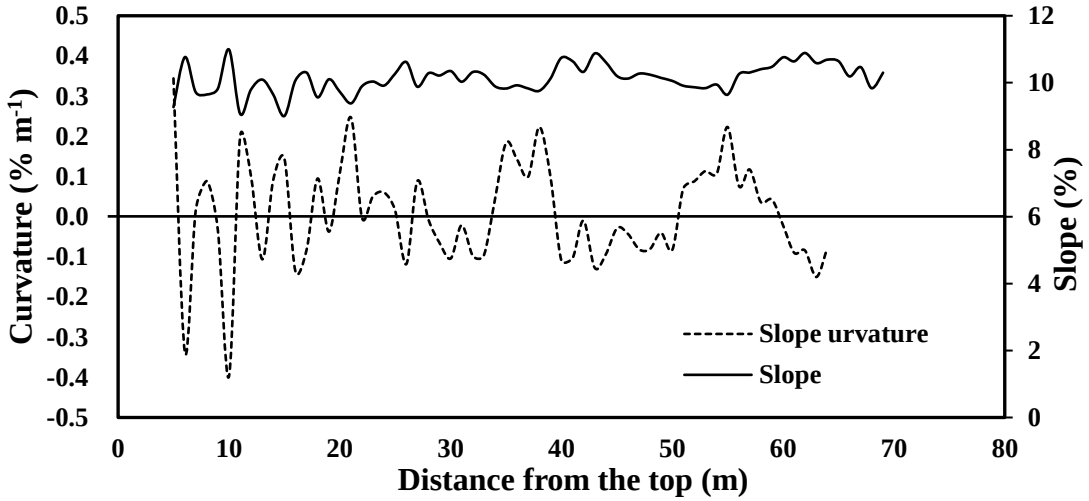

Figure 4.12. Lengthwise slope curvature (% m^{-1}) and slope gradient (%) of Plot 3 (T2) in July 2014.

Plot 3 is oriented from top to bottom (Fig. 4.11). Slope gradient for Plot 3 ranges from 9 to 11% and slope curvature ranged from -0.4% m^{-1} to 0.4% m^{-1} (Fig. 4.12). For the summer period, the comparison showed an overall drop in elevation. In the range of 20 m – 25 m, there was a substantial increase of elevation drop, probably because of a convex shape at the slope. Beyond 25 m, the elevation rise was observed until about 35 m, probably because of a concave shape. A similar pattern of elevation change was repeated for the rest of plot.

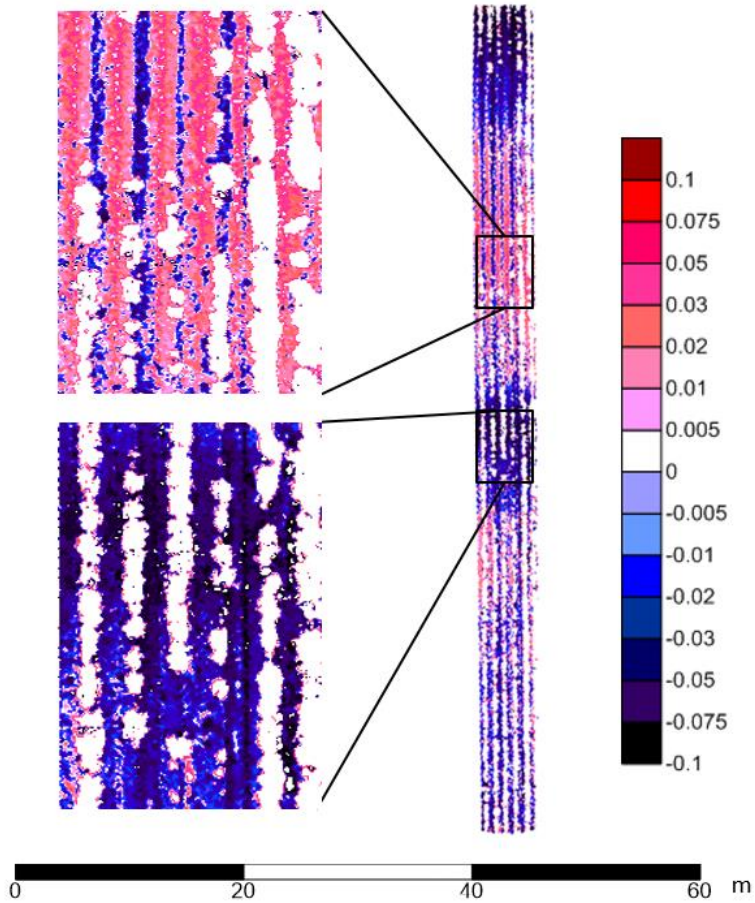

Figure 4.13. Elevation changes (m) of Plot 4 (T2) generated using CRP method for the period from June 20th, 2014 to July 8th, 2014 (red color represents elevation rise; blue color represents elevation drop).

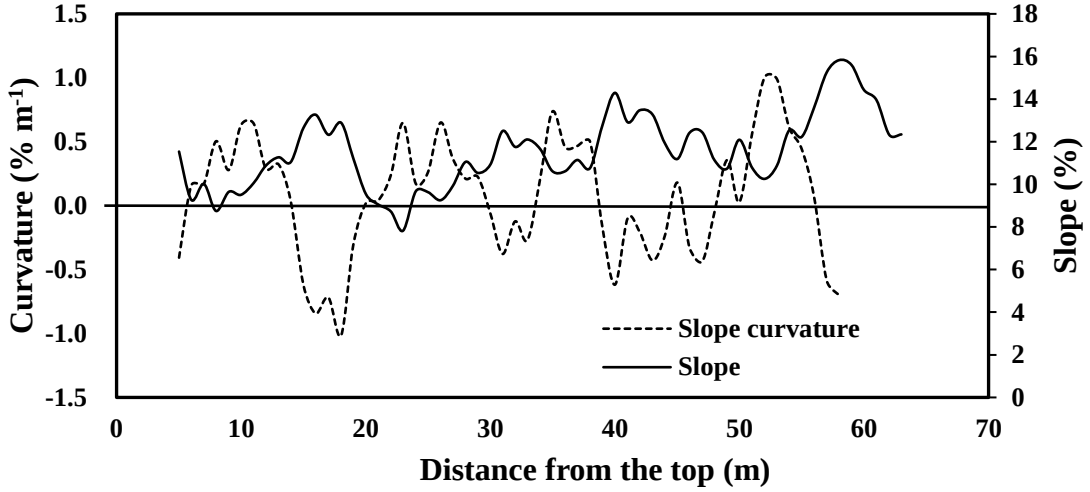

Figure 4.14. Lengthwise slope curvature (% m^{-1}) and slope gradient (%) of Plot 4 (T2) in July 2014.

For Plot 4, the slope gradient ranged from 8% to 16% and slope curvature ranged from -1% m^{-1} to 1% m^{-1} (Fig. 4.14). A higher elevation drop was observed at the top of the plot (Fig. 4.13). Then as slope gradient increased, an elevation rise was observed at about 20 m – 40 m. In addition, the elevation rise was much higher than that of the Plot 3 at this location, probably because of the surface shape of this area. Beyond 40 m, a similar pattern of elevation change as Plot 3 was observed. In addition, the average elevation change extracted from the CRP was about 12 cm lower in comparison to that extracted from the TSS method.

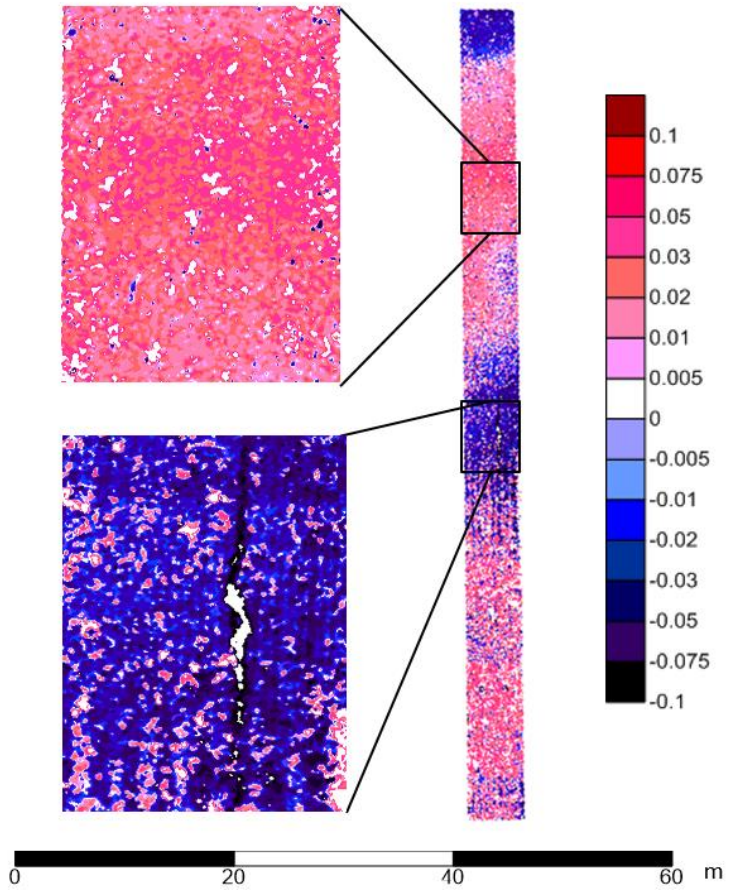

Figure 4.15. Elevation changes (m) of Plot 5 (T0) generated using CRP method for the period from June 20th, 2014 to July 8th, 2014 (red color represents elevation rise; blue color represents elevation drop).

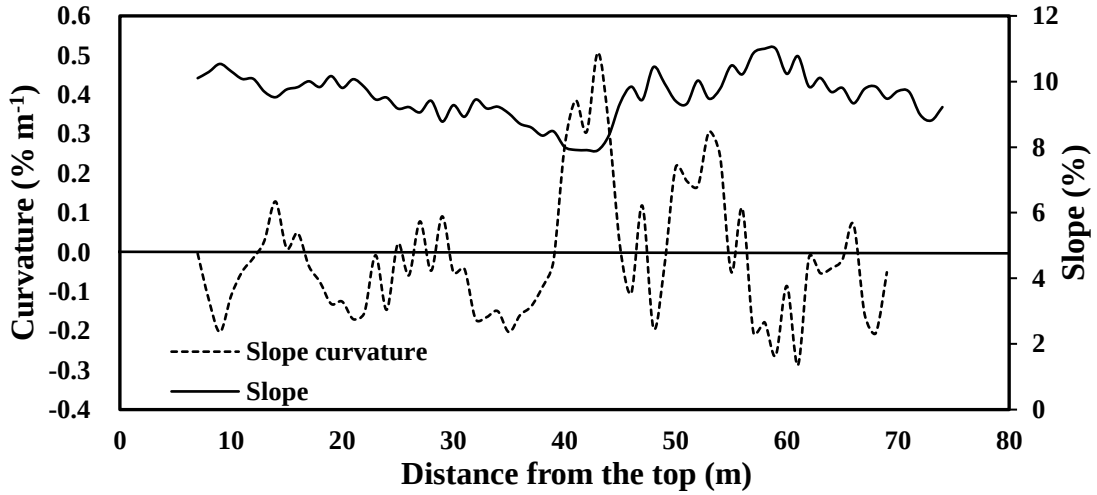

Figure 4.16. Lengthwise slope curvature (% m^{-1}) and slope gradient (%) of Plot 5 (T0) in July 2014.

Plot 5 was a fallow up-down-slope tillage plot. Fig. 4.15 showed a very clear pattern of elevation change. Slope gradient ranged approximately from 8% to 11% and slope curvature ranged from -0.2% m^{-1} to 0.5% m^{-1} (Fig. 4.16). The higher elevation drop was observed at the top of the plot, whereas at about 10 m – 40 m, elevation raised. Beyond 40 m, the pattern of elevation change was repeated again. Unlike the other plots, the pattern of elevation change was similar to the pattern of slope gradient. In comparison to the elevation change extracted from the TSS method, the average elevation change extracted from the CRP method was about 2 cm lower, probably corresponding to the height of the grass. On the other hand, comparisons derived from both methods showed a similar pattern of elevation change, probably because some grass canopies captured by the total station increased the average elevation change.

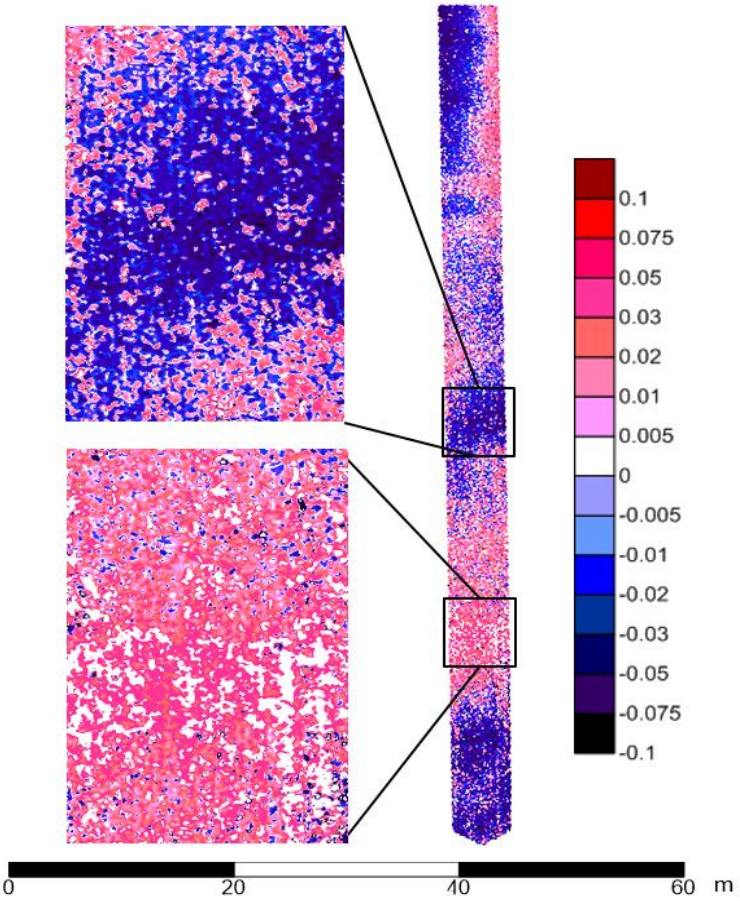

Figure 4.17. Elevation changes (m) of Plot 6 (T0) generated using CRP method for the period from June 20th, 2014 to July 8th, 2014 (red color represents elevation rise; blue color represents elevation drop).

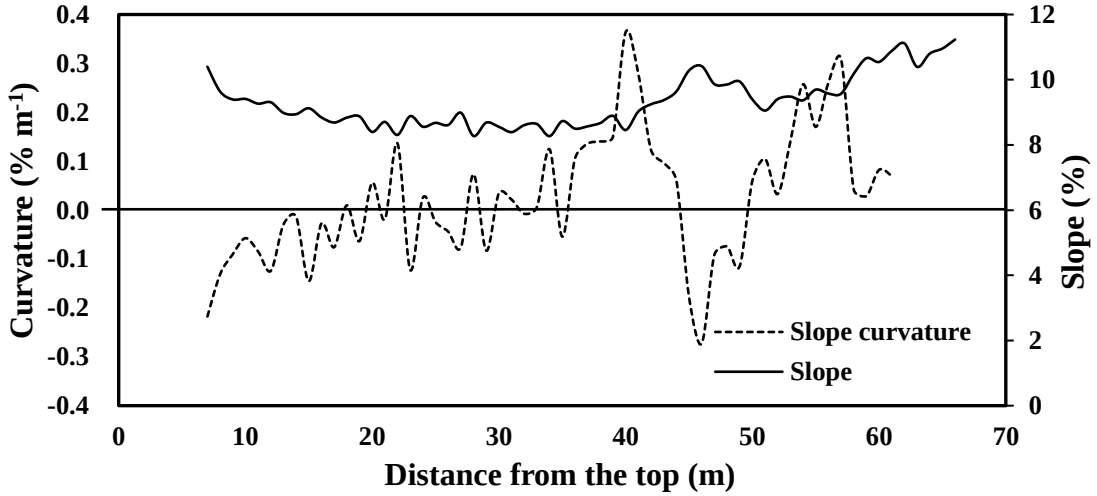

Figure 4.18. Lengthwise slope curvature (% m^{-1}) and slope gradient (%) of Plot 6 (T0) in July 2014.

Plot 6 showed a similar pattern of elevation change as Plot 5 (Fig. 4.17). Slope gradient in the Plot 6 ranged approximately from 8% to 11% and slope curvature ranged from -0.3% m^{-1} to 0.4% m^{-1} (Fig. 4.18). In the range of 10 m – 40 m, unlike Plot 5, the elevation rise was observed on the sides. Then the highest elevation drop was observed at about 40 m, probably because of an obvious convex shape at this location. The highest elevation rise was observed at about 45 m, corresponding to a concave shape at this location. In comparison to the elevation change extracted from the TSS method, a similar pattern of elevation change was observed and the average elevation change extracted from the CRP method was about 12 cm lower, probably corresponding to the height of the grass as well. However, the height of the grass of the Plot 6 was about 10 cm higher than that of the Plot 5, probably because the TSS method of the Plot 6 was conducted a few days later after that of the Plot 5. During these days, the fast- growing grass caused 10 cm difference.

Overall, for the DEMs derived from the TSS method, the surface elevation change cannot be detected accurately due to the canopy cover, whereas for the DEMs derived from the CRP method, the surface elevation change can be detected more accurately with a large shooting angle and photo pre-processing to remove canopy covered area. Most plots showed a similar pattern of elevation change. Higher elevation drop can be observed in the range of 40 m – 50 m whereas elevation rises were found before and after this area. At the bottom of each plot, DEM comparisons showed a consistent trend of elevation drop. Before plant growth, those areas where

potato grew were susceptible to the erosion action due to the convex shape of plowed ridge. At about one-third canopy coverage, the overall canopy effect reduced the erosivity of rainfall, leading to the greatest reduction in erosion. For each potato plot, there was an underestimation of elevation drop. Despite the inaccurate in detecting elevation change, the trend of elevation change still can be observed. In Table 4.2 below, the positive value indicated a net elevation rise whereas the negative value indicated a net elevation drop. There was a clear trend that all the potato plots showed a net elevation drop. On the other hand, there was a net elevation rise for both fallow tilled plots, This was likely due to the fact that grass grew on these plots during the detecting period but they were too small to be picked up and filtered out completely and, therefore, the DEM obtained at the end of this period reflected the grass surface, rather than the base soil surface, shown as an apparent elevation rise.

Table 4.2. Mass-based (Mg ha^{-1}) and depth-based (cm) elevation drop with different tillage treatments using remote sensing methods during the summer period (bulk density = 1.1 g cm^{-3} in AAFC Fredericton Research and Development Centre).

Plot No.	Tillage treatment	Mass-based elevation change (Mg ha^{-1})	Elevation change (cm)
1	T1	-52.46	-0.5
2	T1	-108.12	-1.0
3	T2	-111.60	-1.0
4	T2	-79.80	-0.7
5	T0	89.12	0.8
6	T0	20.54	0.2

With respect to local topography, it appeared that the correlation coefficient between

the elevation change and slope gradient of most plots was significant (Table 4.3). For all plots except for the Plot 3, elevation change was found to correlate significantly with slope gradient, indicating a significant impact of slope gradient on observed elevation change. Whereas for all plots except for the Plot 5, elevation change was not found to correlate significantly with slope curvature, suggesting that the impact of slope curvature was not significant on observed elevation change. In addition, for the most plot showed elevation drop, elevation change had a negative relationship with slope gradient, indicating increasing slope gradient actually reduced elevation change. In contrast, increasing slope gradient amplified elevation change in the plot showed elevation rise.

Table 4.3. Correlation Coefficient (r) between elevation change and slope gradient and between elevation change and slope curvature for 6 plots during the summer period.

Correlation Coefficient (r)	Plot 1	Plot 2	Plot 3	Plot 4	Plot 5	Plot 6
Between Eleavtion change and Slope gradient	-0.36 *	-0.41 *	0.04	-0.36 *	0.68 *	0.48 *
Between Elevation change and Slope curvature	-0.05	0.02	-0.22	-0.03	-0.38 *	0.18

4.3.3 Method verification

After a huge hurricane event, surface elevation experienced a dramatic change. Some changes can be observed visually from comparing the photos taken before and after the hurricane. For example in Fig 4.19, it can be seen that many exposed rocks were buried and tire tracks of the tractor were filled with sediments after the hurricane.

Such subtle changes in surface morphology were reflected in the DEMs obtained from the CRP method as shown in Fig. 4.20.

Figure 4.19. Part of Plot 2 (T1) before the hurricane (left) and part of Plot 2 after the hurricane (right).

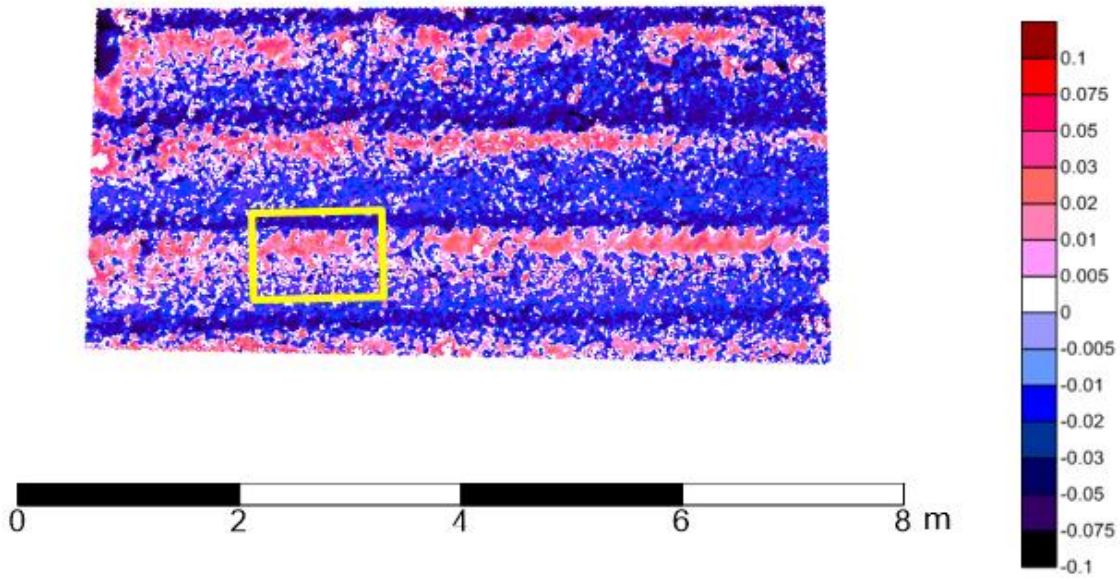

Figure 4.20. Elevation changes (m) of Plot 2 (T1) generated using CRP method before and after the hurricane event (red color represents elevation rise; blue color represents elevation drop).

Another example is shown a portion of Plot 3. In Fig 4.21, the black box indicated the area where soil accumulation happened. The soil particles were transported down the slope after the hurricane, resulting in a sediment deposition in a strip shape along the furrow. This deposition is reflected in the DEM difference as shown in Fig 4. 22.

Figure 4.21. Part of Plot 3 (T2) before the hurricane (left) and part of Plot 3 after the hurricane (right).

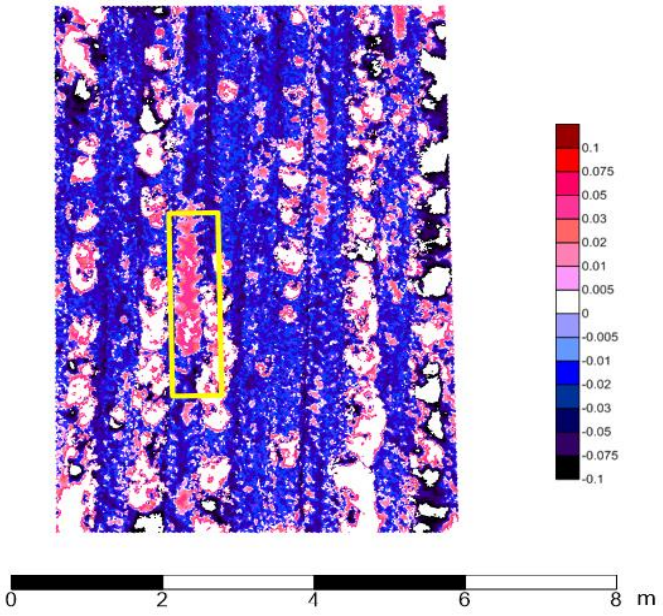

Figure 4.22. Elevation changes (m) of Plot 3 (T2) generated using CRP method before and after the hurricane event (red color represents elevation rise; blue color represents elevation drop).

For the two examples above, the elevation changes observed in the photos were shown in the each DEM, indicating that the elevation change derived from the CRP method can reflect reality correctly.

4.4 Conclusion

In this study, the TSS method was not able to correctly capture changes in soil surface morphology due to changing vegetation cover along about one-third of the field. This cover blocked scanning at the low shooting angle (~20º) by creating a shadow effect. The cameras used in the CRP had a much larger shooting angle (~70º), but the vegetation cover still blocked a significant portion of the view. Hence, further image processing was necessary to generate a DEM for the bare-earth surface. This processing, i.e., deleting green image pixels, however, could still not fully achieve the desired accuracy for bare-ground elevation estimation. For the TSS method, all elevation points including vegetation cover were recorded as raw 3D data points, causing errors across the surface. In comparison, the summer surface derived from the CRP method was more accurate than the TSS method during this period.

With respect to the channel formation, the only large channel generated across the field occurred on the T0 treatment on Plot 5, probably because the soil surface of within this plot was not protected by potato canopy, and had a convex shape. Otherwise, all plots showed a similar pattern. There was a drop in elevation at approximately 0 – 20 m and 40 – 50 m from the top of the plot. A surface rise was observed in the distance range of approximately 20 – 40 m and 50 – 70 m. The plots under potato tillage and fallow tillage showed two opposing trends: (i) for the T1 and T2 treatments, net elevation drops were observed; (ii) for the plots under T0 treatments, net elevation rises were observed. However, these differences were likely

due to the artifacts created by grass growing on T0 plots. In general, the observed elevation changes during summer were combined results of rainfall erosion, gravitational subsidence after tillage and dry-wet action. While the CRP method can detect elevation changes during summer, it cannot be used to distinguish among the processes that impact soil surface elevations.

Reference

Berger, C., Schulze, M., Rieke-Zapp, D., Schlunegger, F., 2010. Rill development and soil erosion: a laboratory study of slope and rainfall intensity. Earth Surface Processes and Landforms. 35(12): 1456-1467.

Bewket, W., Sterk, G., 2003. Assessment of soil erosion in cultivated fields using a survey methodology for rills in the Chemoga watershed, Ethiopia.Agriculture, ecosystems & environment. 97(1): 81-93.

Couper, P., Stott, T., Maddock, A., 2002. Insights into river bank erosion processes derived from analysis of negative erosion-pin recordings: Observations from three recent UK studies. Earth Surf. Process. Landf. 27: 59–79.

Gessesse, G.D., Fuchs, H., Mansberger, R., Klik, A., Rieke-Zapp, D.H., 2010. Assessment of erosion, deposition and rill development on irregular soil surfaces using close range digital photogrammetry. The Photogrammetric Record. 25(131): 299-318.

Govers, G., 1991. Rill erosion on arable land in central Belgium: rates, controls and predictability. Catena. 18(2): 133-155.

Hancock, G.R., Crawter, D., Fityus, S.G., Chandler, J., Wells, T., 2008. The measurement and modelling of rill erosion at angle of repose slopes in mine spoil. Earth Surface Processes and Landforms. 33(7): 1006-1020.

Herweg, K., 1996. Field manual for assessment of current erosion damage. SCRP, Ethiopia and Centre for Environment and Development, University of Berne, Switzerland.

Laflen, J.M., Flanagan, D.C., Ascough, J.C., Weltz, M. A.and Stone, J. J., 1994. The WEPP model and its applicability for predicting erosion on rangelands. Variability in Rangeland Water Erosion Process variabilityinra, 11-22 p.

Lawler, D.M., Couperthwaite, J., Bull, L., Harris, N.M., 1997. Bank erosion events and processes in the Upper Severn Basin. Hydrol. Earth Surf. Sci. 1: 523–534.

Meyer, L.D., Foster, G. R. and Romkens, M. J. M., 1975. Source of soil eroded by water from upland slopes. Present and prospective technology for predicting sediment yields and sources. 177: 189.

Nasermoaddeli, M.H., Pasche, E., 2008. Application of terrestrial 3D laser scanner in quantification of the riverbank erosion and deposition. Proceedings of Riverflow. 3-5 p.

Poesen, J., Nachtergaele, J., Verstraeten, G., Valentin, C., 2003. Gully erosion and environmental change: importance and research needs, Cantena. 50: 91–133.

Schowengerdt, R. A., 2007. Remote Sensing: models and methods for image processing (3rd ed.). Academic Press. 2 p.

Schmid, T., Schack-Kirchner, H., Hildebrand, E., 2004. A case study of terrestrial laser scanning in erosion research: calculation of roughness and volume balance at a logged forest site. In Proceedings of the ISPRS Working Group VIII/2:

Laser-Scanners for Forest and Landscape Assessment. 3-6 p.

Stott, T. A., 1997. Comparison of stream bank erosion processes on forested and moorland streams in the Balquhidder catchments, Central Scotland. Earth Surf. Process. Landf. 22: 383–399.

Vinci, A., Brigante, R., Todisco, F., Mannocchi, F., Radicioni, F., 2015. Measuring rill erosion by laser scanning. Catena. 124: 97-108.

Chapter 5

Conclusion

5.1 General conclusions

This thesis presents the results achieved for two remote sensing methods (TSS and CRP) for assessing erosion-caused differences in bare-earth soil elevations and using ridged and channeled surfaces for determining the measurement error. It was found that the CRP method using a large shooting angle (90º and 70º) produced better results than the TSS method in detecting channels and elevation change. For the CRP method, the performances were further improved using higher overlap rates. In practice, the TSS method can be conducted by one operator to cover a relatively large area at one setting (e.g., 100 m by 100 m). With the handheld CRP method, the operator is limited to capture surface morphology changes within narrow strips only (e.g., no more than 3m wide). For wider areas, a special platform needs to be used.

For the field experiments, during the summer period, most comparisons of the plots showed a drop in elevation in the distance ranges of approximately 0 – 20 m and 40 – 50 m from the top of the plot. On the other hand, the surface rise was observed at approximately 20 – 40 m and 50 – 70 m. This pattern of elevation change was related to the local topography significantly in most cases. Meanwhile, one water-induced rill was detected under the fallow up-down-slope tillage. The elevation changes between different treatments were different. The plots under the potato tillage showed a net elevation drop whereas the plots under fallow tillage showed a net elevation rise. This discrepancy was likely a result of the grass growth on the fallow tillage plots. Moreover, observed elevation change was not able to distinguish the

effects of soil erosion from other contributing processes such as dry/wet cycling and gravitational subsidence after tillage. For the winter period, rills were detected in the plot under the fallow up-down-slope tillage as well. Unlike in the summer period, there was a drop in elevation for the plot as a whole during the winter period. There was no obvious difference of surface morphological change between treatments, indicating that the effect of crop type and slope orientation was not strong. In addition, the pattern of elevation change was associated with the change of soil moisture and soil temperature better than snowmelt and rainfall runoff amount, indicating the significant contribution the freeze-thaw action may have towards elevation change. For both periods, the comparisons also indicated that the CRP method was better than the TSS method on capturing the surface morphological change.

Overall, both remote sensing methods still cannot overcome the challenge that there are multiple processes happening simultaneously, all affecting soil surface morphology. For the summer period, part of the plot was blocked by the plant canopy coverage, resulting in an inaccurate detection of soil surface for the entire plot. For the winter period, snowmelt erosion just contributed about 1% - 3% to the elevation change. Therefore, these two remote sensing methods were not able to distinguish an accurate erosion volume from elevation change. In addition, both methods were capable of quantifying soil lost from water-induced rill and detecting pattern of elevation changes correctly.

5.2 Suggested future work

Very little difference was observed between treatments in this study. This is probably due to the low magnitude of soil erosion occurred in the experimental periods. Further studies on examine the effect of these different treatments are suggested to be carried out in long-term plots or under controlled conditions. For the summer period, the challenge for soil surface detection is canopy cover due to crop and grass growth. Caution should be taken on the timing of measurement to avoid canopy effect as much as possible. Also, new technology needs to be developed to remove small sized canopy more efficiently. Unlike the summer period, bare ground is detected for the winter period. Remote sensing method can detect channel created by snowmelt erosion accurately. However, for overall elevation change, the result indicated that snowmelt erosion is not the dominant process. Future study should not rely on surface elevation change detection for snowmelt erosion rate assessment other than those in the form of rill or ephemeral gully.

With respect to the methods, although the detection range of the handheld CRP methods was limited, the error assessment indicated that the handheld camera photogrammetry with large shooting angles can provide the best accuracy among all methods. It is a handy way to conduct photogrammetry, requiring a camera and some reference targets. Therefore, it is possible to employ this method to detect rill and ephemeral gully in the nature environment where is hard to assess with large equipment.

APPENDIX I

Camera calibration process

1. Focusing the camera lens to the required camera to object distance

    1.1. Switch camera to auto-focus

    1.2. Positioning the camera to the camera to object distance required for the application in front of test field

    1.3. Slowly press the shutter release button that the camera focuses the lens automatically

    1.4. Switch camera to manual focus

    1.5. Fix the lens using electrical tape

2. Make sure camera is set to the following operation modes

    2.1. Use aperture priority setting (capital letter A left switch)

    2.2. Manual focus

    2.3. Use self-timer

3. Settings in the camera menu:

    3.1. Jpeg image quality has to be set to “fine”

    3.2. Jpeg compression “high quality”

    3.3. Auto distortion correction “off”

    3.4. Automatic image rotation “off”

4. Taking images for calibration:

    4.1. Setup camera at the camera to object distance required for the application slightly to the left of test field with a mildly oblique camera position

    4.2. Make sure that the entire image format is covered with targets for every image captured apart from rotated images

    4.3. Move camera to the right (approximately 1-1.5m) at the same distance to the test field and take an image

    4.4. Rotate the camera by 90 degrees and acquire an image. Move camera to the center of test field and take an image (not rotated)

    4.5. Rotate camera by 90 degrees and take an image

4.6. Move camera to the right and take an image (not rotated)

4.7. Rotate camera by 90 degrees and take image

4.8. Move camera slightly to the right of the test field to approximately the same position of note 4.1

4.9. Take an image not rotated

4.10. Move camera closer to test field (approximately 0.5m)

4.11. Take images right, center and left

4.12. Move camera 0.5 m back from the original distance and acquire images left, center and right

APPENDIX II

Elevation changes (m) derived from the TSS method during the winter and snow melting period (from Nov 2013 to May 2014) were listed as follow.

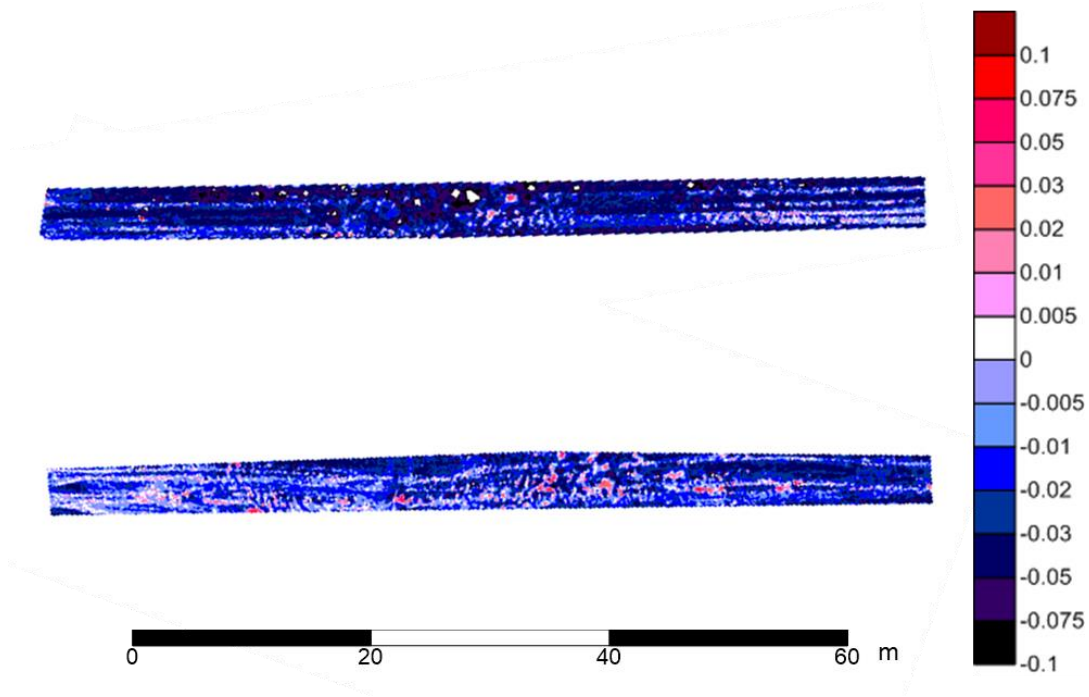

Elevation changes (m) of Plot 1 (top) and Plot 2 (bottom) under potato contour tillage (T1) using TSS method (red color represents elevation rise; blue color represents elevation drop).

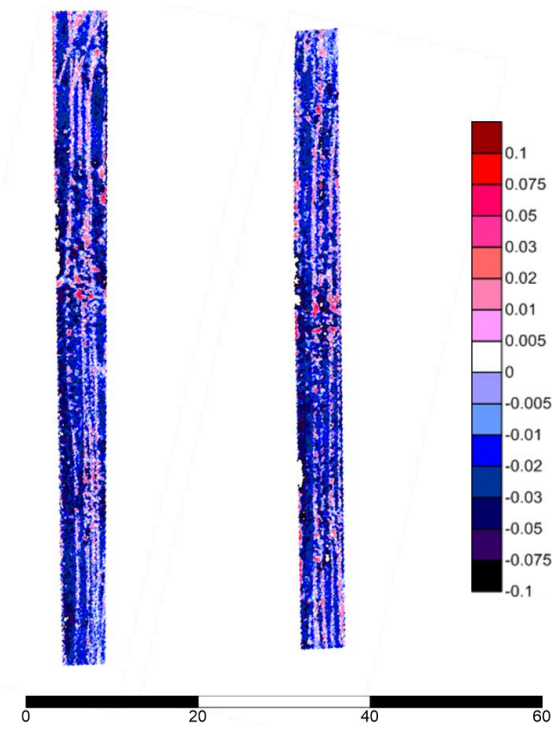

Elevation changes (m) of Plot 3 (left) and Plot 4 (right) under potato up-down-slope tillage (T2) using TSS method (red color represents elevation rise; blue color represents elevation drop).

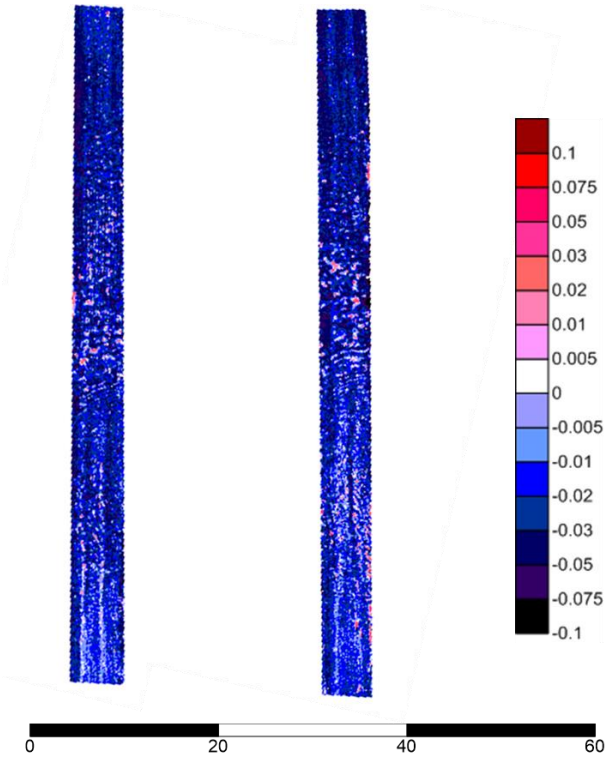

Elevation changes (m) of Plot 5 (left) and Plot 6 (right) under fallow up-down-slope tillage (T0) using TSS method (red color represents elevation rise; blue color represents elevation drop).

Curriculum Vitae

Candidate's full name: Fangzhou Zheng

Universities attended:

University of New Brunswick, Canada, M.Sc. Forestry Candidate, 2012-2016

Dalhousie University Faculty of Agriculture, Canada, B.Sc. (Hons.) Agriculture, 2012

Fujian Agriculture and Forestry University, China, B.Sc. Agriculture, 2010

Conference Oral and Poster Presentations:

Zheng, F.Z., Li, S., Meng, F. R., Wackrow, R., Lobb, D., 2015. Quantifying different water erosion processes by detecting soil surface evolution on a cultivated field. *In:* 20th International Soil tillage Research Organization Conference, September 14-18th, 2015.

Zheng, F.Z., Li, S., Robertson, B., Boudreault, M., Geng. X. Y., 2015. Snow distribution in rolling landscape under agriculture and forestry land uses in Atlantic Canada. *In:* 20th International Soil tillage Research Organization Conference, September 14-18th, 2015.